University of Stavanger

Faculty of Science and Technology

Master Thesis

Study program/ Specialization: Petroleum Engineering /Drilling Technology	Spring semester, 2015 Open
Writer: Irene Buan	………………………………… (Writer's signature)
Faculty supervisor: Mesfin Belayneh and Bernt S. Aadnøy	
Title of thesis: Well collapse modeling & Norne & Heidrun well instability sensitivity studies	
Credits (ECTS): 30	
Key words: Wellbore instability Shale Collapse Simulation Mohr-Coulomb Stassi d'Alia	Pages :90 + appendix Stavanger, 15.06.2015

I

Acknowledgements

Abstract

Well collapse is a typical wellbore instability problem in brittle shale and unconsolidated formations. In this thesis, the thermal, chemical, mechanical, hydraulic, elastic and transient effects on the well collapse strength are studied. Single and combined parametric sensitivity studies of collapse pressure were carried out on two well programs, namely Norne and Heidrun.

The result of the sensitivity study indicates that:

- The most sensitive parameters were found to be the Biot's coefficient, Poisson's ratio and the water activity of the drilling fluid for steady state simulation and the uniaxial compressive strength for transient state simulation.
- Parameters such as the coefficient of linear thermal conductivity, E-modulus, and the internal friction angle were found to be less responsive to collapse pressure.
- The combined effect of chemical and transient state demonstrates positive and negative synergy depending on the osmotic outflow.

Table of Contents

List of Figures

List of Tables

List of Symbols

$P = Pressure\ [MPa]$

$F = Force\ [N]$

$A = Area\ [m^2]$

$\varepsilon = Strain$

$L = Length\ [m]$

$\rho = Density\ [g/cm^3]$

$V_P = P-wave\ velocity\ [ft/s]$

$\beta_{GR}, \alpha_{GR} = constants\ depending\ on\ litohology\ (Gardner's\ relation)$

$\sigma = Stress[MPa]$

$\sigma_v = Overburden/vertical\ stress[MPa]$

$\sigma_h = Horizontal\ stress[MPa]$

$\sigma_{Hmax} = Maximal\ horizontal\ stress[MPa]$

$\sigma_{hmax} = Minimum\ horizontla\ stress[MPa]$

$\sigma_{x,y,z} = Stress\ components[MPa]$

$\sigma_{rr} = Radial\ stress\ [MPa]$

$\sigma_{\theta\theta} = Tangetial\ stress\ [MPa]$

$\sigma_{zz} = Axial\ stress\ [MPa]$

$\sigma_{1,2,3} = Principal\ stress[MPa]$

$\sigma_T = Tensile\ stress\ [MPa]\ (Rankine)$

$\sigma_{cl} = Collapse\ failure\ stress\ [MPa]$

$\sigma_{ect} = Tectonic\ stress\ [MPa]$

$\sigma_{bd} = Non\ breakdown\ failure\ index[MPa]$

$\sigma_{min}^{ef} = Minimum\ compressive\ effective\ principal\ stress$

$\sigma_\theta^{Hyd} = Hydraulic\ effect\ [MPa]$

$E = Young's\ Modulus\ [MPa]$

$\nu = Poisson's\ ratio$

$C_0 = Uniaxial\ Compressive\ Strenght\ [MPa]$

$S_0 = Cohesion\ strenght\ [MPa]$

$\beta_{UCS} = Orientation\ of\ the\ failure\ plane\ [deg]$

$\tau = Shear\ stress[MPa]$

$z = Depth\ [m]$

$g = Acceleration\ due\ to\ gravity\ [9,81\ m/s^2]$

$\alpha_{Biot} = Biot's\ coefficient$

$r = Radius\ [m]$

$a = Radius\ of\ wellbore\ [m]$

$\theta = Transformation\ angle\ [deg]$

$c_0 = Thernal\ duffusivity\ of\ a\ porous\ medium\ [mm^2/s]$

$c'_0\ and\ c' = Coupling\ coefficient$

$k = Permeability\ [mD]$

$C_P = Specitic\ heat\ capacity\ [J/K]$

$k_0 = Thermal\ conductivity\ [W/(m*K)]$

$I_m = Membrane\ efficiency$

$V = Volume[m^2]$

$a_{df} = Activity\ of\ drilling\ fluid$

$a_{fw} = Activity\ of\ formation\ water$

$P_\pi = Chemical\ potential[MPa]$

$T = Temperature[K]$

$T_W = Well\ wall\ temperature\ [K]$

$T_0 = Formation\ temperature\ [K]$

$erfc = Complementary\ error\ function$

$t = Time\ [seconds, hours\ or\ days]$

$a_m = Volumetric\ linear\ thermal\ expansion\ coefficient\ of\ rock\ matrix\ [K^{-1}]$

$Rg = Gas\ coefficient = 8.314\ [J/(mol * K)]$

$\varphi = Angle\ of\ internal\ fricition\ [deg]$

$\beta_{MC} = Fractiure\ angle\ of\ the\ rock\ speciemen\ [deg]\ (Mohr - Coulomb)$

α_{Dp}, β_{DP}

$= Constants\ associated\ with\ the\ internal\ friction\ angle\ and\ the\ cohesive\ strength\ (Drucker\ Prager)$

$\sqrt{J^2} = Second\ deviatory\ invariant$

$I_1 = Mean\ effective\ stress\ [deg]$

$k_{MC}, \eta_{MC} = Material\ constant\ (Mohr - Coulomb)$

$k_S, \eta_S, \alpha_S, \beta_S, \omega_S = Material\ constant\ (Stassi\ d'Alia)$

$m_{Ewy}, \eta_{Ewy}, s_{Lade} = Material\ constants\ (Ewy)$

$k_{MgC}, m_{MgC} = Material\ constants\ (Mogi - Coulomb)$

$\Delta ts = Transit\ travel\ time\ [\mu s/ft]$

Abbreviations

NCS: Norwegian Continental Shelf

NPT: Non- Productive Time

SEM: Scanning Electron Microscope

TLP: Tension Leg Platform

UCS: Uniaxial Compressive Strength

1. Introduction

In this thesis, geomechanical modeling and sensitivity analysis are presented. Based on Stassi d'Alia and Mohr-Coulomb failure criteria, two well collapse models were derived. Furthermore, driving forces such as chemical and thermal effects were simulated. The models were tested on Norne and Heidrun well programs. Both the steady state and the transient state of the models were analyzed.

1.1 Background

The fact that well instability is a major cost factor for the oil and gas industry, is familiar to most drilling engineers. Bernt S. Aadnøy (Aadnøy, 2003) estimated that the overall drilling costs increase by 10% due to wellbore instability issues. Two well-known wellbore failures are namely well collapse and well fracture. These are generally caused by shear failure and tensile mechanisms, respectively. As shales are common rocks in drilled formations (about 75%), up to 90% of the wellbore instability problems occur in these rocks (Steiger & Leung, 1992). Despite all of the previous theoretical and experimental studies performed regarding wellbore instability, the problem is still critical and a cost factor for the industry.

The rock-fluid physical-chemical interaction is a complex process. Many efforts have been carried out to construct a model that considers all of the effects and provides information to design the most proper mud weight program for a well. However, there is still no perfect model. While drilling, the pore pressure continuously changes from its original magnitude, as result of temperature, chemical interactions between the mud and the formation and transient effects. As the new pore pressures establish, the stress concentrations around the wellbore changes accordingly. Hence, all of the aforementioned effects have an impact on the on the original well pressures, strengths and Young's modulus. A proper model is therefore essential for predicting these effects.

In this thesis, two failure criteria are reviewed and two models based on these criteria are then derived in order to analyze the chemical, thermal and transient effects. Shale exhibits anisotropic property such that elastic and mechanical properties measurement is directional dependent. However, in this study, a non-laminated based failure criterion was used to study the well collapse behavior in shale formations. The shale geomechanical properties, stresses around wellbore, driving forces, and various shear failure criteria are. In addition, transient and

steady state well collapse modeling and simulation studies in a given well program is presented. Parametric sensitivity studies are evaluated in order to investigate the main dominant driving forces and parameters. Finally, the results obtained from different shear failure models will be compared.

1.2 Problem Definition

As reviewed in the above section, wellbore instability is a critical problem and cost factor for the industry. In the literature, several models are available. The models are a function of diverse driving forces. As pressures, stresses and parameters relevant for wellbore designing changes over time, well failure may occur not just while drilling, but also days after. This is mainly caused by the changes in the physical properties of the shale which swells in contact with water, and also due to the pore pressure change when drilling in low permeable formations and not being able to dissipate when in contact with the mud (Zhang, et al., 2006). This means that, time delay and transient effects must also be considered while drilling to avoid well failure. The intention of a well program is to show the ideal drilling operation in order to drill safely, economic, fast and without instability problems. Therefore, the drilling fluid, well pressures and strengths must be designed within the safe operational window. In addition thermal, chemical and transient effects must be considered while designing these limits.

This thesis addresses issues such as:

- How does the chemical, thermal, the transient effect and the magnitude of these effects in terms of percentage, change in collapse strengths?
- How does single and combined parameters affect the whole picture of well collapse curve?
- Which parameters are the most sensitive and which parameters are insignificant to the associated collapse models?

The analysis of these addressed issues will provide information for designing drilling fluid with respect to density and chemical composition. As a result, one can learn the dynamics of the pore pressure, in-situ stress, uniaxial compressive strength and finally the transient feature of the well program.

1.3 Objectives

The primary objectives of this thesis are:

- To review the mechanical, elastic and mineralogy of shale formation
- To review stress around the wellbore and failure criterion for non-laminated isotropic formation
- To derive well collapse models based on Stassi d'Alia and Mohr-Coulomb failure criteria coupling thermal, chemical and transient effect on the collapse pressure
- Using the derived models, to perform field case studies on Heidrun and Norne well programs:
    - To perform a single parametric sensitivity studies
    - To perform combined parametric sensitivity studies

2 Literature Study

2.1   Typical Geological Formation in NCS

Sedimentary rocks are formed by surface processes through the rock cycle. These processes are weathering (both physical and chemical), erosion, transportation, deposition (also called sedimentation), burial and diagenesis. Most sediments are created by weathering of the continental shelf, while others are the remains of mineral shells secreted by organisms. Oil, natural gas and coal, our most valuable fossil-fuel resources, are found in these rocks.

The most common sedimentary rocks in a petroleum system are carbonates, sandstone and shale. Carbonates and sandstones are typically reservoir rocks, while shale is often referred to as a cap or seal rock. However, depending on the properties, sandstones and carbonates may function as seals and shales also may contain oil or gas. Figure 2.1 illustrates a typical petroleum system explaining the several elements present.
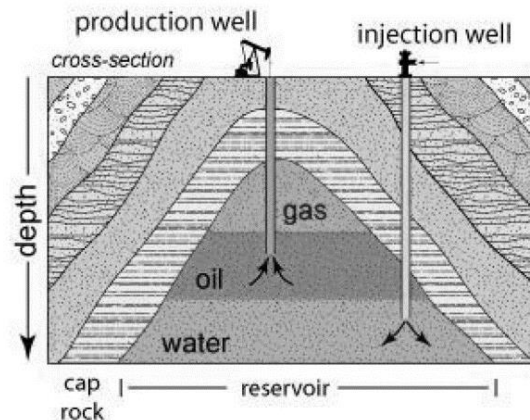
FIGURE 2.1: THE PRINCIPLES OF A PETROLEUM SYSTEM (MYERS, 2015)

Shales are fine-grained clastic sedimentary rocks that mainly consist of hardened clay, silt or mud. The clay content in shale is approximately 40 % or even higher (Shaw & Weaver, 1965). These rocks form distinctive layers, which are easily split. They might be porous, but rarely permeable, which makes them proper seal rocks. Sandstones are also clastic sedimentary rocks, but unlike shales they are composed of sand grains and they are often porous and permeable making them ideal reservoir rocks. Carbonates are sedimentary rocks made of carbonate minerals such as calcite and dolomite. These rocks are also potential good reservoir rocks, when

4

the porosity and permeability are adequate. Limestone and marble are well known carbonates. The first oil field in Norway, Ekofisk, was a permeable chalk reservoir. Chalk is a type of limestone. Figure 2.2 shows the three mentioned sedimentary rocks.

FIGURE 2.2: FROM LEFT SHALE, SANDSTONE AND LIMESTONE (KING, 2015)

The Norwegian Continental Shelf (herby referred to as NCS) is where all of Norway's oil reserves are located. The NCS is commonly divided in three provinces, the Norwegian Sea (Heidrun and Ormen Lange), the North Sea (Ekofisk) and the Barents Sea (Snøhvit and Goliat). Figure 2.3 illustrates the NCS with the three provinces. On average, fields on the Norwegian shelf have a recovery factor of 46% for oil. (Bjørlykke, 2010). While the majority of the producing oil fields are located in the North Sea, the attention of the operators is increasingly directed towards the Barents Sea developments.
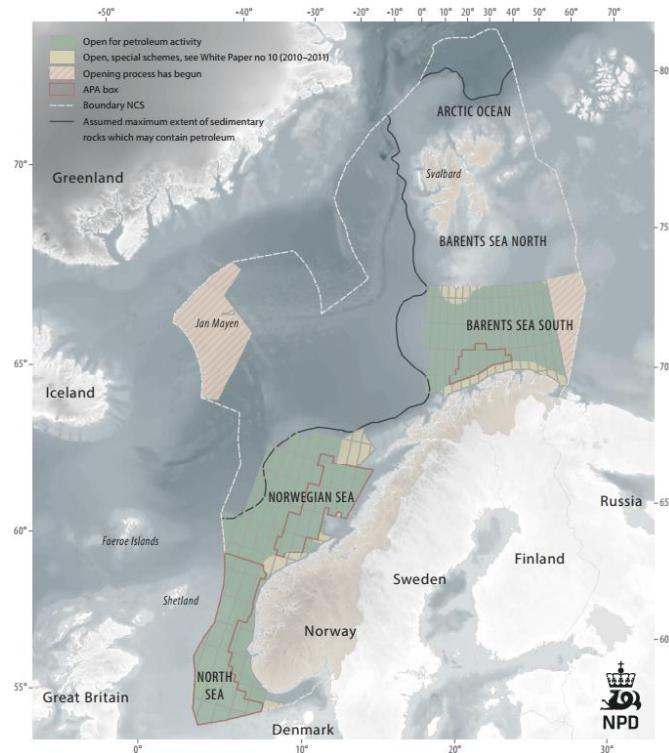
FIGURE 2.3: MAP OVER THE NORWEGIAN CONTINENTAL SHELF (NPD FACTS, 2013)

2.1.1 Challenges of Drilling in a Shale Formation

Wellbore instability is a major concern during drilling operations. It is the result of several factors. Among these are solid-fluid interaction, challenging and complex stress conditions, wellbore deviation, irregular reservoir behavior, inconsistency, lack of appropriate drilling practices, deep water, high pressure and high temperature (HPHT) reservoirs (Aadnøy & Looyeh, 2011). The complex problem includes rock mechanics, stress analysis, in-situ stress calculations, pore pressure prediction, shale/fluid chemical reactions and thermal stimulation (Farrokhrouz & Asef, 2013).

To prevent this problem, a balance between the stress and strength must be restored and maintained during drilling, while chemical, thermal and hydraulic driving forces must be controlled. The drilling fluid composition, mud weight, well trajectory and many other factors needs to be planned in advance. The failure mechanisms are tensile and collapse (Aadnøy & Looyeh, 2011). In this thesis, the focus will be on collapse. Collapse generally occurs due to a too low mud weight, and too high hoop stresses around the wellbore wall. There are many wellbore problems that are connected to collapse, such as fill, washouts, clay swelling, differential sticking and tight hole (Aadnøy & Chenevert, 1987). Figure 2.4 illustrates the different scenarios for a stable and unstable well.

6
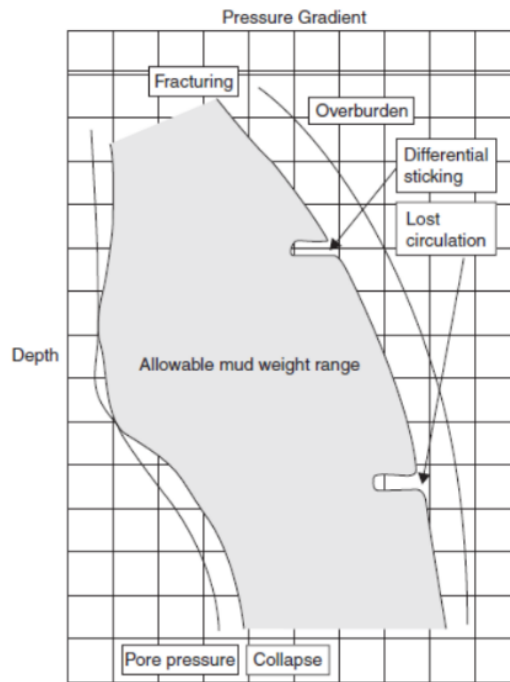
FIGURE 2.4: BOREHOLE PRESSURES WITH THE ALLOWABLE MUD WEIGHT WINDOW (AADNØY, 2010)

The estimated overall expenses of wellbore instability costs the industry an average of 8 billion dollars a year (Soroush, 2013). Out of this, 41% of the cost is due to non-productive time (NPT). Nearly 90 % of the problems occur in shale (Steiger & Leung, 1992). Shale makes up to three fourths of drilled formations, and because of this fact and considering the potential instabilities it may cause, it is treated with with precaution (Farrokhrouz & Asef, 2013). As shales are very sensitive to water, they are probably the weakest formation encountered while drilling. Problems generally occur as a result of abundant swelling clay minerals in the shales. It is commonly seen as caving and sloughing in shale. The resulting scenarios are hole enlargement, bridges and fill which leads to stuck pipe, lost circulation, and difficulties with running casings and interpreting logs. These problems are frequently associated with high pore pressure.

A typical wellbore instability problem in shales, is chemical interactions with the drilling fluid. This meaning shale hydration, swelling and dispersion as well as dissolution of soluble formations. Mechanical stresses also yields problems such as tension failure (fracturing and lost circulation) and compression failure (spalling and collapse). Erosion may also become a problem in shale zones. Occasionally wellbore instability leads to sticking of the drill pipe due to large fragments of brittle shale (>100 cm^3) which breaks off the wellbore walls. Solving this problem requires postponement of the drilling operation and significant additional costs. (Yu, et al., 2002).

As shales do not react with oil-based muds, this solves the swelling problem. However, because of environmental and economic concerns, the usage of oil-based muds have been less frequent. Oil muds are more prone to environmental damage and cost more than the common water based muds. With increasing environmental demands regarding oil-based drilling fluids, the use of water based muds (WBM) is growing. Observations show that the swelling of the shales are related to the activity of the water and the properties of the solute present in the liquid phase of the mud. In fact, it is the imbalance between the mud and the shale in the water activity which generates osmotic flow of ions and water resulting in instability. Fortunately WBMs may be designed to inhibit shale swelling. By implementing additives or inhibitors to the mud, satisfying properties of the drilling fluid may be achieved.

2.1.2   Characteristics of a Shale Formation

Shales are fine-grained rocks (finer than 0.0039 mm), composed of silt-sized particles plus a significant component of flakes of clay minerals (Grotzinger & Jordan, 2010). The thin layers make the shale fissile, and causing them to break along parallel layering or bedding planes. The laminated structure is what makes the shale unique compared to other mud rocks. Lamination thickness usually ranges from 0,1 to 0,4 mm (Farrokhrouz & Asef, 2013). Figure 2.5 shows laminated shale seen from a Scanning Electron Microscope (SEM). Shale is the result of compaction diagenesis of mud and is usually deposited by low-energy currents. The calm currents allow the fine particles to settle slowly to the bottom.
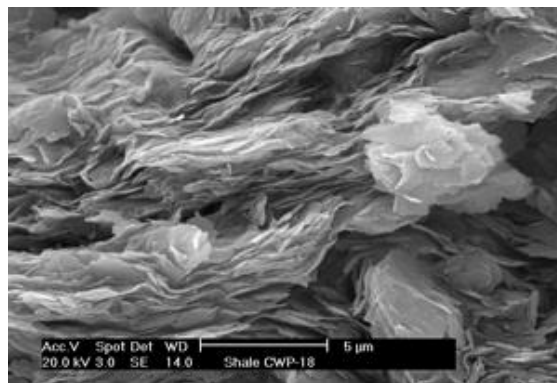
FIGURE 2.5: LAMINATED SHALE (SHAW & WEAVER, 1965)

The clay content in shales is the main reason for the several problems occurring while drilling through these formations. The common clay minerals represented montmorillonite, illite, smectite and kaolinite. It also usually consist of quartz, feldspar and carbonate grains.

Shale is typically categorized between soft (ductile) and hard (brittle) features. The soft shales commonly occurs in shallower depths, and due to this, they have high porosity and high water content. These shales consists of smectite and illite and are associated with swabbing, lost circulation, wash out and pack off. The color of the shale is generally gray, but it mostly depends on the mineral content. Green, brown or red shales indicate the content of iron oxide, while a black color indicates a source of organic matter.

The density shales ranges from 2.65-2.8 g/cm^3, while the porosity ranges from approximately 2-20 % (Ludovic, et al., 2012). Due to narrow pore sizes in the matrix, shales are known to possess extremely small, yet widely unpredictable permeabilities. The range of permeability is approximately $1 \times 10^{-18} \text{m}^2$ to $1 \times 10^{-21} \text{m}^2$ (Farrokhrouz & Asef, 2013).They are therefore often known as typical cap or seal rocks in a petroleum depositional system. Figure 2.6 show the permeability of several rock types, where it should be noted that shale has the lowest permeability of the sedimentary rocks.
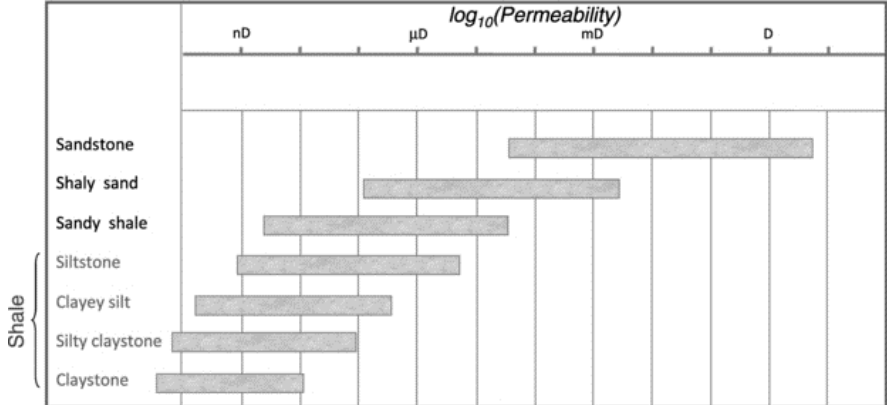
FIGURE 2.6: GENERAL RANGE OF PERMEABILITIES REPORTED IN THE LITERATURE FOR SHALES AND ASSOCIATED ROCKS (LUDOVIC, ET AL., 2012)

Along with the low permeability, shales also tend to have low porosities. In general, if porosity decreases, the permeability decreases logarithmically. Also the strength of shale is to decrease in a nonlinear manner with increasing porosity (Farrokhrouz & Asef, 2010). The pore mean radius is another element, which has an impact on the permeability, as an increasing radius will increase the diameter of pathway for the fluids to flow.

Table 2.1 shows typical parameter values for shale. As a few of these parameters were not available for this study, the given values by (Chen, et al., 2001) were considered to be realistic during the simulation in this thesis.

TABLE 2.1: LIST OF INPUT PARAMETERS FOR MODELING (CHEN, ET AL., 2001)

Variables	Symbol	Value	Unit
Shale activity	a_{wsh}	0.915	Dimensionless
Mud activity	a_{wm}	0.78	Dimensionless
Membrane efficiency	I_m	0.1	Dimensionless
Geothermal gradient	G_g	2	°K/100 m
Overburden gradient	σ_v	0.01945	MPa/m
Minimum horizontal in-situ stress gradient	σ_h	0.01877	MPa/m
Maximum horizontal in-situ stress gradient	σ_H	0.01877	MPa/m
Mud gradient	M_w	0.0180	MPa/m
Pore pressure gradient	p_o	0.01538	MPa/m
Depth (TVD)	D	4352.5	m
Well azimuth	A_{zim}	30	Degree
Well inclination	I_w	0	Degree
Wellbore radius	r_w	0.127	m
Drained Poisson's ratio	v	0.22	Dimensionless
Biot's parameter	α	0.80	Dimensionless
Tensile strength	σ_t	0.689	MPa
Initial cohesive strength	C_0	8.736	MPa
Equilibrium cohesive Strength	C_e	5.192	MPa
Cohesion alteration Factor	a^*	-0.5	Dimensionless
Shale Young's modulus	E	6895	MPa
Failure criteria		Drucker-Prager	
Friction angle	ϕ	30	Degree
Time	t	0, 8640, 86,400, 864,000	s
Pore fluid or mud hydraulic diffusivity	c	3.40e-10	m^2/s
Thermal diffusivity of porous media	c_0	9.54e-7	m^2/s
Coupling coefficient	c_0'	4.25e-14	m^2/s-MPa
Coupling coefficient	c'	0.124	MPa/°K
Volumetric thermal expansion coefficient of pore fluid (water)	α_f	5e-4	°K^{-1}
Volumetric thermal expansion coefficient of rock matrix (shale)	α_m	2.59e-5	°K^{-1}
Wellbore wall temperature	T_w	350.7	°K
Rock initial temperature	T_0	375.7	°K

2.1.3 Anisotropy of Shale

Anisotropy indicates that the properties of a material is directionally dependent. Isotropy is the opposite of anisotropy, and implies equal properties in all directions. Figure 2.7 illustrates the difference between isotropic and anisotropic deformation of a borehole. Most materials show

anisotropic behavior and the most common rock-forming minerals are usually anisotropic (i.e. quartz and feldspar). The strength and hardness of anisotropic materials varies for the exact same sample measured in several orientations.
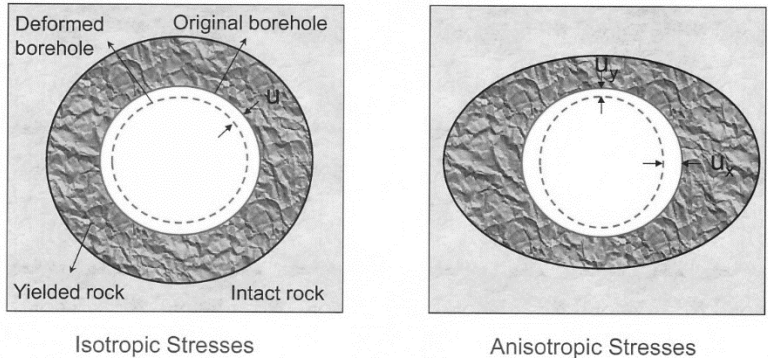
FIGURE 2.7: BOREHOLE DEFORMATION. ISOTROPIC VS. ANISOTROPIC STRESSES (CHEN, ET AL., 2001)

The difference between horizontal and vertical permeability might also be of significance when dealing with anisotropic rock formations in oil wells. When the in-situ stresses are anisotropic, a potential failure will have implications for the direction of the maximum horizontal stress. Typically, the borehole will then become elliptic (Chen, et al., 2001). Figure 2.8 and Figure **2.9** illustrates the principles of anisotropic compressive strength and inclination of beddings.
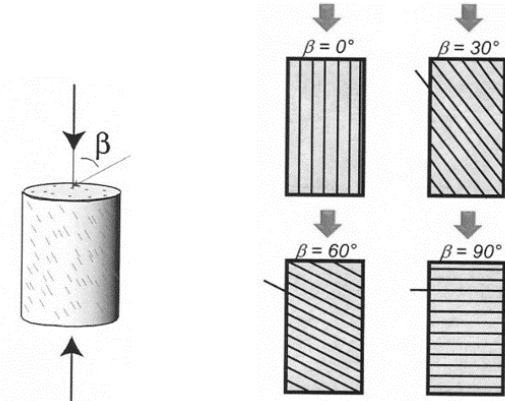
FIGURE 2.8: ANISOTROPIC EFFECT ON COMPRESSIVE STRENGTH (SOROUSH, 2013)

Clastic sediments may develop anisotropic properties both during and after deposition. While periodic layering produces beds of varying material or grain size, the directionality of the transporting medium also affects the ordering of the grains. Hence, anisotropy depends on both the variation of material and the variation of the arrangement and grain size.

In a sedimentary basin, shales are quite abundant and show a relatively high degree of anisotropy. During seismic exploration of oil, shales will act as proper seismic reflectors and provide information regarding petrophysical properties, which is important for exploration and reservoir management within a medium in motion. Particles are then displaced and a force proportional to the displacement acts on the particles, and tries to bring them back to their original position.

2.1.3.1   Elastic Wave

An elastic wave will propagate when a material is elastic and the particles in a specific region are vibrating. For example, sound is transmitted by gas as an elastic wave, as gas is an elastic medium. For correlating purposes, such as comparing sonic logs in deviated and vertical wells, detecting and quantifying this type of anisotropy is important. Other examples of common uses of anisotropic correlations are studies of amplitude variation with offset and borehole and surface seismic imaging (Yenugu, 2010).

2.1.3.2   Elastic Parameters from Wave Velocity

As mentioned above, shales tend to have anisotropic properties, due to the natural lamination of the rock. The anisotropy is reflected in the acoustic velocities of the shale (Stjern, et al., 2003). The velocity of elastic waves depends on several parameters such as density, porosity,

grain size, mineralogy, water content/absorption, temperature and stress level (Soroush, et al., 2010). By assuming an anisotropy and a travel direction along the well for the acoustic wave, the corresponding P-wave (compressional) velocity may be estimated for a given inclination. The uniaxial compressive strength might also be estimated from these velocity values.

While predicting analysis for sanding and wellbore instability, formation elastic parameters such as Young's modulus and Poisson's ratio are used as input parameters. They are commonly known as static elastic properties and are estimated by laboratory experiments on core samples. In 1974 Gardner (Gardner, et al., 1974) empirically derived an equation that relates seismic P-wave velocity to the bulk density of the lithology in which the wave travels. The equation reads:

$$\boldsymbol{\rho = \alpha_{GR} V_p^{\beta_{GR}}} \tag{2.1}$$

Where ρ is the bulk density in g/cm^3, V_p is the P-wave velocity given in ft/s , α_{GR} and β_{GR} are empirically derived constant depending on the lithology. By assuming a good fit by taking $\alpha_{GR} = 0,23$ and $\beta_{GR} = 0,25$ (Gardner, et al., 1974) the equation reduces to the following:

$$\boldsymbol{\rho = 0,23 V_p^{0,25}} \tag{2.2}$$

The above-mentioned constants are usually calibrated from density and sonic well logs, but Gardner's constants may be applied if these logs are not available.

2.1.3.3   Log Responses in a Shale Formation

The logging responses deducted from shale formations are commonly known by geophysicists because shales are good reflectors of signals and as they are abundant in a petroleum sedimentary basin. When interpreting the logs it is essential to consider where there are thin layers, or mixed formations (i.e. sandy shale), and (of course) if the formation contains fluid. In this section, several logs are presented and the responses they display in shale formations.

The Caliper Log records the hole diameter by rotating one or more arms attached. This log will indicate when the shale is causing caving (enlarged hole diameter) or sloughing (tight hole).

The Gamma Ray Log measures the natural gamma ray level in the formation. Shale will show high gamma ray radiation (24-1000 API), while sandstone and carbonate will show low (18-160 API) (Rider & Kennedy, 2012).

The Resistivity Log measures formation resistivity by electric currents. High resistivity readings indicates high hydrocarbon content as hydrocarbon is a non-conductive fluid, while low resistivity readings implies high water content in the formation (i.e. "wet sand") as water is a conductive fluid. Hence, this log is the most proper for hydrocarbon determination. There are two common resistivity logs used in the oil industry, Induction Log and Laterolog Log. The Induction Log measures formation resistivity by a transmitter and receiver which measure the resistivity of the formation by inducing current flow. The resistivity in shale varies extremely and is between 0.5-1000 ohm-m, while the readings from sandstone are generally up to 1000 ohm-m (Rider & Kennedy, 2012). This log represent shallow, medium and deep resistivity. As shale is a non-permeable zone, the log does not separate between deep and medium resistivity in shale.

Density Log measures the bulk density of the formation, which subsequently may be related to the porosity once the lithology is known. Common readings are 2,65 - 2,7 gm/cc in shale and 2,59-2,84 gm/cc in sand (Rider & Kennedy, 2012).

Neutron Log measures the formation's ability to attenuate the passage of neutron through the formation. It is a measure of hydrogen content, which represents presence of water or oil in the formation. The readings of this log in shale formations will be high and range between 25-75% due to water trapped inside the formation (Rider & Kennedy, 2012). The readings in oil or water zones will have the fraction equal to 1 (Rider & Kennedy, 2012).

Sonic Log measures the minimum time required by a compression wave to travel vertically one foot of formation adjacent to the wellbore. The Sonic Travel Time may be related to porosity whenever the lithology is known. The unit of travel time is microseconds per foot. Typical sonic log readings for shale is 62,5-167 μs/ft (Rider & Kennedy, 2012). Figure 2.10 shows a simple explanation of the different logs above.
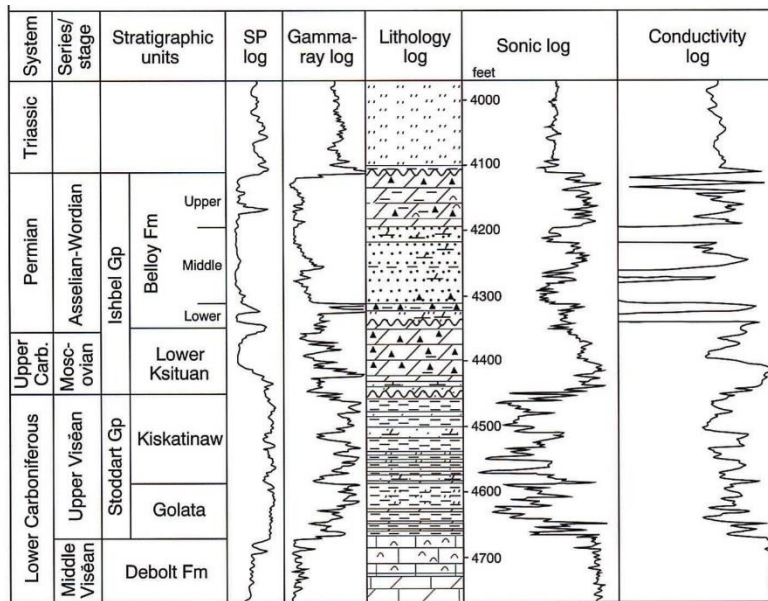
FIGURE 2.10: ILLUSTRATION OF A TYPICAL WELL LOG (HENDERSON, ET AL., 2012)

2.2 Rock Mechanics

Rock mechanics is the theoretical and applied science of the mechanical behavior of rocks in the force fields of their physical environment (Soroush, 2013). Geomechanics is the mechanical behavior of all geo-materials, including soils. Petroleum geomechanics is the discipline that involves rock mechanics, geophysics, petrophysics and geology to quantify the response of the Earth's changes in stresses, reservoir pressure and formation temperature. It applies the principles of rock mechanics to predict the failure of porous, granular, discontinuous, heterogeneous, and anisotropic materials under high stress and high temperature condition. Figure 2.11 display three typical stress regimes, also called faults. The purpose of studying geomechanics is to reduce NPT (Non-Productive Time), deduct costs and to reduce risk. By fault leakage and geomechanic analysis of a rock, the exploration risk reduces.
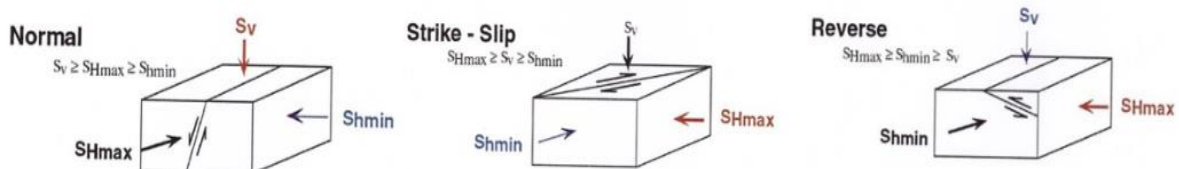
FIGURE 2.11: ANDERSON'S CLASSIFICATION OF STRESS REGIMES (FAULTS) (SOROUSH, 2013)

During drilling, analysis of the rock formation will provide a more accurate and safe operating mud window, which will reduce kicks and lost circulation. It will also improve wellbore stability, by reducing stuck pipe, sidetracks, washing and reaming. During production, it improves fluid flow from natural fractures, predicts and manages sand production, optimizes hydraulic fracturing operation, and reduces casing shear and collapse.

A geomechanical model includes vertical stress (σ_V), maximum horizontal stress (σ_{Hmax}), minimum horizontal stress (σ_{hmin}), stress direction ($\sigma_{Hmax, AZI}$), pore pressure (P_P) and rock strength (UCS).These stresses can be used to analyze borehole problems such as fracturing, lost circulation, collapse and sand production. Vertical stress is always the greatest stress and one principal stress is always vertical. Open fractures are perpendicular to σ_{hmin} direction. Horizontal wells drilled in the σ_{Hmax} direction are most stable (Soroush, 2013).

Geomechanics of shale differs from conventional reservoirs due to inelastic matrix behavior, stress sensitivity, rock anisotropy (laminations and natural fractures), rock rheology, low matrix permeability (Soroush, 2013). Consequently, the mechanical properties of the shale will vary with the applied load. Because of the anisotropy, the properties parallel and perpendicular to the bedding planes are individual. During drilling, it is essential to understand these properties as these have major impact on the drilling operation and well stability. Nevertheless, while the drilling mud weight is designed, the geomechanical properties of the shale should be considered. Table 2.2 presents interesting differences between conventional and shale geomechanics.

Conventional geomechanics vs. Shale		
Subject	Conventional	Shale
Wellbore instability	Dominated by mechanical failure	Dominated by physic chemical effects
Rock behavioral models	Elastic to elastoplastic	Inelastic
Rock mechanical characteristics	More brittle	More ductile
Rock properties	Isotropic to anisotropic	Usually transversely isotropic (TI)
Stress regime	Usually anisotropic	Less anisotropic to isotropic
Rock- fluid interaction	Mechanical	Mechanical- chemical
Natural fractures	Close/open depends on their orientation	Healed/less permeable
Borehole enlargement	More breakout	More washout
Pore pressure estimation	Measurement	Prediction
Hydraulic fracturing efficiency	Higher	Lower
Depletion related deformation	Faulting	Compaction

2.2.1 Mechanical Properties of Shale

2.2.1.1 Stress

Stress is the force acting over an area (any surface). Stresses have both magnitudes and orientation. The stress on a plane may be broken into two components, one perpendicular to the plane face, the normal stress (σ), and the other parallel to the plane, the shear stress (σ_{xy}). Stress at a point in the subsurface is defined in terms of three normal stresses and six shear stresses. For normal stress components, we usually use only one subscript i.e. σ_x not σ_{xx}. (Soroush, 2013):

$$Stress = \sigma = \frac{F(Force)}{A(Area)} \qquad (2.3)$$

2.2.1.2 Strain

The definition of strain is the change in length per original length due to an applied load. Strains are categorized as "scientific strains" and "engineering strains". The initial/original dimension is used for engineering strain, and the actual dimension (which changes with time) is applied for scientific strain.

$$Strain = \varepsilon = \frac{\Delta L(change\ in\ length)}{L(initial\ length)} \qquad (2.4)$$

The fundamental relation between stress and strain is Hookes Law:

$$\sigma = E\varepsilon \qquad (2.5)$$

By combining the equation for stress and strain into Hookes Law, one can derive the load-deformation as:

$$\Delta L = \frac{FL}{EA} \qquad (2.6)$$

As stress cannot be measured directly, strain (deformation) is usually measured in-situ or in the laboratory, before stress is calculated. Stress and strain are proportional to each other through a simple linear relationship shown in Figure 2.12 below. Engineers use stress-strain diagrams to safely design wells and steel constructions, exposed to static loads. The following stress-strain curve illustrates a clear transition between linear elastic to plastic for steel materials. One can easily read the yield stress from the curve (i.e. the lower yield point), showing a clear transition between linear elastic to plastic.
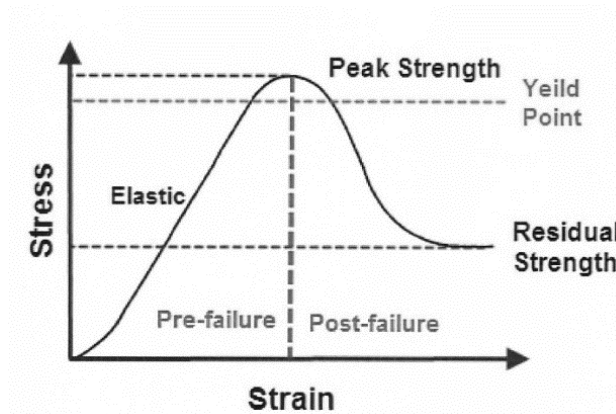
FIGURE 2.12: A TYPICAL STRESS-STRAIN CURVE (SOROUSH, 2013)

The "Ultimate Tensile Strength" is the maximum load the material can be exposed to before it fails. The "yield point" is the stress at transition zone between elastic and plastic region. This point is the reference point for noting the strength of a material.

2.2.1.3   Young's Modulus

Young's modulus, also known as Modulus of Elasticity, E, is a measure of the stiffness of a material. It is applicable to a linear elastic region where stress is directly proportional to strain. The slope (i.e. E) is given as:

$$E = \frac{\Delta\sigma}{\Delta\varepsilon}$$

(2.7)

The elastic parameter Young's modulus is established by sonic wave velocity. This parameter considers temperature and other changing factors down in the wellbore.

2.2.1.4   Poisson's Ratio

Poisson's ratio for axial member is a material property that predicts the lateral strain as a ratio of the axial strain. This relationship is given by:

$$v = \frac{-\varepsilon_l}{\varepsilon_a}$$

(2.8)

Where ε_l is the strain in the lateral direction and ε_a is the axial strain.

2.1.1.1   Uniaxial Compressive Strength (UCS)

Uniaxial compressive strength is the strength of the rock while it is compressed in a uniaxial direction, without lateral restraint. It is defined by the following equation (Fjær, et al., 2008):

$$UCS = C_0 = 2S_0 \tan\beta_{UCS}$$

(2.9)

Where S_0 is the cohesion strength, the ability of molecules sticking together under tensile loading and resist deformation, while β_{UCS} is the orientation of the failure plane. The cohesive force, is the force attracting two touching molecules. Figure 2.13 shows the different failure phases of the material during uniaxial compressive loading.
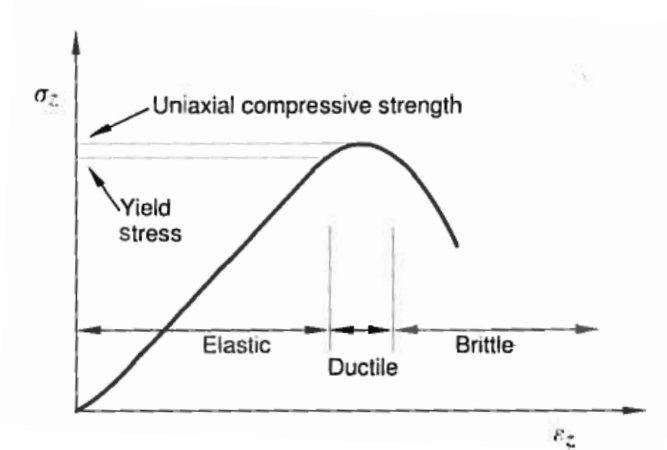
FIGURE 2.13: ILLUSTRATION OF STRESS AS A FUNCTION OF STRAIN (DEFORMATION IN A UNIAXIAL COMPRESSION TEST) (FJÆR, ET AL., 2008)

2.1.2   Stress Components

Imagine a perfect cube with six equal sides. The law on balance of forces suggests that stress components may be transformed by defining random planes inside the cube. This law states that identical stresses act in different directions on each of the side. Nine stress vectors are established for the cube. Three normal stress vectors σ_{xx}, σ_{yy} and σ_{zz}, and six shear stress vectors τ_{xy}, τ_{yx}, τ_{xz}, τ_{zx}, τ_{yz} and τ_{zy}. The indexes defines the axis normal to the plane(first) and the direction of the stress component (second). Two identical indexes implies normal stresses and are given with only one index, e.g. $\sigma_{xx} = \sigma_x$.

The shear stresses in opposite directions become equal when the object is at ease or non-rotating:

$$\tau_{xy} = \tau_{yx}, \tau_{xz} = \tau_{zx} \ and \ \tau_{yz} = \tau_{zy} \qquad (2.10)$$

The stress state can be defined as a matrix by three normal and three shear stresses:

$$[\sigma] = \begin{bmatrix} \sigma_x & \tau_{xy} & \tau_{xz} \\ \tau_{xy} & \sigma_y & \tau_{yz} \\ \tau_{xz} & \tau_{yz} & \sigma_z \end{bmatrix} \qquad (2.11)$$

While rotation, all of the shear stresses will be neglected, leaving only the three normal stresses left, also known as the principal stresses.

$$[\sigma] = \begin{bmatrix} \sigma_x & 0 & 0 \\ 0 & \sigma_y & 0 \\ 0 & 0 & \sigma_z \end{bmatrix} \qquad (2.12)$$

When an element (in any component) is in a highly specific orientation, such that the only resultant stresses are normal stresses, these are called "principal stresses". Principal stresses are essential for predicting rock failure. Two principal stresses are in the horizontal plane and most shear failure criteria comprise two or three principal stresses.

2.1.2.1   In-Situ Stresses

In-situ stresses are stresses exerted on sediments, at equilibrium or undisturbed state. They are also called far-field stresses. In-situ stresses comprise horizontal and vertical stresses. The vertical stresses are owed to overburden stresses from the overlying rocks and horizontal stresses are due to overburden, tectonic and geological depositions. However, geologists differentiate between paleo-stress and in-situ or contemporary stress. Paleo-stress is stress that earlier, in a specific geological period, acted upon the given rocks. In-situ or contemporary stress are stresses which may be implied by plate motion, earthquakes or borehole data (Dorkhabi, 2014). Figure 2.14 illustrates tensoral general in-situ stresses.
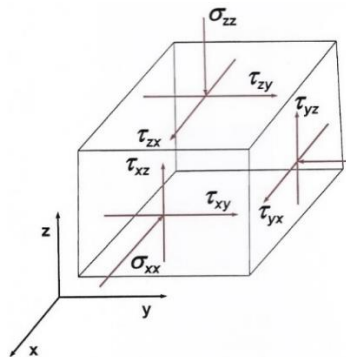
FIGURE 2.14: TENSORAL REPRESENTATION OF GENERAL IN-SITU STRESSES (**SOROUSH, 2013**)

2.1.2.2 Vertical Stress

Vertical stress σ_v is mainly due to the weight of overlying formations and the fluids they contain, and is known as Overburden Stress. Vertical stress may also include stresses resulting from geological conditions such as magma or salt dome intruding in the surrounding areas of the rock formation. The overburden stress have the ability to spread and expand the underlying sediments in horizontal lateral directions, due to the effect of Poisson's Ratio. The overburden stress increases in depth as the number of overlying sediments increases. While formations are

homogenous, the vertical stress is given by $\sigma_v = \rho g z$. If the formations are not homogenous, the density will vary and the equation below has to be applied to determine the overburden stress.

$$p(z) = p_0 + g \int_0^z \rho(z)\, dz \qquad (2.13)$$

Where *p(z)* is the overburden pressure at depth z, p_0 is the datum pressure (i.e. at surface), *g* is the acceleration due to gravity on Earth and ρ_o is the density of the overlying rock at depth z.

2.1.2.3 Horizontal Stresses

Horizontal stresses are caused by lateral movement of the overburden stress which are restricted by the presence of adjacent materials. These stresses are known as maximum,σ_H and minimum σ_h horizontal stresses. Underground formations are affected by horizontal stresses when sediments are moving in horizontal directions in addition the the vertical stress impact. However, in this case the rock is assumed to be isotropic, but in real life situations rock formations cannot always be treated as isotropic and homogeneous. Poroelastic theory might have to be used for some cases. When tectonic forces are not present, the horizontal stresses may be neglected.

For vertical fracture, the minimum horizontal stress can be estimated using the equation (Fjær, et al., 2008):

$$\sigma_h = \frac{v}{1-v}\left(\sigma_v - \alpha_{Biot}P_p\right) + \alpha_{Biot}P_p + \sigma_{ext} \qquad (2.14)$$

Where σ_h = minimum horizontal stress, σ_v = overburden, P_p = pore pressure, α_{Biot} = Biot constant and σ_{ext} = tectonic stress. v is Poisson's ratio and can be estimated from acoustic log data or lithology correlations.

2.1.3 Stresses around a Wellbore

Underlying formations are at all times in a stressed state, caused by tectonic and overburden stresses. Figure 2.15 gives a simplified illustration of stresses around a wellbore. While drilling a well, the existing stresses in the solid material changes. After a while, the borehole wall is only supported by hydrostatic fluid column in the well.
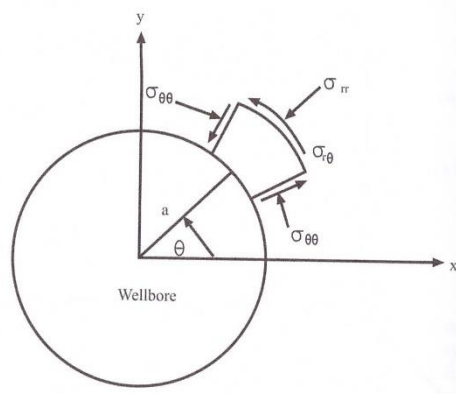
However, as the in-situ stresses generally do not match the hydrostatic fluid column pressure, there will be a stress redistribution around the well. Figure 2.16 shows a simplified drawing of the stress distribution for a deviated well. Managing and correlating the stresses is highly demanding in order to avoid failure. Hence, knowledge of the wellbore stresses is needed to ensure wellbore stability (Fjær, et al., 2008).
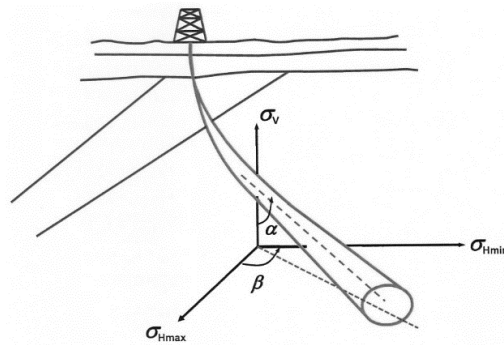
FIGURE 2.16: STRESSES IN DEVIATED WELLS (SOROUSH, 2013)

Ernst Gustav Kirsch was a German engineer who introduced equations for describing the elastic stress state around a circular hole in an infinite plate with unidirectional (one-dimensional) tension. The Kirsch Equations are widely used for vertical boreholes with diverse far-field stresses. He also proposed equations for shear stresses. Bernt S. Aadnøy derived the equations accordingly (Aadnøy & Looyeh, 2011):

$$\sigma_r = \frac{1}{2}(\sigma_x + \sigma_y)\left(1 - \frac{a^2}{r^2}\right) + \frac{1}{2}(\sigma_x - \sigma_y)\left(1 + 3\frac{a^4}{r^4} - 4\frac{a^2}{r^2}\right)cos2\theta + \tau_{xy}\left(1 + 3\frac{a^4}{r^4} - 4\frac{a^2}{r^2}\right)\sin 2\theta + \frac{a^2}{r^2}P_w \qquad (2.15)$$

$$\sigma_\theta = \frac{1}{2}(\sigma_x + \sigma_y)\left(1 + \frac{a^2}{r^2}\right) - \frac{1}{2}(\sigma_x - \sigma_y)\left(1 + 3\frac{a^4}{r^4}\right)cos 2\theta - \tau_{xy}\left(1 + 3\frac{a^4}{r^4}\right)\sin 2\theta - \frac{a^2}{r^2}P_w \qquad (2.16)$$

$$\sigma_z = \sigma_{zz} - 2v(\sigma_x - \sigma_y)\frac{a^2}{r^2}cos2\theta - 4v\tau_{xy}\frac{a^2}{r^2}sin2\theta \rightarrow \textit{Plane strain} \tag{2.17}$$

$$\sigma_z = \sigma_{zz} \rightarrow \textit{Plane stress}$$

$$\tau_{r\theta} = \left[\frac{1}{2}(\sigma_x - \sigma_y)sin2\theta + \tau_{xy}cos2\theta\right]\left(1 - 3\frac{a^4}{r^4} + 2\frac{a^2}{r^2}\right) \tag{2.18}$$

$$\tau_{rz} = (\tau_{xy}\cos\theta + \tau_{yz}sin\theta)\left(1 - \frac{a^2}{r^2}\right) \tag{2.19}$$

$$\tau_{\theta z} = (-\tau_{xz}sin\theta + \tau_{yz}cos\theta)\left(1 + \frac{a^2}{r^2}\right) \tag{2.20}$$

2.1.3.1 Stress Transformation

In most cases, a well is oriented and has an azimuth (α) and/or an inclination(i). The in-situ stresses then need to be transformed into the new coordinate system. Figure 2.17 shows a simple explanation of the meaning of stress transformation. In order to determine the magnitudes and orientations of the stress or strain components transformation equations must be applied.
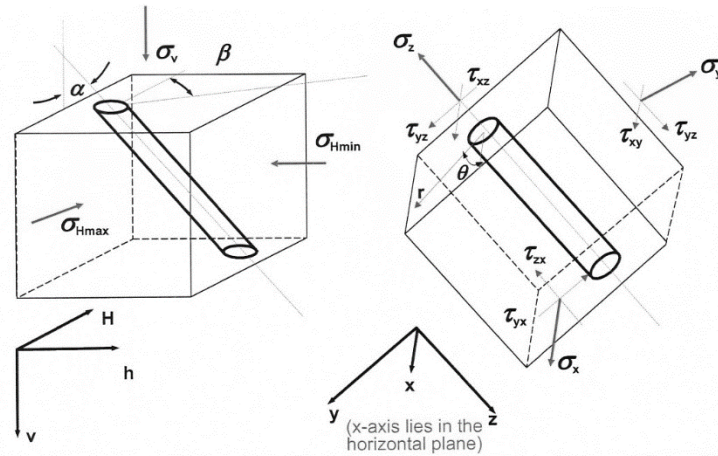
FIGURE 2.17: TRANSPOSE OF IN-SITU STRESSES TO A WELL COORDINATE SYSTEM (SOROUSH, 2013)

Bernt S. Aadnøy derived the equations accordingly (Aadnøy & Chenevert, 1987):

$$\sigma_{xx} = (\sigma_h \cos^2\varphi + \sigma_H \sin^2\varphi)\cos^2\gamma + \sigma_v\sin^2\gamma \tag{2.21}$$

$$\sigma_{yy} = \sigma_h \sin^2\varphi + \sigma_H \cos^2\varphi \tag{2.22}$$

$$\sigma_{zz} = (\sigma_h \cos^2\varphi + \sigma_H \sin^2\varphi)\sin^2\gamma + \sigma_v\cos^2\gamma \tag{2.23}$$

$$\tau_{xy} = \frac{1}{2}(\sigma_H - \sigma_h)\sin2\varphi\cos\gamma \tag{2.24}$$

$$\tau_{yz} = \frac{1}{2}(\sigma_H - \sigma_h)\sin2\varphi\sin\gamma \tag{2.25}$$

$$\tau_{xz} = \frac{1}{2}(\sigma_h \cos^2\varphi + \sigma_H \sin^2\varphi - \sigma_v)\sin2\gamma \tag{2.26}$$

2.1.4   Principal Stresses

The definition of principal stresses is that for the principal stress orientation on the faces, the shear stresses are zero. The principal stress components are ordered such that $\sigma_1 > \sigma_2 > \sigma_3$. Vertical stress, σ_v, is usually assumed to be a principal stress component, as such, the other two components lie in the horizontal plane and is designated σ_{Hmax} and σ_{hmin} (Soroush, 2013). Figure 2.18 explains the principal stresses as wellbore stresses.
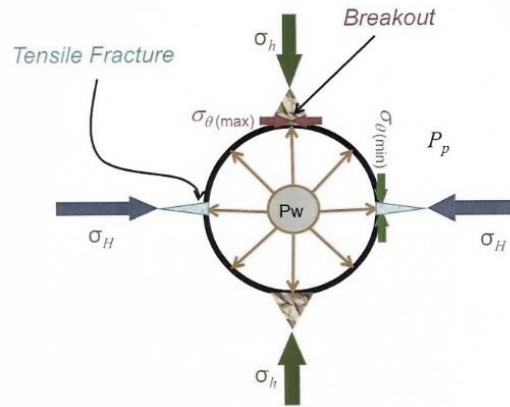
FIGURE 2.18: NEAR WELLBORE STRESSES (SOROUSH, 2013)

Anyhow, principal stresses may be estimated once the shear and the normal stresses are established. Applying the equation below, the stress vector at the wellbore wall, $(r = a)$, is equal to:

$$[\sigma] = \begin{bmatrix} \sigma_r & 0 & 0 \\ 0 & \sigma_\theta & \tau_{\theta z} \\ 0 & \tau_{z\theta} & \sigma_{zz} \end{bmatrix} \tag{2.27}$$

Bernt S. Aadnøy derived the equations for principal stresses accordingly (Aadnøy & Looyeh, 2011):

$$\sigma_1 = P_w \tag{2.28}$$

$$\sigma_2 = \frac{1}{2}(\sigma_\theta - \sigma_{zz}) + \frac{1}{2}\sqrt{(\sigma_\theta - \sigma_{zz})^2 + 4\tau_{\theta z}^2} \tag{2.29}$$

$$\sigma_3 = \frac{1}{2}(\sigma_\theta - \sigma_{zz}) - \frac{1}{2}\sqrt{(\sigma_\theta - \sigma_{zz})^2 + 4\tau_{\theta z}^2} \tag{2.30}$$

2.2 Driving Forces

Thermal and chemical effects are highly crucial when drilling into shale formation as they may influence the collapse and tensile strength significantly. Experiments performed by Mody & Hale (Chen, et al., 2001) showed that the original pore pressure increased due to these effects.

Chemical effects are generally caused by osmosis. Osmosis is the transport of solvent through a semipermeable membrane from the dilute solution side to the concentrated solution side of the membrane. It is driven by chemical potential differences between the water on either side of the membrane. With and ideal semipermeable membrane, only water should permeate through the membrane (Cheryan, 1998).

Osmosis is a function of two important factors, namely the water activity of the drilling fluid and of the formation. The chemical effect caused by a difference between the shale formation water activity and the drilling fluid water activity is equivalent to the hydraulic potential in a system (Cheryan, 1998). Membrane efficiency is estimated as the ratio of the observed osmotic pressure by the theoretical osmotic pressure. The osmotic pressure is the force per unit area required to prevent water passing through a semi-permeable membrane into an area of high solute concentration (Cheryan, 1998).

As the pore pressure is influenced by the osmotic effect, the wellbore stresses are also impacted. The wellbore stresses may also be influenced by temperature changes in the well. These effects may be caused by fluids in the annulus with different temperatures, or even temperature that leads to volumetric expansion (Ewy & Chen, 2005). For a radial system, such as a wellbore, thermal and chemical effects are given by the following equations (Chen, et al., 2001):

$$\frac{\partial T}{\partial t} = c_o \left(\frac{\partial^2 T}{\partial r^2} + \frac{1}{r} \frac{\partial T}{\partial r} \right) + c'_o \left(\frac{\partial T}{\partial r} \frac{\partial P}{\partial r} + T \left(\frac{\partial^2 P}{\partial r^2} + \frac{1}{r} \frac{\partial P}{\partial r} \right) \right) \qquad (2.31)$$

$$\frac{\partial P}{\partial t} = c \left(\frac{\partial^2 P}{\partial r^2} + \frac{1}{r} \frac{\partial P}{\partial r} \right) + c' \frac{\partial T}{\partial t} \qquad (2.32)$$

Where T is temperature, P is pore pressure, c_o is the thermal diffusivity of a porous medium, c'_o is the coupling coefficient, and c' is the other coupling coefficient.

The thermal and hydraulic diffusivity may also be expressed by the following equations by Venkanna (Venkanna, 2010) and Cossé (Cossé, 1993) :

$$c = \frac{k}{\varphi \mu c_t} \tag{2.33}$$

Where k is the permeability, φ is the porosity, μ is the dynamic viscosity and c_t is the compressibility of fluid.

$$c_o = \frac{k_o}{\rho c_p} \tag{2.34}$$

Where k_o is the thermal conductivity, ρ is the density and c_p is the specific heat capacity.The two terms containing c_o, in equation 2.31, are the temperature changes due to heat conduction. The first term in the equation 2.31 containing c_o', is the temperature change due to heat convection and the second term is temperature due to pressure diffusion. However, the terms containing c, gives the pore pressure diffusivity due to hydraulic force, while the term containing c', gives the pore pressure ch5ange due to temperature variation (Ewy & Chen, 2005).

The convection term (equation 2.31) is negligible due to a low permeable formation (shale). The coupling coefficient (equation 2.31) can be disregarded due to the insignificant magnitude compared to the thermal diffusivity. Gathering the above assumptions, the above equation can then be simplified, as the whole term containing the coupling coefficient can be neglected (Chen, et al., 2001). Decoupling the above equations and considering the assumptions, the equations transforms to the following (Chen, et al., 2001):

$$\frac{\partial T}{\partial t} = c_o \left(\frac{\partial^2 T}{\partial r^2} + \frac{1}{r} \frac{\partial T}{\partial r} \right) \tag{2.35}$$

$$\frac{\partial P}{\partial t} = c \left(\frac{\partial^2 P}{\partial r^2} + \frac{1}{r} \frac{\partial P}{\partial r} \right) + c' \frac{\partial T}{\partial t} \tag{2.36}$$

2.2.1 Chemical Effects

The chemical potential due to osmosis in a system is estimated by the following equations by Mody and Hale (Chen, et al., 2001):

$$P_\pi = -I_m \frac{R_g T}{V} ln \frac{a_{df}}{a_{fw}} \tag{2.37}$$

Where P_π is the chemical potential, I_m is the membrane efficiency, R_g is the gas constant, T is thetemperature of the well wall, V is the partial molar volume of water, a_{df} is the activity of drilling mud and a_{fw} is the activity of shale. The membrane efficiency is kept in equation 2.37,

as shale does not have a permeable membrane while interacting with water. Hence, the partial membrane is considered when I_m, is in a range of 0.01-0.1 for shale (Chen, et al., 2001).

The magnitude of the activity of the drilling fluid and the activity of the formation water determines if the direction of the water movement is to be either inwards or outwards. Water activity is the ratio of vapor pressure of a given liquid divided by vapor pressure of pure water (Soroush, 2013). The activity is controlled by the salt content, meaning the salinity of the fluid. The higher the salinity, the lower the activity (Soroush, 2013). The flow of water containing salt will therefore influence the pore pressure due to osmosis.

An increase in pore pressure, leading to a decrease in the effective stresses in the wellbore, will result in a reduced collapse strength. If the pore pressure decreases, the result will be the opposite. However, if the pore pressure is altered due to chemical effects, the pore pressure will generally increase if moved away from the wellbore, and eventually decrease if it is observed moving away from the wellbore wall. This scenario is due to osmosis and the balancing of the hydraulic effect, and when the hydraulic effect exceeds this effect it results in a decrease of the pore pressure (Yu, et al., 2003). As seen, when water flows inwards due to osmotic effect, the pore pressure increases until it reaches a certain point, where it will slowly decrease again. When water comes out, the pore pressure increases only when as moving away from the wellbore wall. Furthermore, it should be noted that the pore pressure around the wall increases whenever the mud weight is altered due to higher hydraulic force on the wall, caused by the difference in initial pore pressure and the actual well pressure.

As illustrated in the below figure 2.19 and figure 2.20 the water molecules move from the higher activity to the lower activity. The pore pressure will increase or decrease (depending on the value of the activity) due to osmosis.
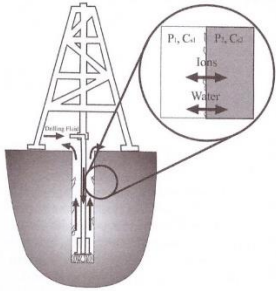
FIGURE 2.19: WELLBORE DRILLED IN A SHALE FORMATION (FARROKHROUZ & ASEF, 2013)
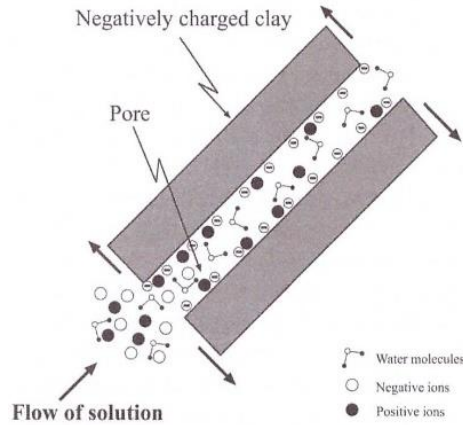
FIGURE 2.20: PORES IN A SHALE FORMATION IN CONTACT WITH A SALTED SOLUTION (FARROKHROUZ & ASEF, 2013)

2.2.2 Thermal Effects

Cooling the formation is needed to maintain wellbore stability. Hence, cooler muds may reduce the pore pressure and increase the collapse stress. On the contrary, hotter muds cause instability in the shales.

Thermal driving forces are important as thermal diffusion into shale formations develops faster than hydraulic diffusion and thereby dominates the pore pressure changes in the early stage (Chen, et al., 2001). The thermal diffusion induces further pore pressure and rock stress changes, which affects the wellbore stability (Chen, et al., 2001). In addition, temperature changes due to injection or production of fluids with different temperatures in the annulus may induce thermal stresses. The changes may also lead to volumetric expansion in the rock matrix and the pore fluid, which again will have an impact on the pore pressure (Ewy & Chen, 2005). Carlaw and Jeager (1959) simplified the equation 2.35 for short time and distance as following (Chen, et al., 2001):

$$T(r,t) = T_o + (T_w - T_o)\sqrt{\frac{r_w}{r}} \, erfc\left\{\frac{r-r_w}{2\sqrt{c_o t}}\right\} \tag{2.38}$$

29

Where T_o is the formation temperature, T_w is the well wall temperature, r_w is the well radius, r is the distance away from the wellbore center, $erfc$ is the complementary error function, c_o is thermal diffusivity and t is time.

By applying equation 2.38, the temperature profile may be estimated with respect to the specific radius and wellbore radius, at any time for minor distances. As the temperature varies, the effective stresses will change and affect the collapse strength.

An analytical solution to equation 2.36 was also derived in order to determine a pore pressure profile with respect to time and wellbore radius. The equation is presented below (Chen, et al., 2001):

$$p(r,t) = p_o + (p_w - p_\pi - p_o)\sqrt{\frac{r_w}{r}}\, erfc\left\{\frac{r-r_w}{2\sqrt{ct}}\right\} - \frac{c'(T_w - T_o)}{1-c/c_o}\sqrt{\frac{r_w}{r}}\left[erfc\left\{\frac{r-r_w}{2\sqrt{ct}}\right\} - erfc\left\{\frac{r-r_w}{2\sqrt{c_o t}}\right\}\right] \quad (2.39)$$

Where p_o is the initial pore pressure, p_w is the well pressure, and p_π is the chemical potential. The first term is the hydraulic diffusivity effect on the pore pressure, considering the difference between well pressure and the sum of chemical potential and initial pore pressure. The second term considers the temperature effects in the wellbore or the thermal diffusivity, which affects the pore pressure profile. If the wall temperature is higher than the formation temperature, the pore pressure will generally increase.

2.2.3   Chemical Effects

As temperature and pore pressure profiles are established, the stresses induced by hydraulics of the fluid flow and temperature, can be determined by the following equations (Chen, et al., 2001):

$$\sigma_{rr} = \frac{\alpha(1-2v)}{1-v}\frac{1}{r^2}\int_{r_w}^{r} p^f(r,t)rdr + \frac{E\alpha_m}{3(1-v)}\frac{1}{r^2}\int_{r_w}^{r} T^f(r,t)rdr + \frac{r_w^2}{r^2}P_w \quad (2.40)$$

$$\sigma_{\theta\theta} = -\frac{\alpha(1-2v)}{1-v}\left[\frac{1}{r^2}\int_{r_w}^{r} p^f(r,t)rdr - p^f(r,t)\right] - \frac{E\alpha_m}{3(1-v)}\left[\frac{1}{r^2}\int_{r_w}^{r} T^f(r,t)rdr - T^f(r,t)\right] - \frac{r_w^2}{r^2}P_w \quad (2.41)$$

$$\sigma_{zz} = \frac{\alpha(1-2v)}{1-v}p^f(r,t) + \frac{E\alpha_m}{3(1-v)}T^f(r,t) \quad (2.42)$$

Where E is Young's modulus, σ_{rr} is radial stress, $\sigma_{\theta\theta}$ is tangential stress, σ_{zz} is axial stress α_m is volumetric linear thermal expansion coefficient of rock matrix in K⁻¹. The first term in all of

the above equations is the induced stresses caused by the fluid flow, the second is due to thermal effects and the third term is due to well pressure. However, the third term is only applicable for pressures in a cylindrical profile. To modify this term to in-situ stresses in a well, the Kirsch's equations (2.15-2.20) may be coupled in order to determine the induced stresses due to well pressure and in-situ stresses around a wellbore. It should also be noted that the two first terms depend on Young's modulus, Poisson's ratio, volumetric expansivity and Biot's coefficient of the formation.

Removing the integrals from equations 2.40- 2.42, the stress equations may be simplified to (Chen, et al., 2001):

$$\boldsymbol{\sigma_{rr} = p_w} \tag{2.43}$$

$$\boldsymbol{\sigma_{\theta\theta} = \frac{\alpha(1-2v)}{1-v}(P_w - P_\pi - P_o) + \frac{E\alpha_m}{3(1-v)}(T_w - T_o) - p_w} \tag{2.44}$$

$$\boldsymbol{\sigma_{zz} = \frac{\alpha(1-2v)}{1-v}(P_w - P_\pi - P_o) + \frac{E\alpha_m}{3(1-v)}(T_w - T_o)} \tag{2.45}$$

Hence, final stress fields around the wellbore may be determined by coupling Kirsch's equations 2.15-2.20 with the above equations. Equation 2.44 is the combination of hydraulic and osmotic effect. An equation for only hydraulic effect is as following:

$$\boldsymbol{\sigma_\theta^{Hyd} = \alpha\frac{1-2v}{1-v}(P_w - P_0) - P_0} \tag{2.46}$$

2.2.4   Effects of Salts on the Mechanical Strength of Shale

Salts have proved to be beneficial in stabilizing shale formations. They lower the water activity, which increases the osmotic pressure gradients. The mobility of the solute is also low in shale which increases the membrane efficiency of the shale-mud system. The resulting outcome is a generated effective osmotic pressures which is able to offset the hydraulic mud over-balance and stability is restored through dehydration. In order to partially compensate the hydraulic inflow of mud filtrate, it is possible to use high-salinity fluids to stimulate the osmotic back flow of shale pore water towards the wellbore (Farrokhrouz & Asef, 2013). Examples of salt additives are Potassium Chloride (KCl), Sodium Chloride (NaCl), Calcium Chloride ($CaCl_2$), and Magnesium Chloride ($MgCl_2$) (Yu, et al., 2002).

2.3 Failure Criteria

A failure mode is a manner in which a rock failure may occur. In order to avoid failure, one needs to be prepared, take precautions and apply risk-reducing measures. The main rock failure modes in a well are tensile and collapse. For tensile failure, one uses the maximum-normal stress criterion, and for compressive failure, the maximum strain energy of distortion criterion is used. In order to use the correct components for the failure analysis, the in-situ stresses must be transformed. Isotropic stresses is assumed $\sigma_h = \sigma_H$. The overburden stress, σ_v, is either retrieved from a drilling mud program or calculated by using the densities and depths.

2.3.1   Collapse Failure Criteria and Collapse Model

When hydrostatic drilling fluid column pressure is too low, the structural integrity of the hole is reduced, and borehole collapse may occur. Shear failure occasionally develops due to high compressive loading on rock formations. The resulting problems are commonly drill pipe sticking and possible loss of well.

Faults develop as a result of the shear stresses exceeding the strength of the rock. The planes will thereby slide and separate from each other. The compressive loading and stresses around the wellbore will have an essential impact on the shape of the wellbore. The wellbore will maintain its circular form if the stresses are even and of same magnitudes. However, if the compressive loading is acting on several axes, the wellbore will deform. Nevertheless, collapse failure, may still occur in circular shaped wellbores. As this type of failure leads to several well stability problems, several analytical and numerical models have been established for controlling and preventing collapse failure. Several collapse failure models are used in the petroleum industry, and among these are Drucker- Prager, Ewy, Stassi d'Alia, Mogi- Coulomb criteria and Mohr- Coulomb criteria.

Wellbore collapse occurs when the stress surrounding the rock, exceeds the strength. This type of compressive failure develops from failure at wellbore wall, failure inside the formation or as a time-dependent failure (Chen, et al., 2001). Each presented failure model for collapse has its advantages and downsides when applied. The key is to choose the most appropriate, and take precautions to the shortcomings of the model.

2.3.1.1 Mohr- Coulomb

The Mohr-Coulomb criterion is the most applied and straightforward failure criterion for rock materials. This criterion assumption that overburden stress, σ_v, has zero influence on the strength of the rocks. The Mohr- Coulomb failure criterion links the shearing resistance of the involved forces and friction, to the connecting bonds between the rock grains. The criterion is linearly approximated as (Aadnøy & Looyeh, 2011):

$$\boldsymbol{\tau = \tau_0 + \sigma \tan \varphi} \tag{2.47}$$

Where τ is the shear stress, τ_0 is the cohesive strength, σ is the effective normal stress and φ is the angle or internal friction. Figure 2.21 illustrates the Mohr- Coulomb failure envelope.
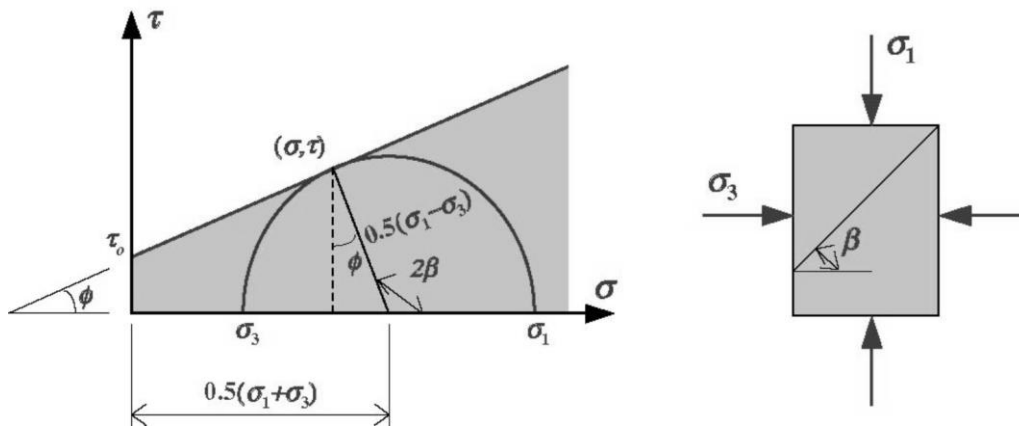
FIGURE 2.21: MOHR-COULOMB FAILURE ENVELOPE WHERE THE CIRCLES IN THE ENVELOPE, EACH REPRESENTS A TRIAXIAL TEST (AADNØY & LOOYEH, 2011)

Mohr-Coulomb:

$$\boldsymbol{\sigma_{1,2} = \frac{\sigma_\theta + \sigma_z}{2} \pm \sqrt{\left(\frac{\sigma_\theta - \sigma_z}{2}\right)^2 + \sigma_{\theta z}^2}} \tag{2.48}$$

$$\boldsymbol{r = \sqrt{\left(\frac{\sigma_\theta - \sigma_z}{2}\right)^2 + \sigma_{\theta z}^2}} \tag{2.49}$$

$$\sigma_{min = Center - r}$$

$$\sigma_{max = Center + r}$$

Mohr-Coulomb principal stresses:

$$\{\sigma_r\} \tag{2.50}$$

$$\left\{ \frac{\sigma_\theta + \sigma_z}{2} + \sqrt{\left(\frac{\sigma_\theta - \sigma_z}{2} \right)^2 + \sigma_{\theta z}^2} \right\} \tag{2.51}$$

$$\left\{ \frac{\sigma_\theta + \sigma_z}{2} - \sqrt{\left(\frac{\sigma_\theta - \sigma_z}{2} \right)^2 + \sigma_{\theta z}^2} \right\} \tag{2.52}$$

When analyzing rock failure, an expression for the particular stress state should be established. If the effective stress is assumed to be represented as in Figure 2.21, the failure point (σ, τ) may be expressed as the following:

$$\tau = \frac{1}{2}(\sigma_1 - \sigma_3) \cos \varphi \tag{2.53}$$

$$\sigma = \frac{1}{2}(\sigma_1 + \sigma_3) - \frac{1}{2}(\sigma_1 - \sigma_3) \sin \varphi \tag{2.54}$$

The fracture angle of the rock specimen β_{MC}, and the angle of internal friction φ obtained from the Mohr-Coulomb model, are related to one another by the following relation (Aadnøy & Looyeh, 2011):

$$\beta_{MC} = 45° + \frac{\varphi}{2} \tag{2.55}$$

It should be noted that the above equations (2.53 and 2.54) do not consider the intermediate principal stress, which results in an underestimation of the rock strength. Hence, the presented collapse pressure curve will be too conservative (Al-Ajmi & Zimmermann, 2006). Several assumptions must also be made in order to apply the equations for well collapse by the Mohr-Coulomb model. The shear stress in the Kirsch's equations may be neglected. The normal and shear stresses are estimated from the borehole wall, which gives us $a = r$. The angle θ is assumed equal to $\pi/2$ in order to provide the maximum values of the stresses. Inserting these values in the equations 2.15- 2.20 section 2.1.3, the stress components reduces to the following:

$$\sigma_r = P_w - P_0 \tag{2.56}$$

$$\sigma_\theta = 3\sigma_x - \sigma_y - P_w - P_0 \tag{2.57}$$

$$\sigma_z = \sigma_{zz} + 2v(\sigma_x - \sigma_y) - P_0 \tag{2.58}$$

$$\tau_{r\theta} = \tau_{rz} = 0 \tag{2.59}$$

$$\tau_{\theta z} = -2\tau_{xz} \tag{2.60}$$

Consequently, the stresses are in terms of in-situ stresses, and the principal stresses may be calculated by inserting these equations in equations 2.28-2.30. If the well is assumed vertical, the principal stresses are given as the following (Fjær, et al., 2008):

$$\sigma_r = P_w \tag{2.61}$$

$$\sigma_\theta = 2\sigma_h - P_w \tag{2.62}$$

$$\sigma_z = \sigma_v \tag{2.63}$$

Hence, the equations above show that pressure variations will affect the radial and hoop stress, while the axial stress will not be changed. When collapse failure occurs, the hoop stress exceeds the radial stress. This occurs at three scenarios (Al-Ajmi & Zimmermann, 2006):

$$\sigma_\theta > \sigma_r > \sigma_z \tag{2.64}$$

$$\sigma_z > \sigma_\theta > \sigma_r \tag{2.65}$$

$$\sigma_\theta > \sigma_z > \sigma_r \tag{2.66}$$

These scenarios may be implemented with the values for maximum and minimum principal stresses in the given Mohr-Coulomb failure criterion model to derive equations for well collapse pressure. The equations are derived as following for the different cases in parentheses (Fjær, et al., 2008):

Case	Equation	Number
$\sigma_\theta \geq \sigma_z > \sigma_r$	$P_w \leq P_0 + \dfrac{2(\sigma_h - P_0) - C_0}{1 - \tan^2 \beta_{MC}}$	(2.67)
$\sigma_z \geq \sigma_\theta > \sigma_r$	$P_w \leq P_0 + \dfrac{\sigma_v - P_0 - C_0}{\tan^2 \beta_{MC}}$	(2.68)
$\sigma_z \geq \sigma_r > \sigma_\theta$	$P_w \geq P_0 + 2(\sigma_h - P_0) - \dfrac{\sigma_v - P_0 - C_0}{\tan^2 \beta_{MC}}$	(2.69)
$\sigma_r \geq \sigma_z > \sigma_\theta$	$P_w \geq P_0 + \dfrac{2(\sigma_h - P_0)\tan^2 \beta_{MC} + C_0}{\tan^2 \beta_{MC}}$	(2.70)
$\sigma_r \geq \sigma_\theta > \sigma_z$	$P_w \geq P_0 + (\sigma_v - P_0)\tan^2 \beta_{MC} + C_0$	(2.71)
$\sigma_\theta \geq \sigma_r > \sigma_z$	$P_w \leq P_0 + 2(\sigma_h - P_0) - (\sigma_v - P_0)\tan^2 \beta_{MC} - C_0$	(2.72)

2.3.1.2 Drucker-Prager

The Drucker-Prager failure criterion is an extended variant of the Von-Mises criterion. The criterion assumes that the octahedral shearing approaches the critical value when (Yu, et al., 2002):

$$\alpha_{DP} I_1 + \sqrt{J_2} - \beta_{DP} = 0 \tag{2.73}$$

Where α_{DP} and β_{DP} are associated with the internal friction angle φ and the cohesive strength τ_0 for linear conditions. For evaluating a given rock formation failure, the second deviatoric invariant ($\sqrt{J_2}$) must be plotted against the first invariant, the mean effective stress (I_1) (Yu, et al., 2002).

$$\sqrt{J_2} = \alpha_{DP} I_1 + \beta_{DP} \tag{2.74}$$

$$I_1 = \frac{\sigma_{rr} + \sigma_{\theta\theta} + \sigma_{zz}}{3} - p(r,t) \tag{2.75}$$

$$J_2 = \frac{1}{6}((\sigma_{rr} - \sigma_{\theta\theta})^2 + (\sigma_{\theta\theta} - \sigma_{zz})^2 + (\sigma_{rr} - \sigma_{zz})^2) + \sigma_{r\theta}{}^2 + \sigma_{\theta z}{}^2 + \sigma_{rz}{}^2 \tag{2.76}$$

The constants α and β are estimated by using Young's Modulus and Poisson's ratio as follows (Yu, et al., 2002):

$$\beta_{DP} = \frac{2\sqrt{2}c\,\cos\varphi}{3-\sin\varphi} \tag{2.77}$$

$$\alpha_{DP} = \frac{2\sqrt{2}\,\sin\varphi}{3-\sin\varphi} \tag{2.78}$$

Where c is the cohesive strength and θ is the friction angle.

A potential failure occurs when the effective collapse stress, σ_{cl} given at a specific point is less than zero (Yu, et al., 2002):

$$\sigma_{cl} = -\sqrt{J_2} + \alpha_{DP}I_1 + \beta_{DP} \leq 0 \tag{2.79}$$

Hence, collapse failure happens when the rock strength exceeds the rock stress, or in this case, when the failure index σ_{cl}, becomes negative. This criterion fits higher stress levels.

2.3.1.3 Ewy-Modified Lade

The Lade failure criterion is developed for cohesion material. The model reads (Ewy, 1998):

$$\left(\frac{I_1^3}{I_3} - 27\right)\left(\frac{I_1}{P_a}\right)^{m_{Ewy}} - \eta_{Ewy,1} = 0 \tag{2.80}$$

I_1 and I_3 are the first and the second invariant stresses tensors, m_{Ewy} and $\eta_{Ewy,1}$ are material constants and P_a is the atmospheric pressure. In addition:

$$I_1 = \sigma_1 + \sigma_3 + \sigma_3 \tag{2.81}$$

$$I_3 = \sigma_1\sigma_2\sigma_3 \tag{2.82}$$

2.3.1.3.1 Modified Version

The modification is on the first and the second invariant stresses tensors. These are given as (Ewy, 1998):

$$I_1 = (\sigma_1 + S_{Ewy} - P_0) + (\sigma_2 + S_{Ewy} - P_0) + (\sigma_3 + S_{Ewy} - P_0) \tag{2.83}$$

$$I_3 = (\sigma_1 + S_{Ewy} - P_0)(\sigma_2 + S_{Ewy} - P_0)(\sigma_3 + S_{Ewy} - P_0) \tag{2.84}$$

The material constants S_{Ewy} and η_{Ewy} relate to the Coulomb strength parameters by:

$$S_{Ewy} = \frac{c}{\tan \phi}$$

(2.85)

$$\eta_{Ewy} = 4\tan^2 \phi \frac{(9 - 7\sin \phi)}{(1 - \sin \phi)}$$

(2.86)

2.3.1.4 Mogi- Coulomb

The Mogi-Coulomb failure criterion is considered an extended version of the Mohr-Coulomb criterion. It was introduced by Al-Ajmi and Zimmermann (Al-Ajmi & Zimmermann, 2006), who reviewed several rock failure models on data from numbers of rock types. Their conclusion was that the Mohr-Coulomb criterion underestimated the rock strength, while the Drucker-Prager criterion overestimated it. By considering the importance of the intermediate principal stress associated with failure, and accounting for the cohesion strength and the friction angle, they stated that applying this model would give best practice. The formulation of the criterion is given as following (Al-Ajmi & Zimmermann, 2006):

$$\tau_{oct} = k_{MgC} + m_{MgC}\sigma_{oct}$$

(2.87)

Where τ_{oct} and σ_{oct} are the octahedral shear and normal stresses expressed as (Al-Ajmi & Zimmermann, 2006):

$$\tau_{oct} = \frac{1}{3}\sqrt{(\sigma_1 - \sigma_2)^2 + (\sigma_1 - \sigma_3)^2 + (\sigma_2 - \sigma_3)^2} = \sqrt{\frac{2}{3}J_2}$$

(2.88)

$$\sigma_{oct} = \frac{1}{3}(\sigma_1 + \sigma_2 + \sigma_3)$$

(2.89)

In this relation, k_{MgC} and m_{MgC} are rock material constants and these may be evaluated from the intercept and the slope of the resulting failure envelope when plotting τ_{oct} versus σ_{oct}. The Figure 2.22 illustrates the example of the best fits from a fictional triaxial and polyaxial test.
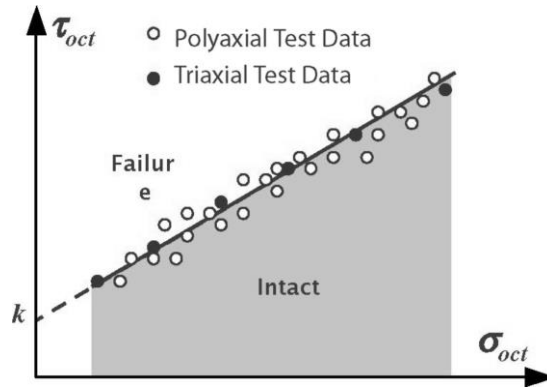
FIGURE 2.22: MOGI-COULOMB FAILURE ENVELOPE (AL-AJMI & ZIMMERMANN, 2006)

2.3.1.5 Stassi D'Alia

Stassi d'Alia is a simple linear elastic failure criterion model used to estimate shear failure. The model has been commonly used by Statoil ASA as it has proven to provide reliable data for many years. The failure criterion is presented as follows (Stjern, et al., 2003):

$$(\sigma_1 - \sigma_2)^2 + (\sigma_2 - \sigma_3)^2 + (\sigma_3 - \sigma_1)^2 = 2(C_0 - \tau_0)(\sigma_1 + \sigma_2 + \sigma_3 + 2C_0\tau_0) \qquad (2.90)$$

The tensile strength, τ_0, is often set equal to zero, to prevent sudden unwanted effects occurring when the tensile strength is increased.

When $\tau_0 = 0$:

$$(\sigma_1 - \sigma_3)^2 + (\sigma_2 - \sigma_3)^2 + (\sigma_3 - \sigma_1)^2 = 2C_0(\sigma_1 + \sigma_2 + \sigma_3) \qquad (2.91)$$

One disadvantage of the model is that it seems to overestimate the importance of the intermediate principal stress, σ_2, resulting in misleading collapse predictions. However, to improve the source of error, the criterion might be calibrated against collapse problems in two comparable wells (Stjern, et al., 2003).

2.3.2 Fracture Model

Tensile failure of a material occurs when the tensile strength is exceeded by the minimum compressive effective principal stress, σ_{min}^{ef}, resulting in a non-negative breakdown failure index σ_{bd}. The ultimate tensile strength is the limit where the tensile stress may lead to tensile failure.

2.3.2.1 Rankine Failure Criteria

Unlike for collapse failure modeling, one failure criterion for tensile failure modeling is used. The failure criterion according to Rankine is given as (Fjær, et al., 2008):

$$\boldsymbol{\sigma_3 = -\sigma_T} \tag{2.92}$$

Where σ_3 is the effective minimum principal stress and σ_T is the tensile strength of the rock. This type of failure may be ductile, which yields at the first stage, hardens at the second stage and breaks after a possible "neck" formation. When brittle failure occurs, the formation may suddenly break into two or several pieces at low stress state. Naturally, formed cracks or fractures make rocks weak and the tensile strength for rocks is negligible.

3 Well Collapse Modeling

This chapter presents the well collapse modeling derived for this thesis. The well collapse models are based on the Stassi d'Alia and the Mohr-Coulomb failure criteria. The models will be used in the case studies of the Heidrun and Norne well programs.

3.1 Well Collapse Modeling Based on Stassi D'Alia Failure Criteria

This well collapse model is based on the Stassi d'Alia failure criterion. The derived model considers driving forces such as temperature and chemical effects. This is an improved borehole stability model, routinely used by Statoil ASA (Stjern, et al., 2003).

The Stassi d'Alia failure criterion:

$$(\sigma_1 - \sigma_2)^2 + (\sigma_2 - \sigma_3)^2 + (\sigma_3 - \sigma_1)^2 = 2(C_0 - \tau_0)(\sigma_1 + \sigma_2 + \sigma_3 + 2C_0\tau_0) \qquad (2.90)$$

Assume that the tensile strength is equal to zero, ($\tau_0 = 0$), to avoid unexpected effects that commonly occur if the tensile strength is increased.

$$(\sigma_1 - \sigma_3)^2 + (\sigma_2 - \sigma_3)^2 + (\sigma_3 - \sigma_1)^2 = 2C_0(\sigma_1 + \sigma_2 + \sigma_3) \qquad (2.91)$$

The stresses are as following:

$$\sigma_1 = \sigma_\theta = 3\sigma_x - \sigma_y + 2\eta(P_w - P_\pi - P_0) + k_S - P_w \qquad (3.1)$$

$$\sigma_2 = \sigma_z = \sigma_v + k_S + 2\eta(P_w - P_\pi - P_0) \qquad (3.2)$$

$$\sigma_3 = P_w \qquad (3.3)$$

Where:

$$k_S = \frac{E\alpha_m}{3(1-v)}(T_w - T_o) \qquad (3.4)$$

$$\eta_S = \frac{\alpha_o(1-2v)}{1-v} \qquad (3.5)$$

Inserting the stresses into the failure criteria:

$$\sigma_1 - \sigma_2 = 3\sigma_x - \sigma_y + 2\eta_S(P_w - P_\pi - P_0) + k_S - P_w - \sigma_v - 2\eta_S(P_w - P_\pi - P_0) - k_S \qquad (3.6)$$

$$\sigma_1 - \sigma_2 = 3\sigma_x - \sigma_y - P_w - \sigma_v = C_{12} - P_w \qquad (3.7)$$

$$\sigma_2 - \sigma_3 = \sigma_v + k_S + 2\eta_S(P_w - P_\pi - P_0) - P_w \qquad (3.8)$$

$$\sigma_v + k_S - 2\eta_S(P_\pi + P_0) - (1 - 2\eta_S)P_w = C_{23} - \alpha_S P_w \qquad (3.9)$$

$$\sigma_3 - \sigma_1 = 3\sigma_x - \sigma_y + 2\eta_S(P_w - P_\pi - P_0) + k_S - 2P_w = C_{13} - \beta_S P_w \qquad (3.10)$$

$$\sigma_1 + \sigma_2 + \sigma_3 = 3\sigma_x - \sigma_y + 4\eta_S(P_w - P_\pi - P_0) + 2k_S + \sigma_v = C_{123} - \omega_S P_w \qquad (3.11)$$

Finally:

$$(C_{12} - P_w)^2 + (C_{23} - \alpha_S P_w)^2 + (C_{13} - \beta_S P_w)^2 = 2C_0(C_{123} - \omega_S P_w) \qquad (3.12)$$

$$P_w^2 - 2C_{12}P_w + C_{12}^2 + \alpha_S^2 P_w^2 - 2\alpha_S C_{23}P_w + C_{23}^2 + \beta_S^2 P_w^2 - 2C_{13}\beta_S P_w + C_{13}^2 = 2C_0 C_{123} + 2C_0\omega_S P_w) \qquad (3.13)$$

$$P_w^2(1 + \alpha_S^2 + \beta_S^2) - 2(C_{12} + C_{23} + C_{13} + C_0\omega_S)P_w + C_{12}^2 + C_{23}^2 + C_{13}^2 - 2C_0 C_{123} = 0 \qquad (3.14)$$

Applying the second-degree formula:

$$aP_w^2 + bP_w + c = 0 \qquad (3.15)$$

Where:

$$a = 1 + \alpha_S^2 + \beta_S^2 = 1 + (1 - 2\eta_S)^2 + 4(1 - \eta_S)^2 \qquad (3.16)$$

$$\beta_S = 2\eta_S - 2 = -(2 - 2\eta_S) \qquad (3.17)$$

$$b = -2(C_{12} + C_{23} + C_{13}) \qquad (3.18)$$

$$\omega_S = 4\eta_S \qquad (3.19)$$

$$C_{12} = 3\sigma_x - \sigma_y + k_S - \sigma_v \qquad (3.20)$$

$$C_{23} = \sigma_v + k_S - 2\eta_S(P_\pi + P_0) \qquad (3.21)$$

$$C_{13} = 3\sigma_x - \sigma_y - 2\eta_S(P_\pi + P_0) + k \qquad (3.22)$$

$$C_{123} = 3\sigma_x + 4\eta_S(P_w - P_\pi - P_0) + 2k_S + \sigma_v \tag{3.23}$$

$$c = C_{12}^2 + C_{23}^2 + C_{13}^2 - 2C_0C_{123} + 3P_0^{New} \tag{3.24}$$

So:

$$P_{Stassi\,d'Alia} = \frac{-b \pm \sqrt{b^2 - 4ac}}{2a} \tag{3.25}$$

3.2 Well Collapse Modeling Based on the Mohr-Coulomb Failure Criterion

Abdullah Tariq (Tariq, 2014) presented an analysis of the Mohr-Coulomb model where the result demonstrated that the model is very sensitive to thermal and chemical effects. The model demonstrated that the well got stronger when $a_{df} > a_{fw}$. However, in this thesis, a new model was derived, based on other states of Mohr-Coulomb. The approach is as it was presented in section 2.3.1.1 for the case $\sigma_z \geq \sigma_\theta > \sigma_r$ (Fjær, et al., 2008):

$$P_w \leq P_0 + \frac{\sigma_v - P_0 - C_0}{\tan^2 \beta_{MC}} \tag{3.26}$$

The stresses at the wellbore are:

$$\sigma_{zz} = \sigma_z + 2\nu(\sigma_x - \sigma_y) + k_{MC} + 2\eta_{MC}(P_w - P_\pi - P_0) \tag{3.27}$$

$$\sigma_r = P_w - P_0 \tag{3.28}$$

Inserting into Mohr-Coulomb failure criterion (equation 3.26), one can solve the collapse pressure:

$$P_{cp} = \frac{\sigma_z + 2\nu(\sigma_x - \sigma_y) + k_{MC} - C_0 + \alpha_{MC}P_0 \tan^2 \beta_{MC} - 2\eta(P_\pi - P_0)}{\tan^2 \beta_{MC} - 2\eta_{MC}} \tag{3.29}$$

In the absence of thermal, poroelastic and chemical effect:

$$P_{cp} = \frac{\sigma_z + 2\nu(\sigma_x - \sigma_y) - C_0 + \alpha_{MC}P_0 (1 - \tan^2 \beta_{MC})}{\tan^2 \beta_{MC}} \tag{3.30}$$

3.3 Transient State Modeling

As sonic logs are not available for the modeling in this thesis, back calculations for compressional wave velocity using Gardner's relation (equation 2.2) was performed. Uniaxial compressive strength may be calculated using several models, but in this thesis the model derived by Horsrud (2001) (Horsrud, 2001) and Lal et al (1999) (Lal, 1999) is applied. By using sonic logs they could estimate the strength as following (Horsrud, 2001):

$$C_0[MPa] = 0,77 \left(\frac{304,8}{\Delta t_{(sonic)}}\right)^{2,93} \tag{3.31}$$

$$C_0 = 0,77 v_p^{2,93} \tag{3.32}$$

The transient effect is dependent on the uniaxial compressive strength (UCS). As the uniaxial compressive strength is a time dependent parameter, it may be expressed as following (Lal, 1999):

$$C(t) = (C_o - C_e)e^{at} + C_e \tag{3.33}$$

Where t is time in days, a is a constant and C_e is the equivalent cohesive strength. As time passes, the cohesive strength of any formation reduces to the equivalent cohesive strength. Figure 3.1 illustrates the uniaxial compressive strength (cohesive strength) as a function of time. For this simulation, the constant $a = -0,5$ and the equivalent cohesive strength, C_e was assumed to be 60% of the steady state uniaxial compressive strength, C_0. As can be seen, the strength reduces 66% after 10 days.
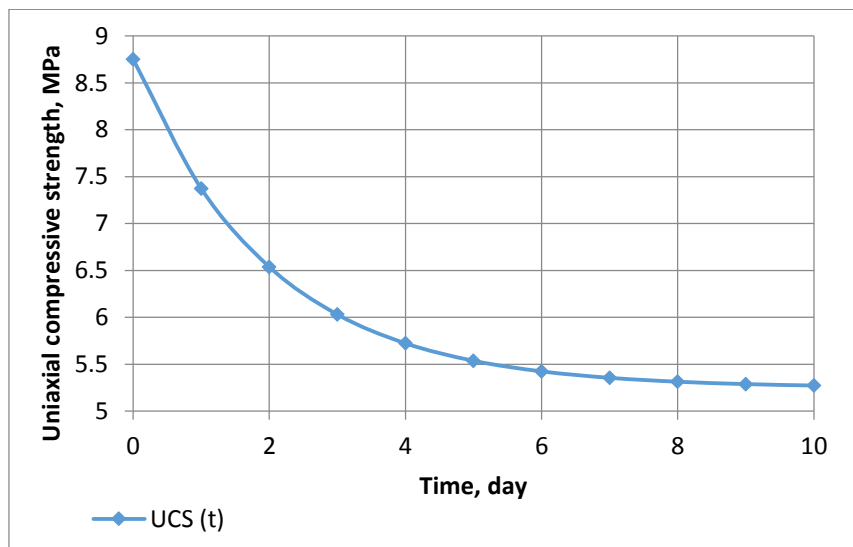

Figure 3.1: Cohesive Strength as a function of time (graph from Excel)

4 Simulation

As new stresses around the wellbore arises, and hence the collapse strength changes. A continuous control over the well pressures is required and ensuring that wellbore instability is maintained. By applying the given equations from chapter 2 and the derived models from chapter 3, new collapse pressures may be simulated. The primary objective of this simulation is to study the effect of changing various parameters. From the results, one will learn which parameters are the most sensitive therefore given the most caution.

This chapter presents simulation studies on the two Norwegian Continental shelf oil field well programs, namely Heidrun and Norne. The Heidrun field case study is simulated both with the Mohr-Coulomb model and the Stassi d'Alia model, and the Norne field is only simulated using the Stassi d'Alia model. Both fields are simulated under steady and transient state conditions. The following sensitivity studies were performed by using Excel spreadsheets. Data from the Heidrun well program (Figure 4.3) and Norne well program (Figure 4.29) was digitized and implemented in the models. The shale properties used for the analyses were based on the given values in

Table **2**.**1**. The simulation results presented below are for the most sensitive parameters of the well program, whereas less sensitive parameter effects are for the most sensitive presented in the appendix. To illustrate the effects, the percentage change is presented in both diagrams and numbers.[1]

4.1 Heidrun Field Simulation with Mohr-Coulomb Model

For the Heidrun case study, the analyses were performed, based on the Mohr-Coulomb model derived in section 3.2.

4.1.1 Heidrun Field

The Heidrun field is situated at the Haltenbanken outside Mid-Norway, as shown in Figure 4.1. The field was discovered in 1985 by Conoco, and has been producing oil and gas since 1995.

---

[1] Ref = reference, meaning steady state

The current operator of the field is Statoil with a company share of approximately 13,043160 % (NPD Facts Heidrun, 2015). The other partners are Petoro AS, ConocoPhillips Skandinavia AS and Eni Norge AS. A total of 76 wells have been planned on the main field, consisting of 51 production wells, 24 water injection wells and one gas injection well (NPD Facts Heidrun, 2015).

FIGURE 4.1: THE LOCATION OF THE HEIDRUN FIELD (ANON., 2009)

With a water depth of approximately 350 meters (NPD Facts Heidrun, 2015), the field is developed with a floating concrete TLP (Tension Leg Platform), installed over a subsea template. However, the northern part (The North Flank) is mainly developed with subsea facilities. Figure 4.2 shows an image of the platform above sea level.

FIGURE 4.2: THE HEIDRUN FIELD (NPD FACTS HEIDRUN, 2015)

The reservoir is a sandstone reservoir of the respective Garn, Ile, Tilje and Åre Formations of Early and Middle Jurrasic age. As the reservoir is very faulted, the reservoir quality varies, depending on the formation. The depth of the reservoir is about 2300 meters (NPD Facts Heidrun, 2015).To withhold and maintain a high pressure, water and gas is injected in the Garn and Ile Formation as they are good quality formations. As the Tilje and Åre Formations are more complex, water injection is the only recovery strategy in this part of the reservoir.

Considering the age of the field, several methods have been implemented to prolong the lifetime of the wells and improve the recovery. A few examples of these are: new drilling technology, new EOR (Enhanced Oil Recovery) methods, new well targets and Light Well Interventions.

The shale formations in the Heidrun field are namely Brygge, Tare and Tang which are of Lower-Tertiary age. These three formations are commonly known as the "troublesome BTT" (Brygge Tare Tang). Drilling these shales resulted in severe pack-off and lost circulation problems (Stjern, et al., 2003).

The wellbore program used in this thesis for the Heidrun simulations is a prognosis of a stability plot from a typical Heidrun TLP well (Stjern, et al., 2003). See figure 4.3. As Heidrun is located in an environmentally critical area, only water-based mud is accepted during drilling. However, KCl is utilized as an inhibitive additive in the mud.

The Heidrun TLP wells are generally drilled in three sections; the $17^{1/2}U$ section down into the Kai formation, the $12^{1/2}U$ section reaching top of the reservoir and the $81^{1/2}U$ section through the reservoir (Stjern, et al., 2003).
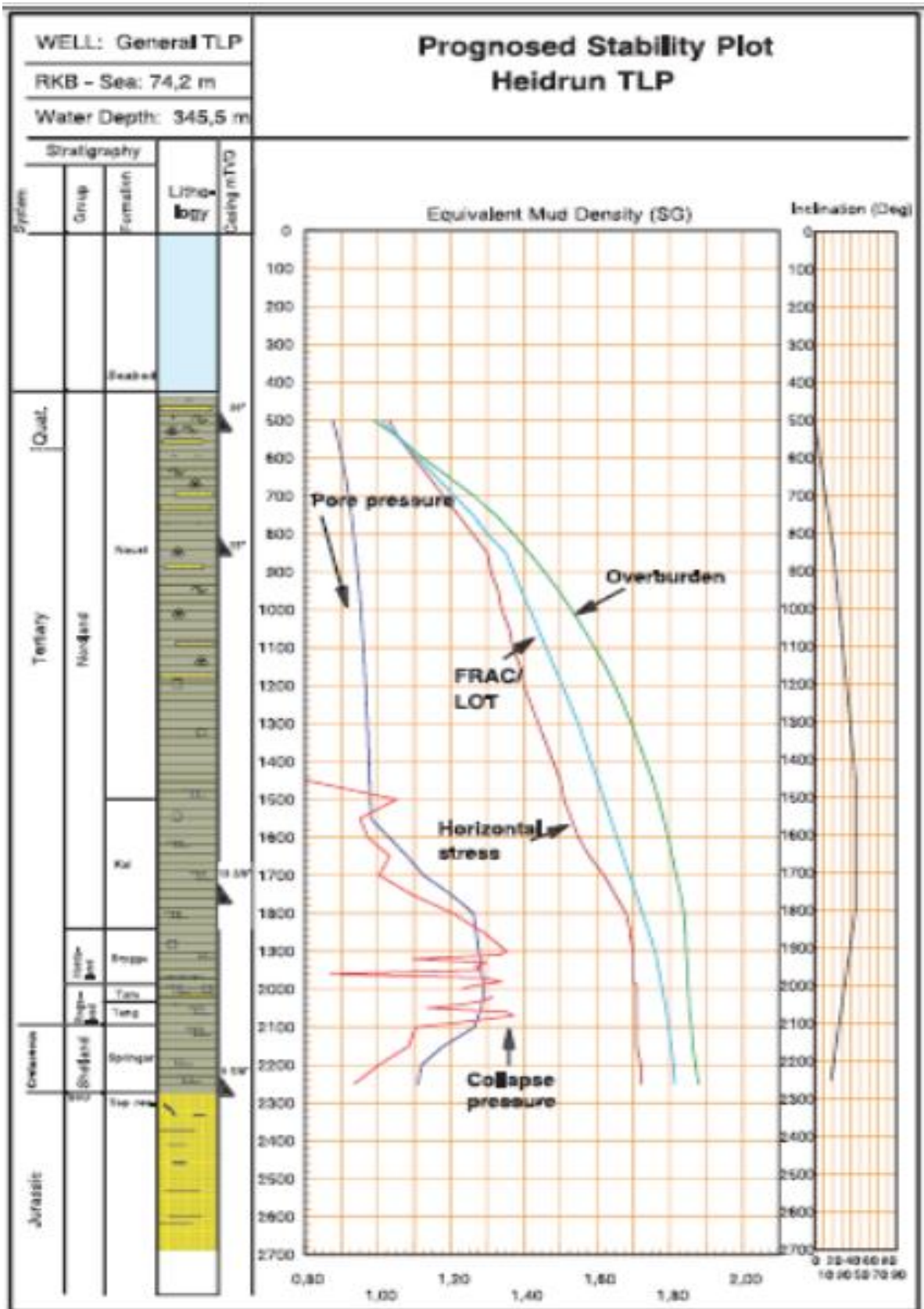
FIGURE 4.3: PROGNOSIS STABILITY PLOT FOR A TYPICAL HEIDRUN TLP WELL (STJERN, ET AL., 2003)

4.1.2   Steady State Parameter Sensitivity Studies

The exact changes (increase or decrease) are defined in the sections below. The sensitivity of two parameters is analyzed.

4.1.2.1   Effect of Poisson's Ratio

Poisson's ratio is an important parameter used to compute the horizontal stress, the thermal and poroelastic effect. This simulation will illustrate the effects of changing the value of Poisson's ratio from 0,22 to 0,25 and then to 0,27. Table 4.1 displays the simulation input parameters. The reference values are in the first column, with Poisson's ratio = 0,22.

TABLE 4.1: INPUT PARAMETERS

Parameters	Ref.	Input values	
Poisson's ratio, ν	0,22	0,25	0,27
Biot's coefficient, α_{Biot}	0,86	-	-
$\eta_{MC}=$	0,62	0,57	0,54
Internal friction angle, φ, deg	35	-	-
Failure angle, β_{MC}, deg	62,5	-	-

Figure 4.4 shows the simulation result. As seen from figure 4.5, when the Poisson's ratio increases by 3%, the collapse pressure increases by an average value of 0,8%.
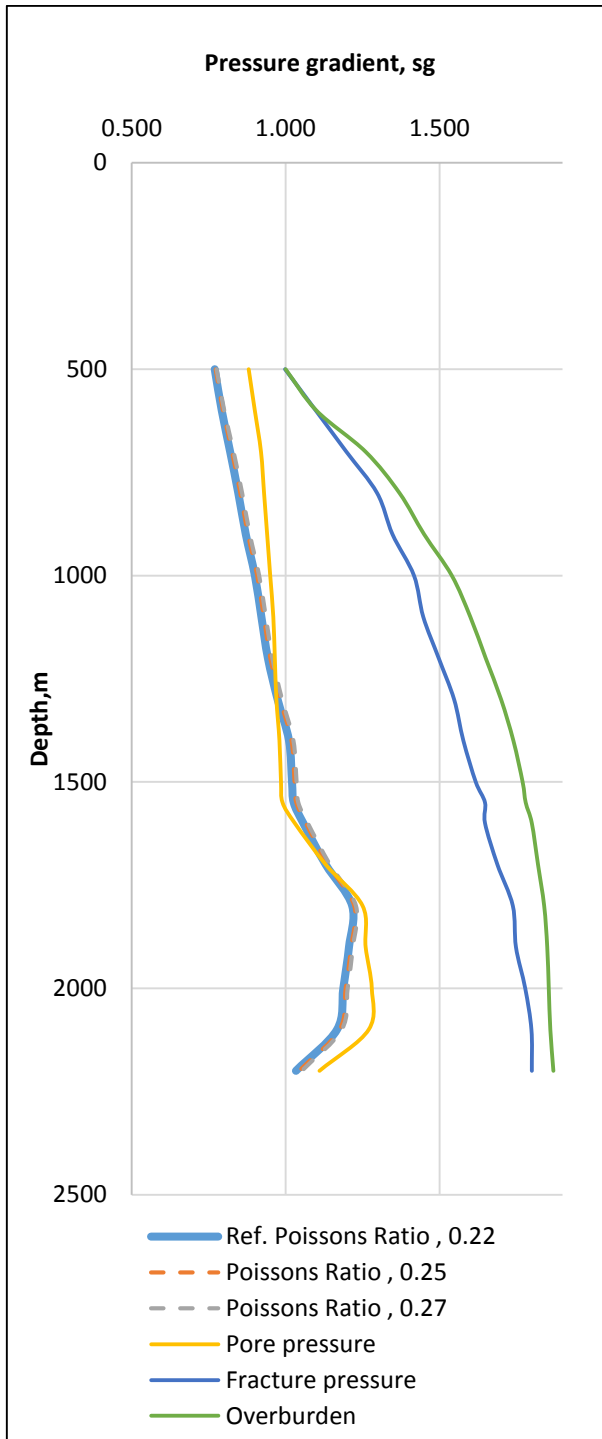
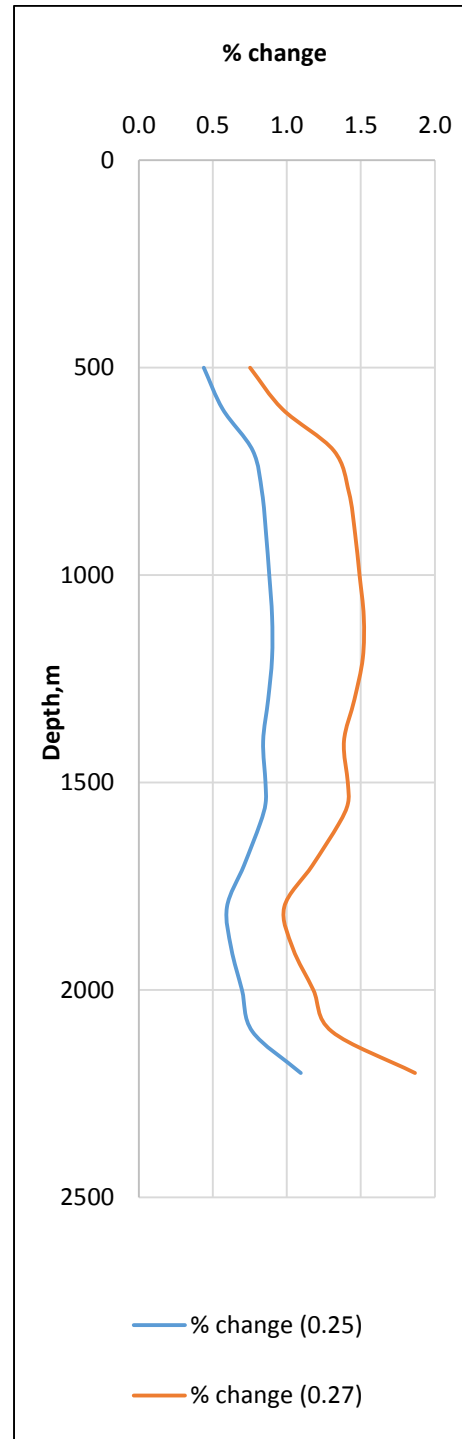FIGURE 4.4: PRESSURE RESULTS FOR CHANGES IN POISSON'S RATIO

FIGURE 4.5: PERCENTAGE CHANGE IN COLLAPSE PRESSURE

4.1.2.2 Effect of Biot's Coefficient

Table 4:2 displays the simulation input parameters. The reference values are in the first column, with Biot's coefficient = 0,86. This simulation will display the effects of changing the value of Biot's coefficient from 0,86 to 0,87 to 0,88 to 0,95. Figure 4.6 shows the simulation result. As seen from figure 4.7 when the Biot's coefficient increases by 1%, the collapse pressure increases by an average of 0,9%.

TABLE 4.2: INPUT PARAMETERS

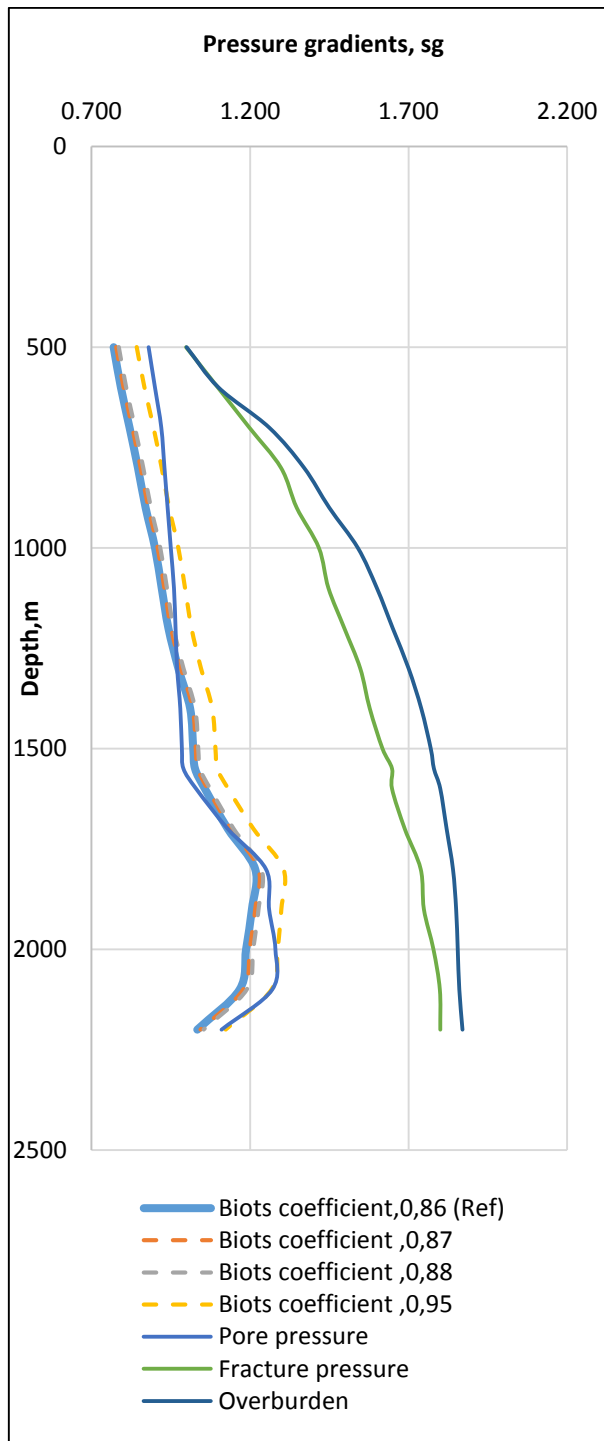| Parameters	Ref.	Input values		
Biot's coefficient, α_{Biot}	0,86	0,87	0,88	0,95
Poisson's ratio, ν	0,22	-	-	-
$\eta_{MC}=$	0,62	-	-	-
Internal friction angle, φ, deg	35	-	-	-
Failure angle, β_{MC}, deg	62,5	-	-	-

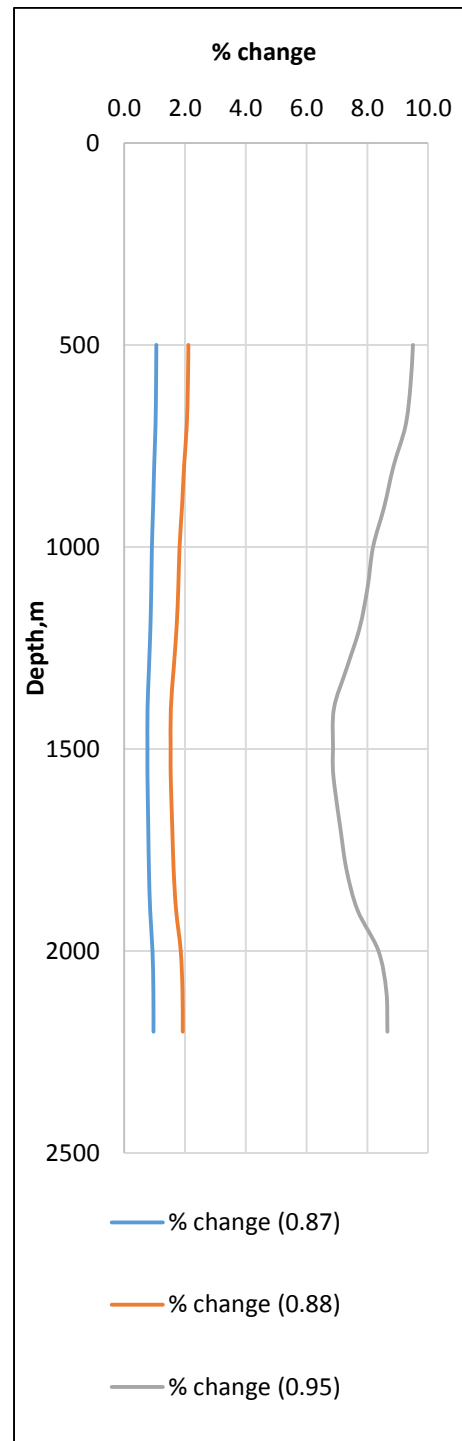FIGURE 4.6: PRESSURE RESULTS FOR CHANGES IN
BIOT'S COEFFICIENT

FIGURE 4.7: PERCENTAGE CHANGE IN
COLLAPSE PRESSURE

4.1.2.3 Effect of Activity

Table 4:3 display the simulation input parameters. The reference values are in the first column, and considered while there is no chemical effect activity ($a_{fw} = a_{df}$). The second column display the values for $a_{fw} = 0,91$ and $a_{df} = 0,80$ ($a_{fw} > a_{df}$), and the third column show the values for $a_{fw} = 0,91$ and $a_{df} = 0,95$ ($a_{fw} < a_{df}$). The value for the water activity in the shale does not vary as the activity of the formation water cannot be changed.

TABLE 4.3: INPUT PARAMETERS

Parameters	Ref.	Input values	
Activity, a	$a_{fw} = a_{df}$	$a_{df}=0,80$	$a_{df}=0,95$
Thermal conductivity, k_0	$8,633 \times 10^{-6}$	-	-
E-modulus	6895	-	-
Temperature, deg C	Tw	-	-
Internal friction angle, φ , deg	32	-	-
Biot's coefficient, α_{Biot}	0,86	-	-
Poisson's ratio, ν	0,22	-	-
$\eta_{MC}=$	0,62	-	-
Failure angle, β_{MC}, deg	61	-	-

Figure 4.8 shows the simulation result. As seen from figure 4.9, when water activity of the drilling fluid is 13,8% lower than the activity of the shale formation, the collapse pressure changes from a negative effect (minimum at -22,9%) to a positive effect (maximum at 17,6%), and then to a negative effect again (-2,8 % at the bottom of the well). When the water activity of the drilling fluid is 4,2% higher than the activity of the shale formation, the collapse pressure changes by 4,9% on the top of the well, by 28,6% at the maximum, and then it changes by 3,1% at the bottom of the well.
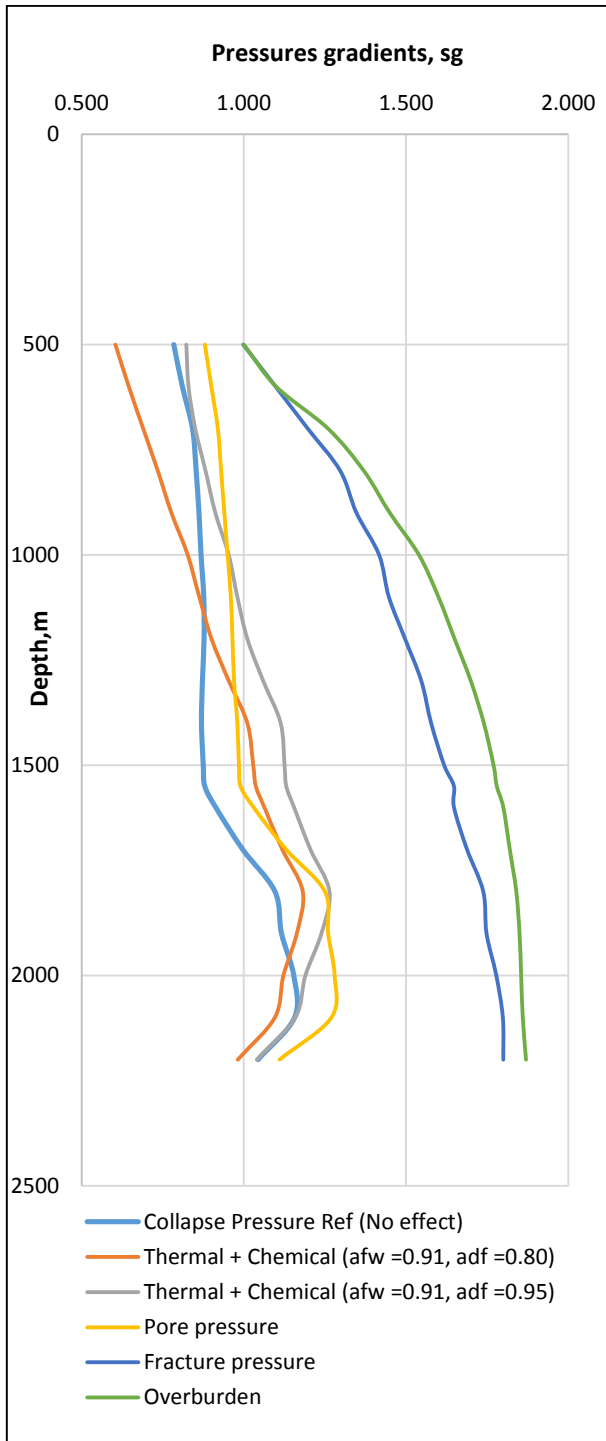
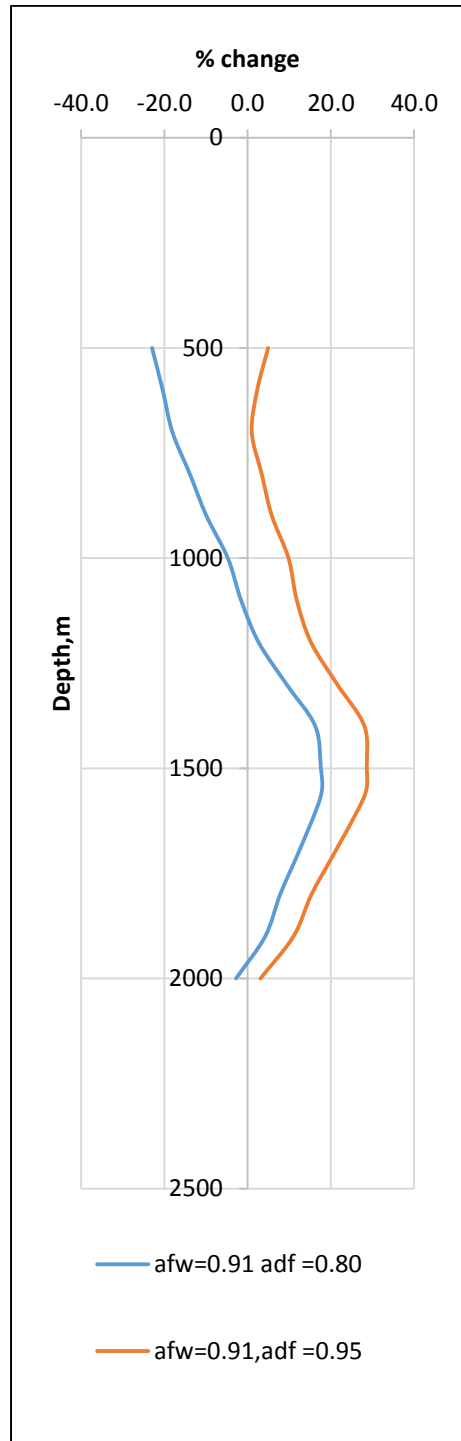FIGURE 4.8: PRESSURE RESULTS FOR CHANGES IN WATER ACTIVITY OF THE DRILLING FLUID

FIGURE 4.9: PERCENTAGE CHANGE IN COLLAPSE PRESSURE

4.1.3 Transient State Parameter Sensitivity Studies

In the above steady state well instability study, it was demonstrated that the combination of temperature and chemical effects influences the collapse strength. In this simulation, the transient effect is simulated based on in-situ stresses, thermal, chemical, and poroelastic driving forces.

4.1.3.1 Transient Effect on the Uniaxial Compressive Strength

Figure 4.10 shows the transient effect on the input parameter uniaxial compressive strength. The figure illustrates how the strength changes from the reference point (where only in-situ stresses are affecting) to after one day and ten days (during thermal and chemical effects). The figure displays that the UCS increases with time.
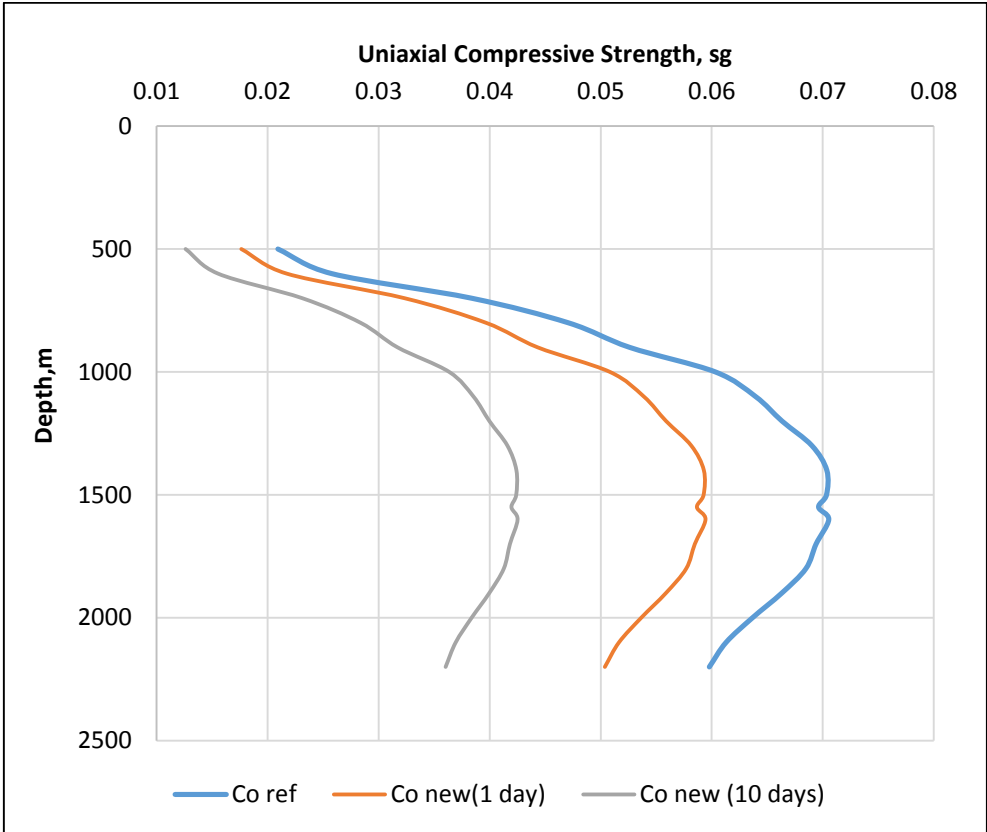

FIGURE 4.10: TRANSIENT EFFECT ON THE UCS

The uniaxial compressive strength decreases 15,7% after 1 day, and after 10 days it decreases 39,8% from its original value.

4.1.3.2 The Effect of Only In-Situ Stresses on the Collapse Pressure

Figure 4.11 displays the effect of only the in-situ stresses (without thermal and chemical effects). As seen, the change is not very visible from the first day to the tenth day. Figure 4.12 displays the percent change in the collapse pressure after one day and ten days when only in-situ stresses are acting. As seen, first the collapse pressure increases and changes with a maximum percentage of 21,2 % then after ten days (20,6% after one day) at 1500 meters. Afterwards it decreases again, and changes with a percentage of 1,2 % after ten days (0,8 % after one day) in the bottom of the well. Hence, the collapse pressure is most affected in the middle of the well, when only in-situ stresses are the acting force.
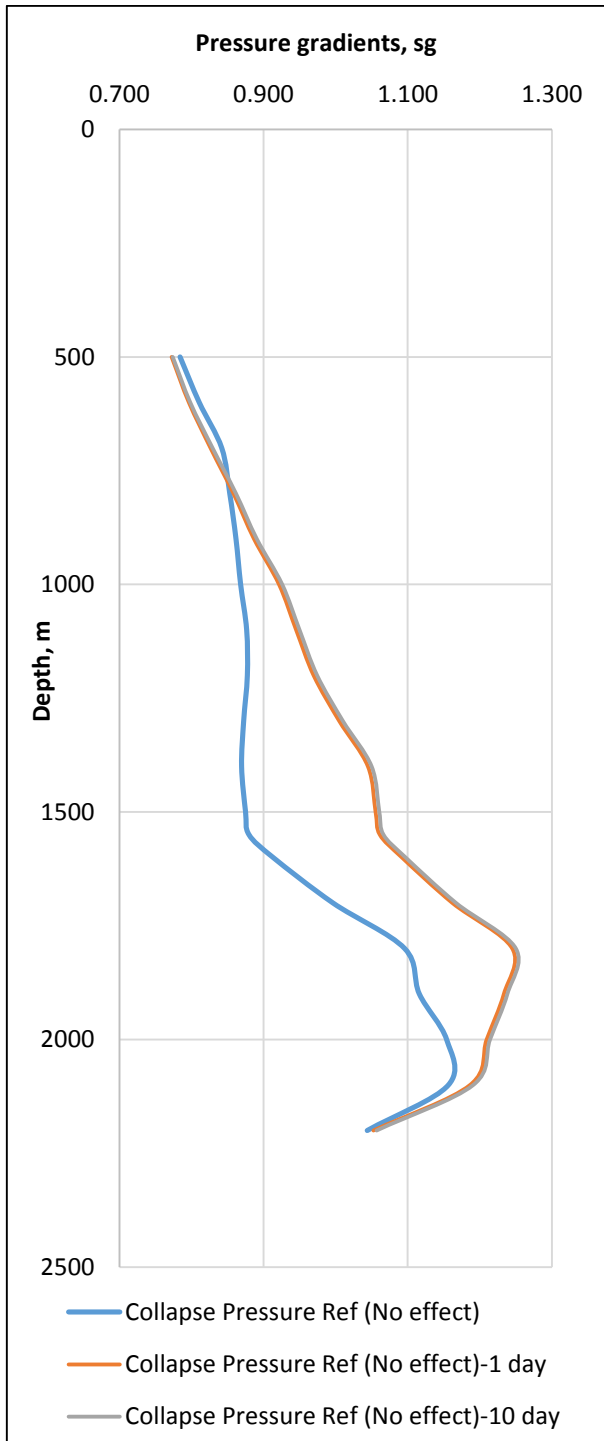
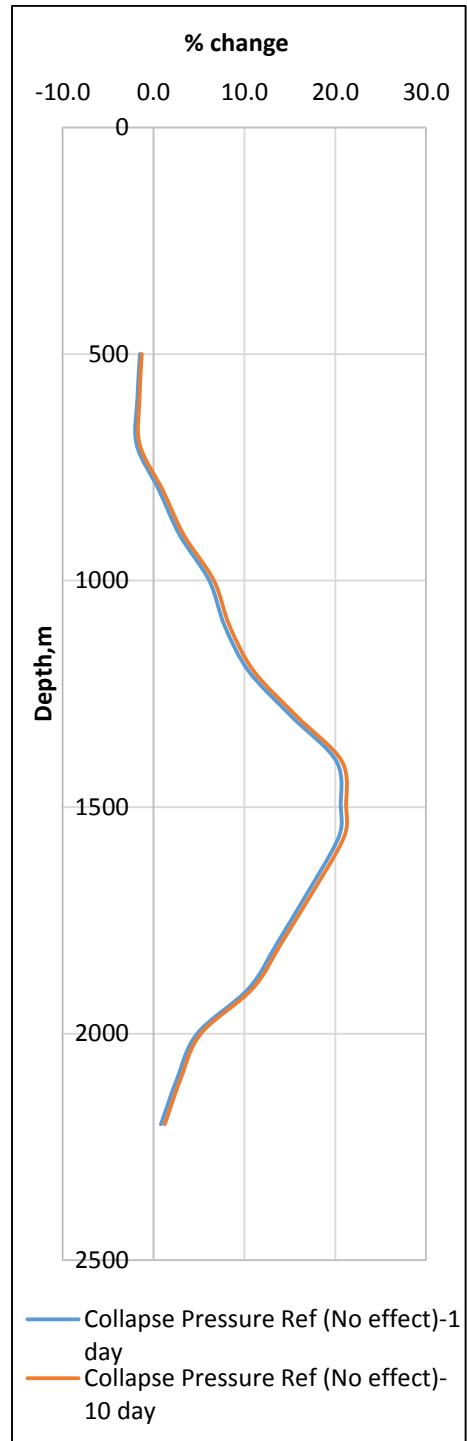FIGURE 4.11: EFFECT OF ONLY IN-SITU STRESSES

FIGURE 4.12: PERCENTAGE CHANGE OF THE COLLAPSE PRESSURE

4.1.3.3 Combined Effect after One Day

Figure 4.13 displays the total effect after one day. As seen, when the activity of the drilling fluid is higher than the activity of the formation water $(a_{df} > a_{fw})$, the collapse pressure increases. When the activity of the drilling fluid is lower than the activity of the formation water $(a_{df} < a_{fw})$, the collapse pressure decreases. It should be noted here, that if neither transient nor chemical and thermal effects are designed for, the well might collapse in some sections when $a_{df} < a_{fw}$. Figure 4.14 displays the percentage change in collapse pressure after one day. As seen, when $a_{df} < a_{fw}$, the change is first increasing (from -22,7% to 18,5% at the maximum), but then it decreases again (from 18,5% to -5,5%). When $a_{dr} > a_{fw}$, the change is first increasing (from -5,1% to 29,2% at the maximum), but then it decreases again (from 29,2% to -0,1%).
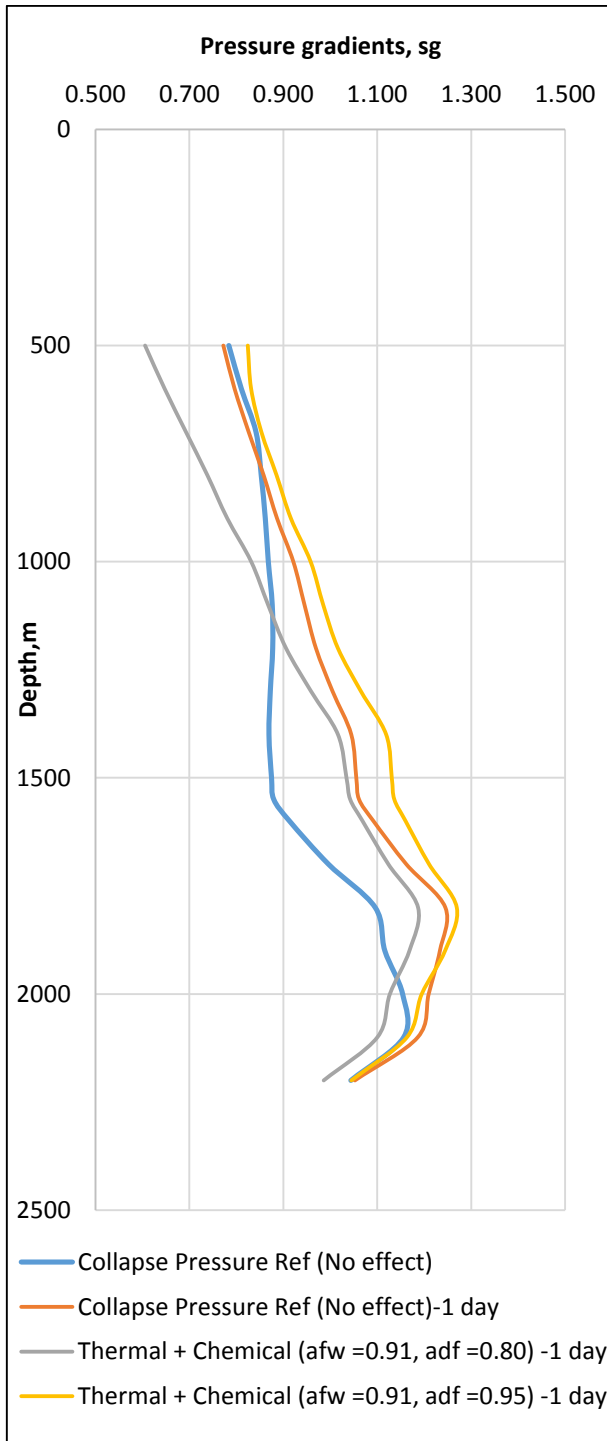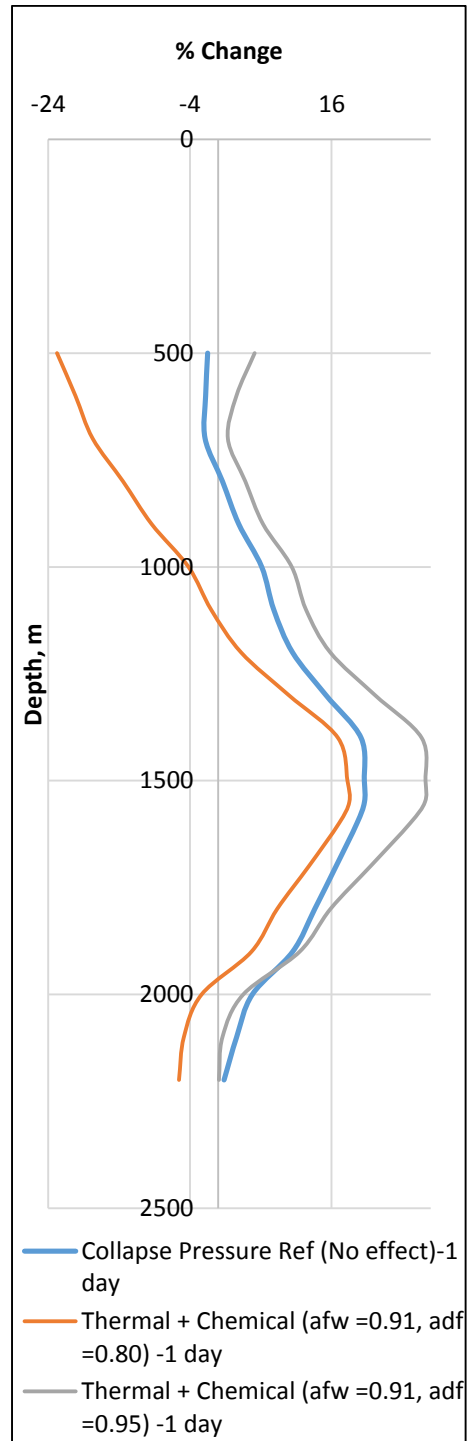
FIGURE 4.13: TOTAL EFFECT AFTER ONE DAY

FIGURE 4.14: PERCENTAGE CHANGE OF
THE COLLAPSE PRESSURE AFTER ONE
DAY

4.1.3.4 Combined Effect after Ten Days

Figure 4.15 displays the total effect after ten days. As seen, the curves are quite similar to the curves in figure 4.13 for one day. Hence, the collapse pressure changes in a similar way after ten days. Figure 4.16 displays the percentage change after ten days, with a basis of the reference point. This figure is also very similar to the figure for one day (Figure 4.14). As seen, when $a_{df} < a_{fw}$, the change is first increasing (from -22,4% to 19,4% at the maximum), but then it decreases again (from 19,4% to -4,9%). When $a_{df} > a_{fw}$, the change is first increasing (from 5,5% to 30,2% at the maximum), but then it decreases again (from 30,2% to 0,8%) to the bottom of the well.
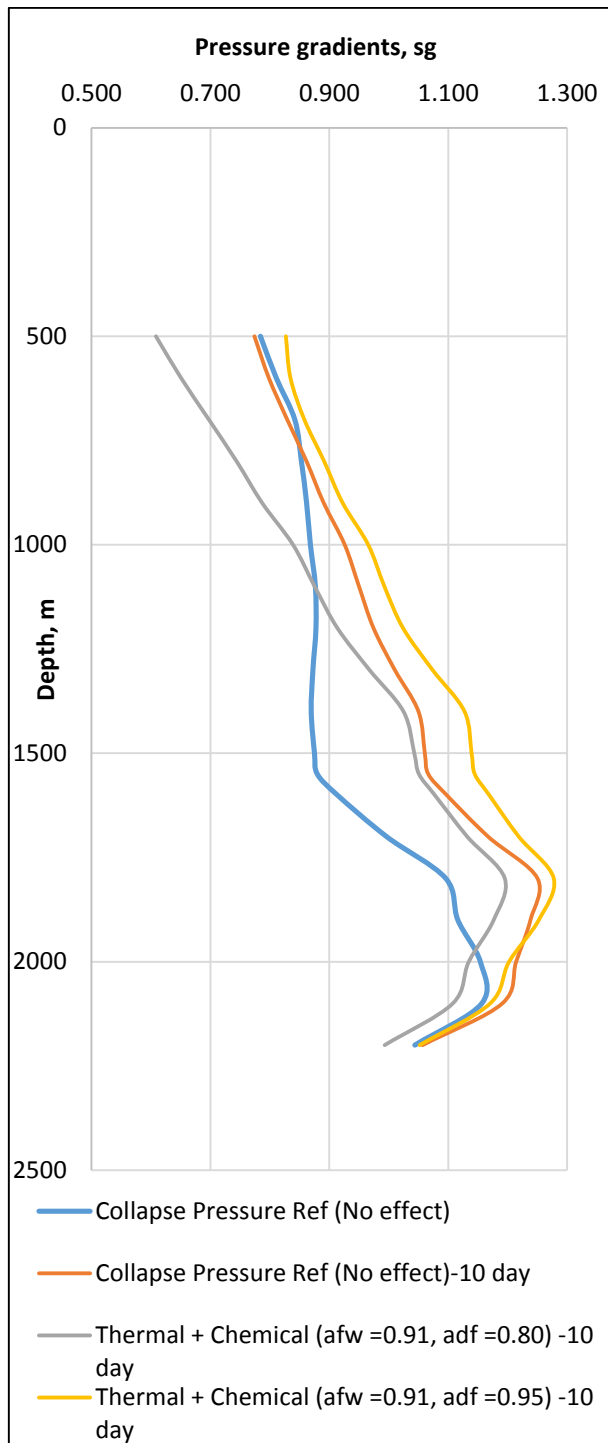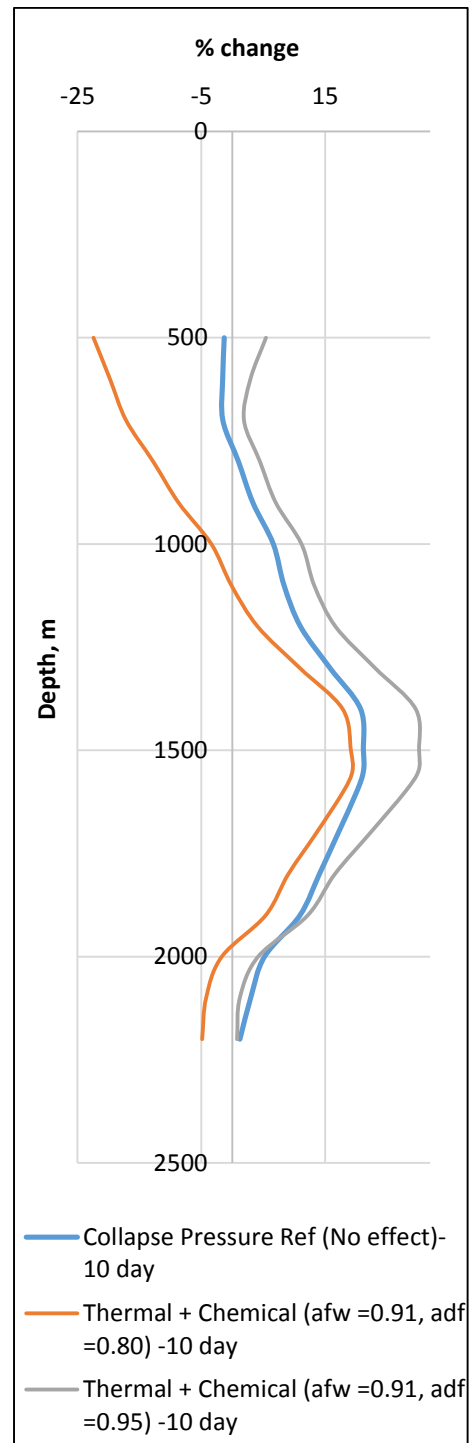
FIGURE 4.15: TOTAL EFFECT AFTER TEN DAYS

FIGURE 4.16: PERCENTAGE CHANGE IN COLLAPSE PRESSURE

4.1.3.5 Combined Effect from the First to the Tenth Day

The figures 4.17 and 4.18 considers the effect of only in-situ stresses (no thermal or chemical effects). Figure 4.17 displays the change of the collapse pressure when only in-situ stresses are affecting. The figure displays that there is not much of a change from the first to the tenth day as the curves are almost identical. Figure 4.18 displays the percentage change in the collapse pressure after the tenth day with the basis of the first day. As seen, the change is very low and ranges from 0,2-0,5%.
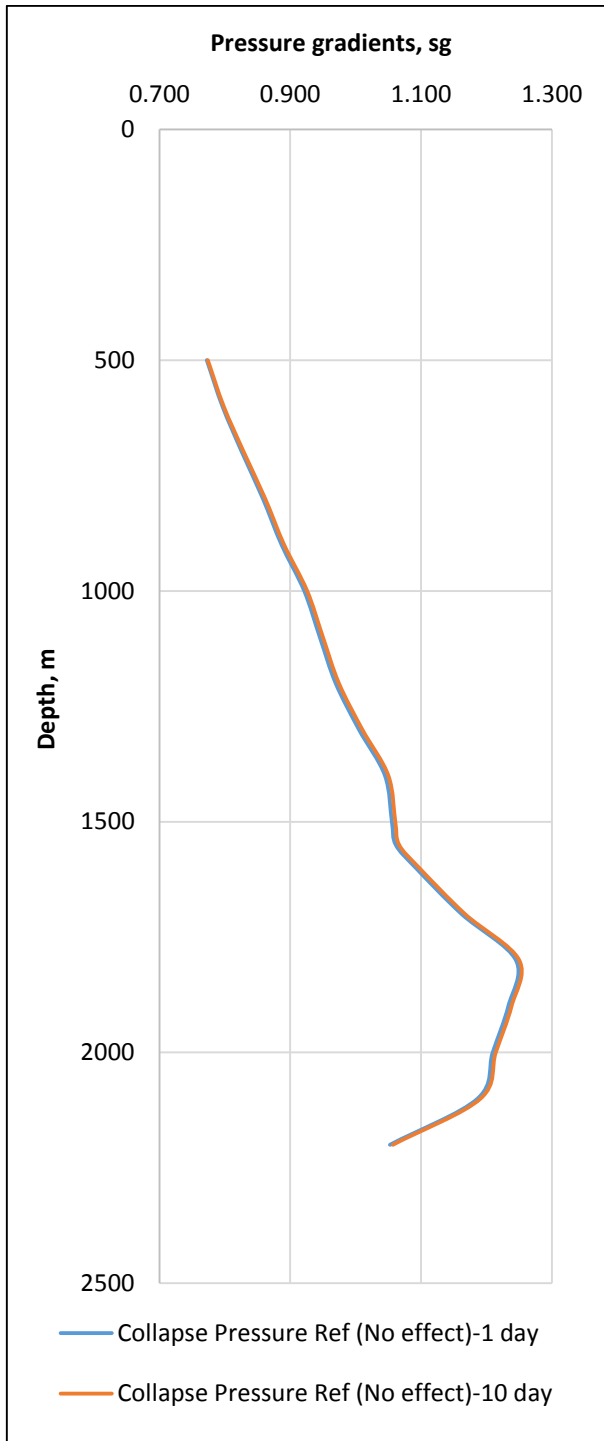
FIGURE 4.17: COLLAPSE PRESSURES FROM THE FIRST TO THE TENTH DAY WHEN ONLY IN-SITU STRESSES ARE ACTING
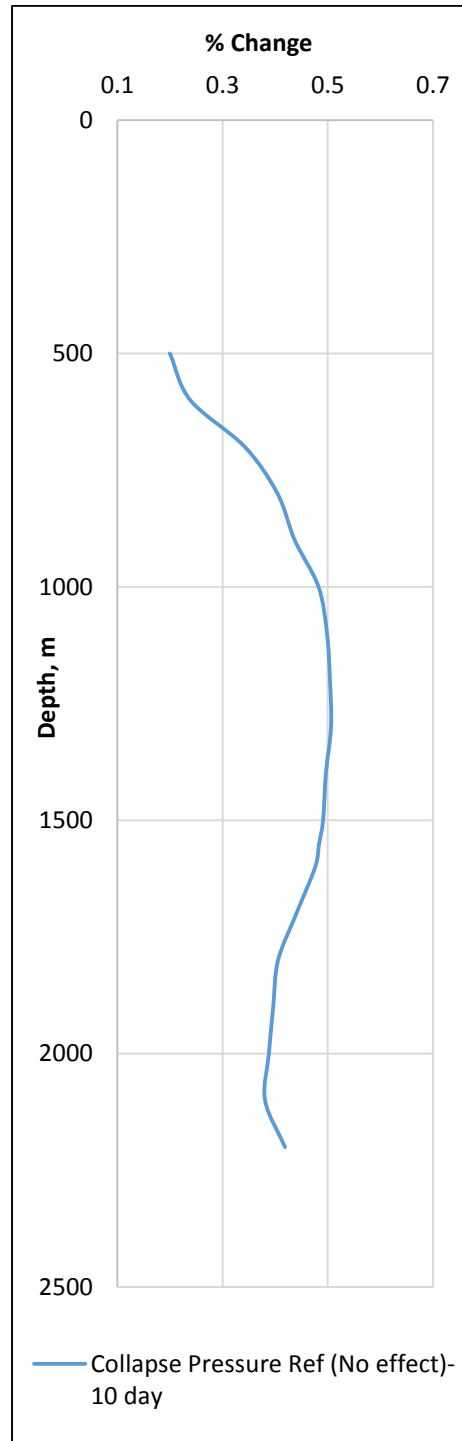
FIGURE 4.18: PERCENTAGE CHANGE IN COLLAPSE PRESSURE

Figure 4.19 and 4.20 considers the thermal and chemical effect on the collapse pressure from the first day to the tenth day. Figure 4.19 displays the change in thermal and chemical effect when $a_{df} > a_{fw}$ and when $a_{df} < a_{fw}$. As seen, the curves of the first day and the tenth day are almost identical. Figure 4.20 displays the percentage change of the thermal and chemical effect. As mentioned, the change is not very significant. As illustrated in figure 4.20, the change ranges from 0,4-0,9% when $a_{df} < a_{fw}$ and from 0,3-0,8% when $a_{df} > a_{fw}$.
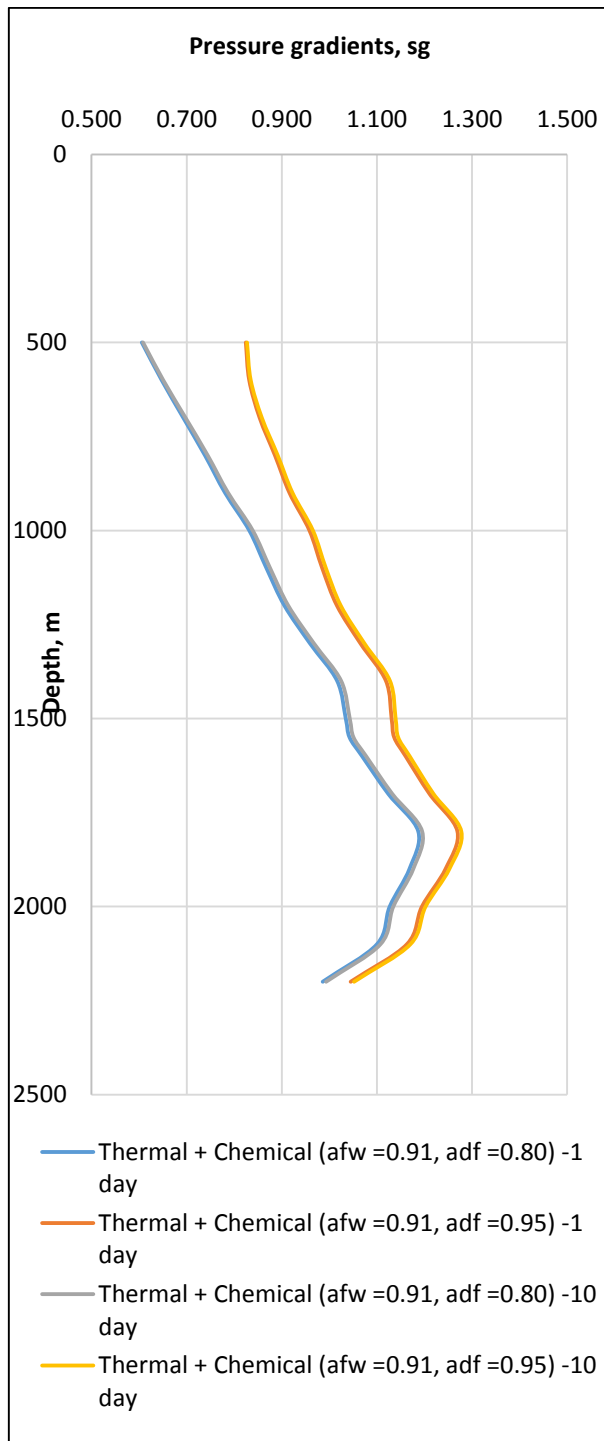
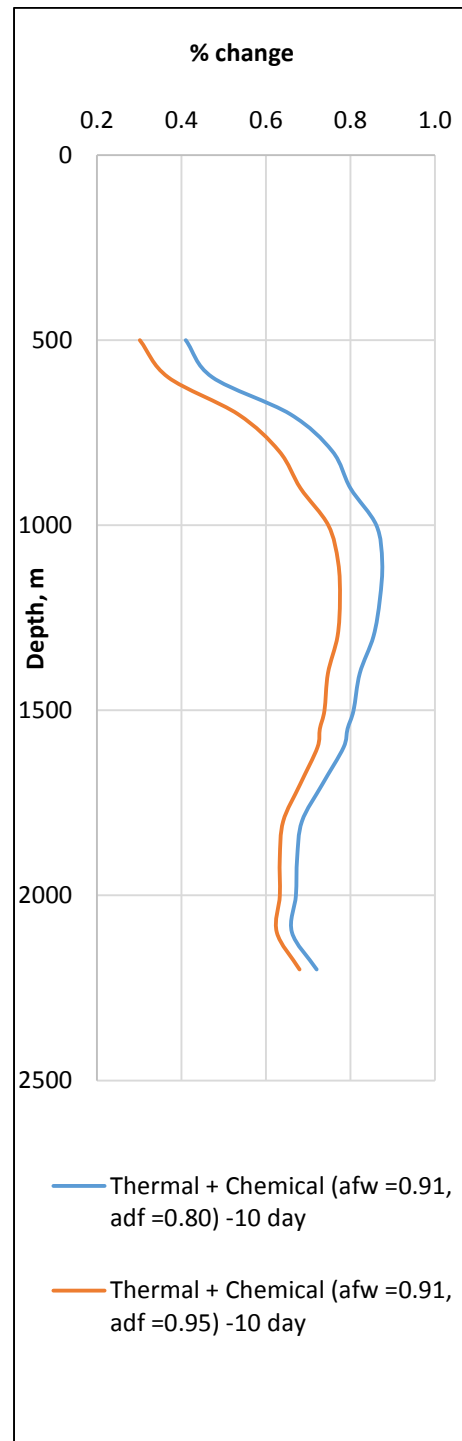FIGURE 4.19: THERMAL AND CHEMICAL EFFECT ON THE COLLAPSE PRESSURE AFTER ONE AND TEN DAYS

FIGURE 4.20: PERCENTAGE CHANGE OF THERMAL AND CHEMICAL EFFECT FROM THE FIRST TO THE TENTH DAY

4.2 Heidrun Field Simulation with Stassi D'Alia

The following simulation is based on the Stassi d'Alia failure criterion, modeled in section 3.1.

4.2.1   Steady State Chemical and Thermal Effects

In this section, only the effect of the activity of the drilling fluid is considered. Table 4.4 displays the input parameters. This simulation will illustrate the effects of changing the value of the drilling fluid activity from 0,8 to 0,91, while the shale formation water activity is held constant at 0,91. Figure 4. 21 illustrates the change of the collapse pressure due to thermal and chemical effects. As seen, from figure 4.22, the change ranges from -22,6% to -2,1% when $a_{df} < a_{fw}$, and from 0,9% to 13,2% when $a_{df} > a_{fw}$. Hence, the collapse pressure decreases when $a_{df} < a_{fw}$ and increases when $a_{df} > a_{fw}$. Figure 4.23 displays the wellbore pressures to the bottom of the well when thermal and chemical effects are influencing on the collapse pressure.

TABLE 4.4: INPUT PARAMETERS

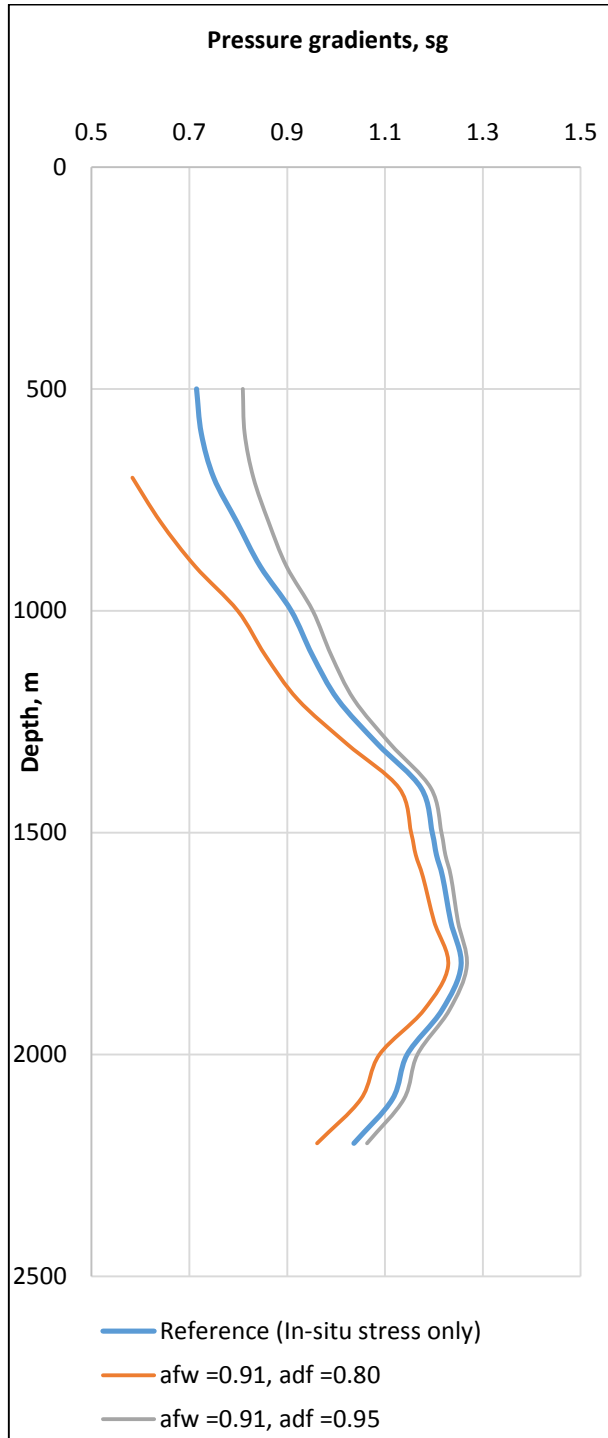| Parameters	Ref.	Input values
Activity of drilling fluid, a_{df}	0,8	0,95
Activity of formation water, a_{fw}	0,91	-
Poisson's ratio, ν	0,32	-
$\eta_S=$	0,502941	-
Biot's coefficient, α_{Biot}	0,95	-
Temperature Tw, deg C	350	-

FIGURE 4.21: THERMAL AND CHEMICAL EFFECTS DUE TO CHANGE IN DRILLING FLUID ACTIVITY
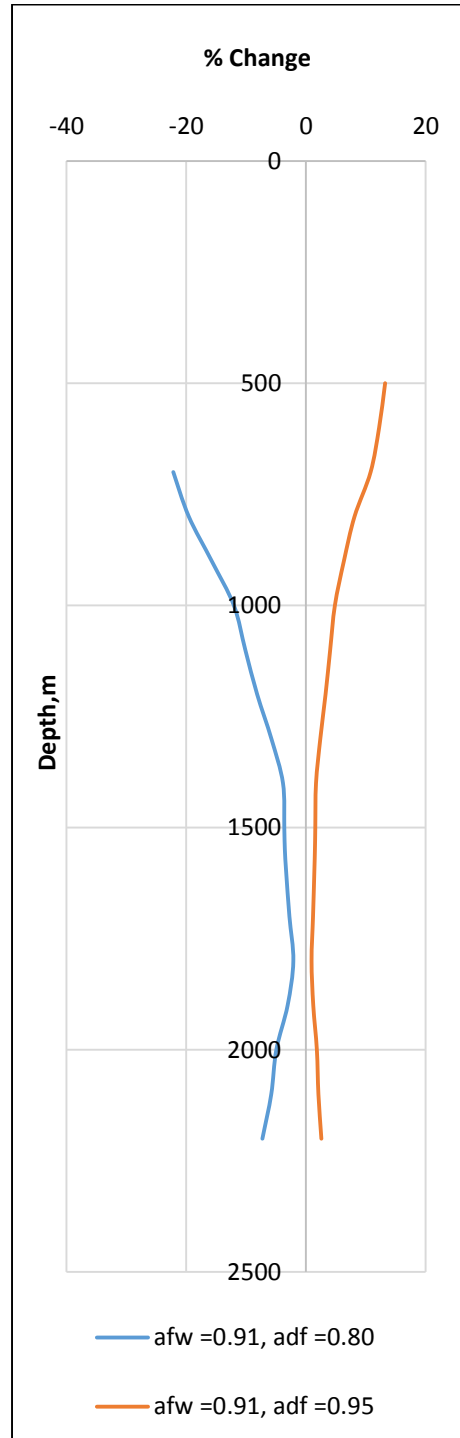

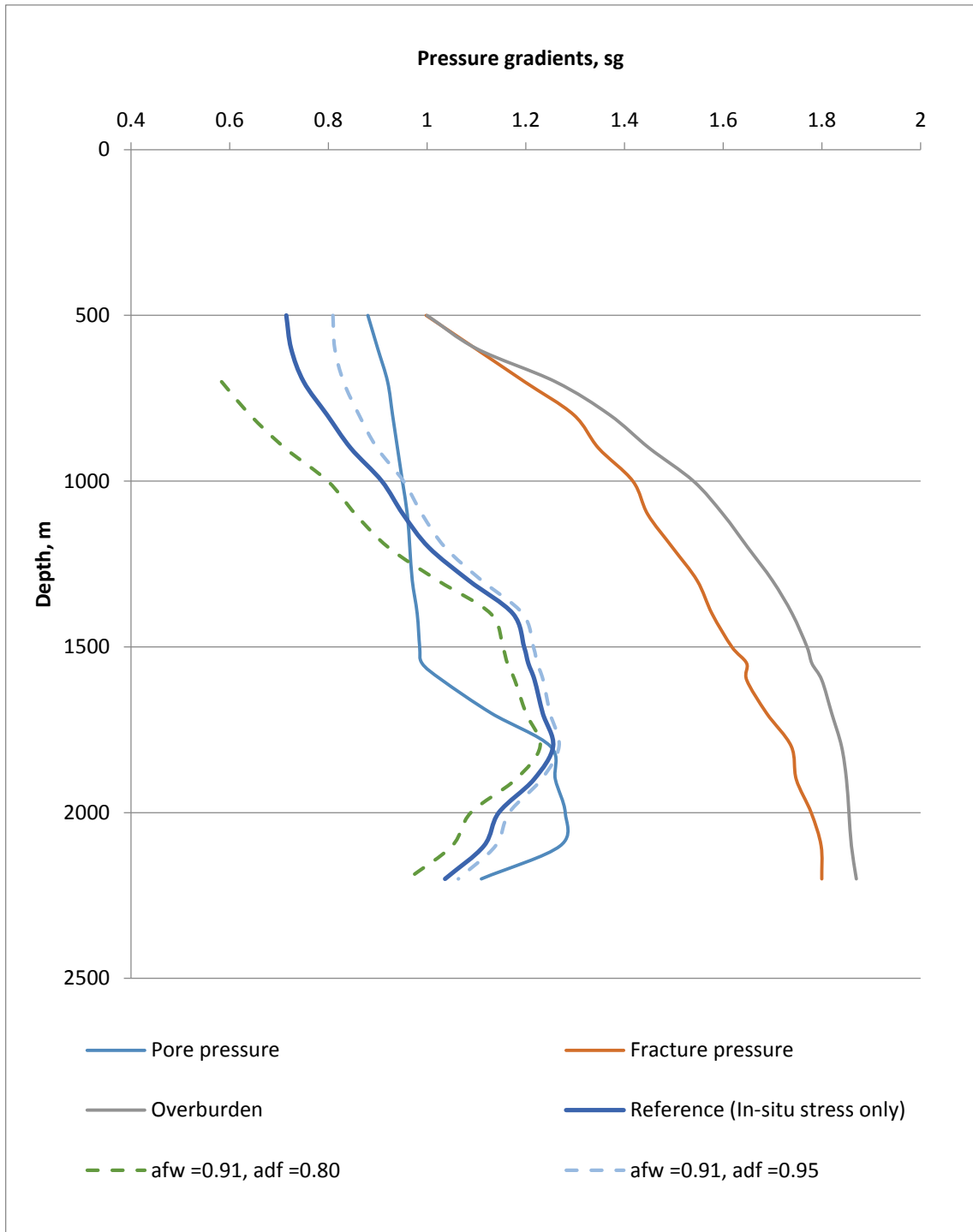FIGURE 4.22: PERCENTAGE CHANGE IN COLLAPSE PRESSURE

FIGURE 4.23: WELLBORE PRESSURES

4.2.2 Transient State Chemical and Thermal Effects

The transient effect is derived as in section 3.3. This section considers the combination of transient effect with thermal and chemical effect after one day. The input parameters are as defined in Table 4.4. Figure 4.24 displays how the pressures are affected by the thermal, chemical and transient effect. As illustrated in Figure 4.25, the change is most visible from 1000-1700 meters. At this interval, it shows a change of 1,41- 1,53% when $a_{df} < a_{fw}$ and 1,43-1,59% when $a_{df} > a_{fw}$. Figure 4.26 illustrates the changes in the collapse pressure due to the combination of the transient, thermal and chemical effects.

TABLE 4.5: INPUT PARAMETERS

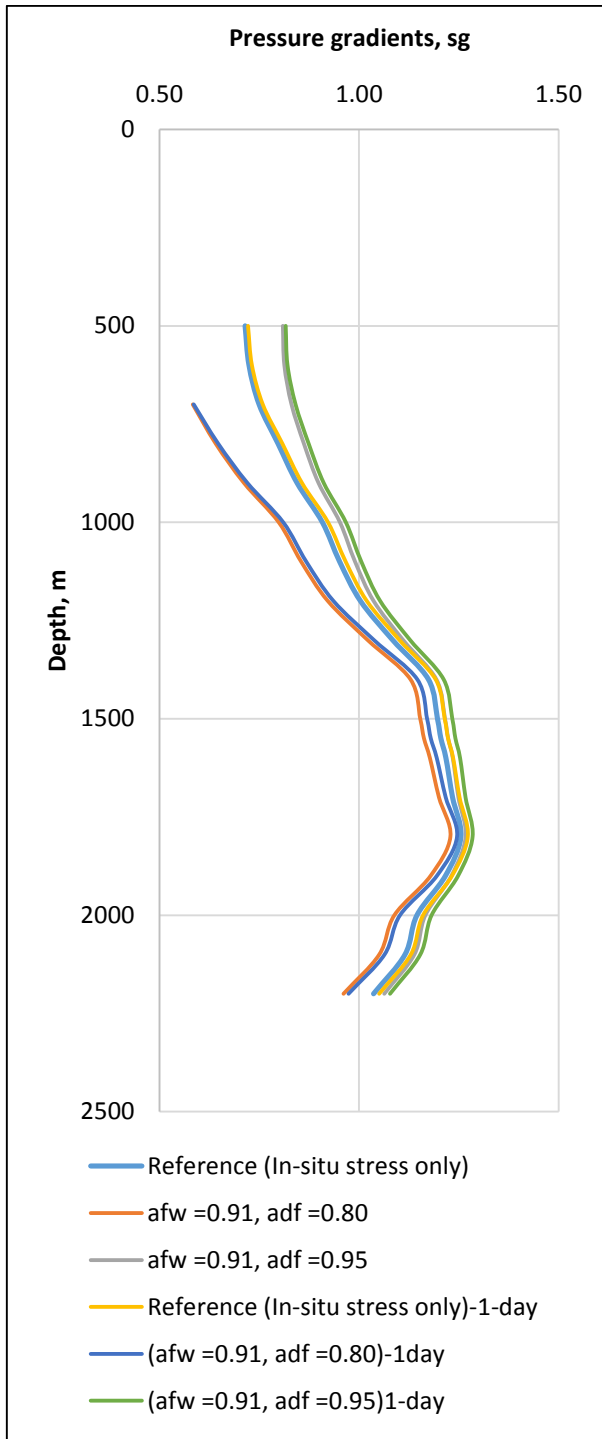| Parameters	Ref.	Input values
Activity of drilling fluid, a_{df}	0,8	0,95
Activity of formation water, a_{fw}	0,91	
Poisson's ratio, ν	0,32	-
$\eta_s =$	0,502941	-
Biot's coefficient, α_{Biot}	0,95	-
Temperature Tw, deg C	350	-

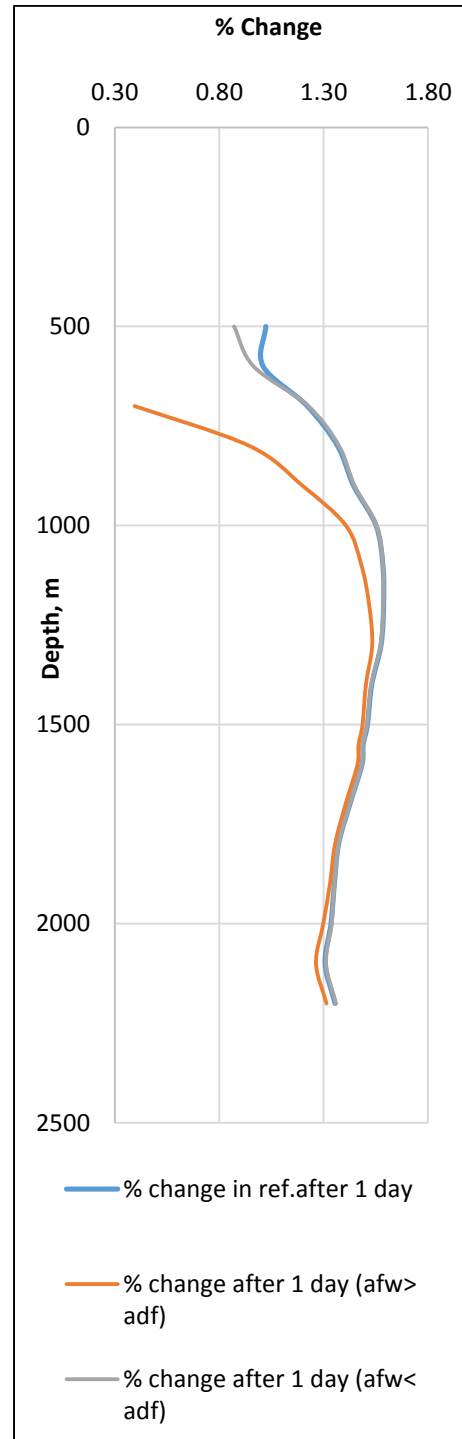FIGURE 4.24: CHANGES IN THE COLLAPSE PRESSURE
COMPARED TO REFERENCE POINT

FIGURE 4.25: PERCENTAGE CHANGE IN
COLLAPSE PRESSURE DUE TO TRANSIENT,
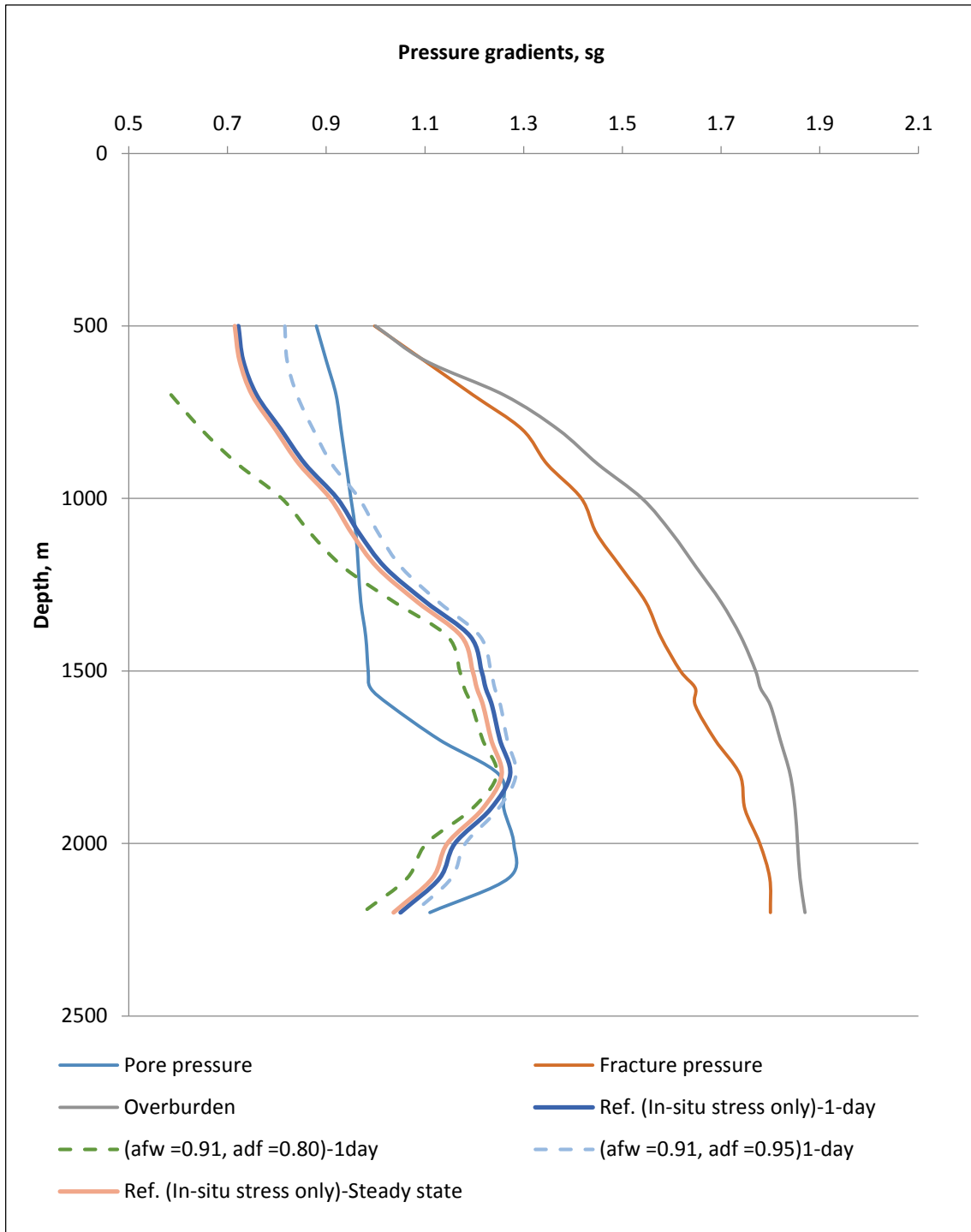CHEMICAL AND THERMAL EFFECTS

70

FIGURE 4.26: WELLBORE PRESSURES

4.3 Norne Field Simulation with Stassi D'Alia Model

The analyses for the Norne case study were based on the Stassi d'Alia model derived in section 3.1, using equation 3.25.

4.3.1   Norne Field

Norne is an oil field located approximately 80 km north of the Heidrun field in the Norwegian Sea, as seen in Figure 4.27. It was discovered in December 1991 and is located in the blocks 6608/10 and 6508/1 (NPD Facts Norne, 2015).The field was developed with a production and storage vessel, "Norne FPSO", connected to seven subsea templates, as seen in Figure 4.28 (NPD Facts Norne, 2015). A flexible riser to the vessel carries the well stream, which are anchored to the sea floor. A processing plant is located on the deck of the ship, while the vessel has storage tanks for stabilized oil.
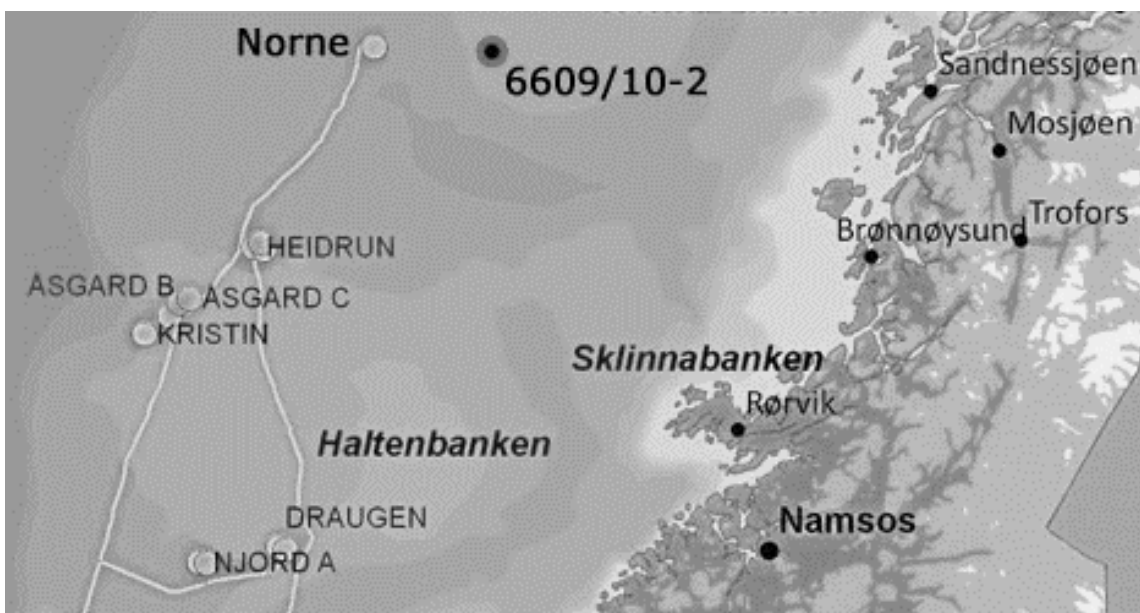

FIGURE 4.27: THE LOCATION OF THE NORNE FIELD (PTIL/PSA, U.D.)

FIGURE 4.28: NORNE FIELD (NPD, U.D.)

At the point of discovery, the estimated recoverable oil reserves were 450 million barrels. The water depth is approximately 380 meters. The reservoir is located at 2500 meters below the seabed and consists of sandstone of the Åre, Tilje, Tofte, Ile, Not and Garn formations. The field is operated from Harstad by Statoil ASA and its partners (Eni Norge AS and Petoro) (Adlam, 1995).

In August 1996, the development drilling commenced, while oil production began November 1997 (NPD Facts Norne, 2015). The oil is produced by water injection. Since the gas injection was stopped in 2005, all of the gas is now exported. The field consists of two oil compartments; the North-East Segment (Norne G-segment) and the Norne Main Structure (Norne C-,D- and E-segment) (NPD Facts Norne, 2015).

The given well program for this case study is 6608/10-K-2 H pilot (see Figure 4.29) (NPD Facts Norne, 2015). The reason for choosing exactly this field and well program is because there is shale all the way from the seabed down to the reservoir, which makes the simulation more precise. The well 6608/10-2 was originally the first wildcat well at the field. It was entered 28th of October 1991 and completed on January 29th 1992. The current status of the well is plugged and abandoned (NPD Facts Norne, 2015). However, the well from the given wellbore program, 6608/10-K-2, was drilled for observational purposes. By 2010 a total of 50 wells had been drilled in the field where 33 were producers, 10 water injectors and 7 were observation wells (NPD Facts Norne, 2015).
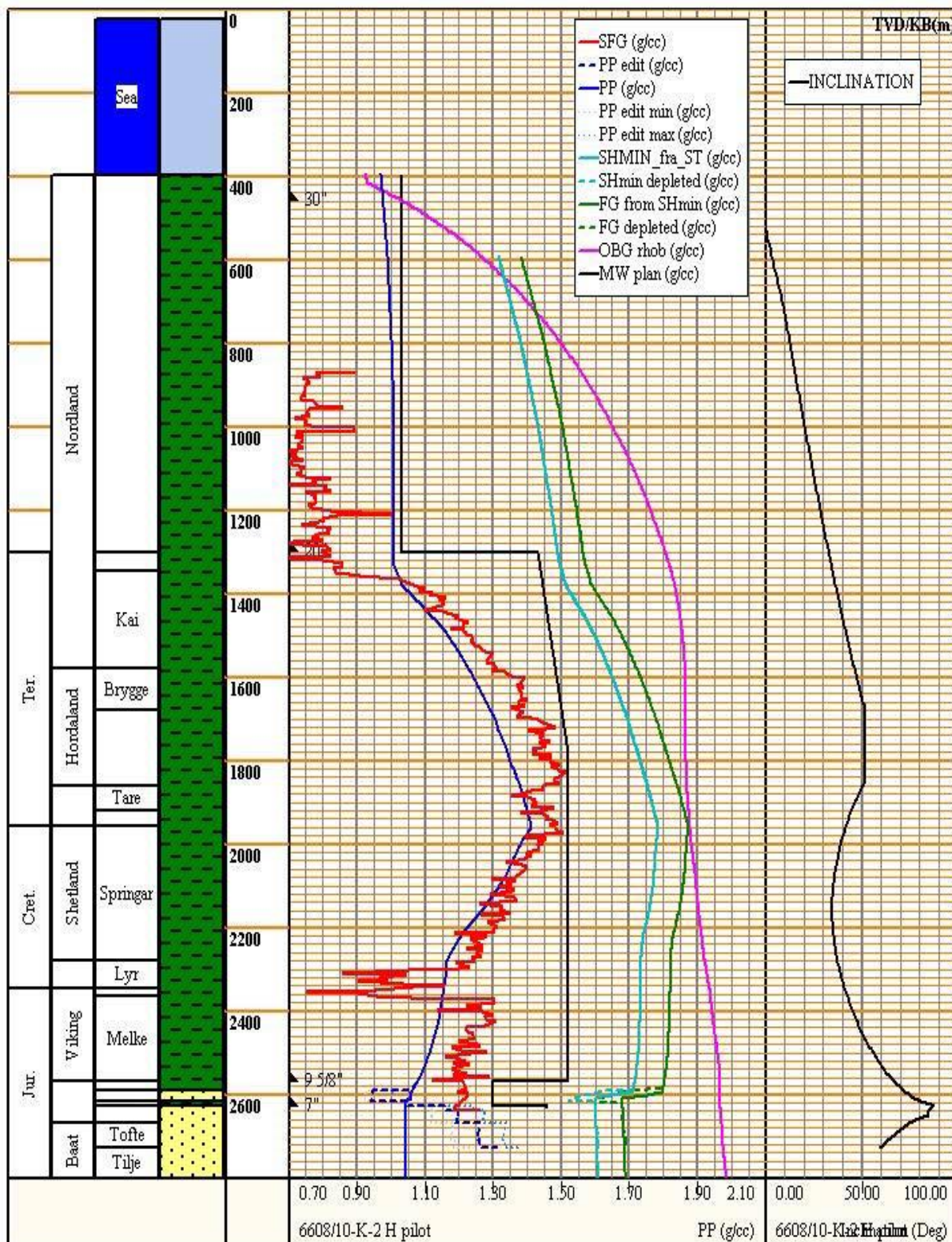
FIGURE 4.29: DRILLING PROGRAM FOR NORNE (STATOIL ASA, 2010)

4.3.2　　Steady State Parameter Sensitivity Studies

The following sensitivity studies were performed by using Excel spreadsheets. The data from the Norne well program (figure 4.29) was digitized and the Stassi d'Alia model was applied. As seen from earlier simulations, not all parameters display significant changes caused by thermal, chemical or transient effects. Because of this, the results of the simulation of only two parameters are presented in the following sections. However, the activity of the drilling fluid has demonstrated significant effects, but as it has been simulated several times, it will not be presented again in this section.

4.3.2.1　Effect of Poisson's Ratio

Table 4.6 displays the input parameters for this simulation. This simulation will illustrate the effects of changing the Poisson's ratio from 0,32 to 0,30 and 0,34. Figure 4.30 shows the change in the collapse pressure due to different values of the Poisson's ratio. As seen from figure 4.31, when the Poisson's ratio is increased 6,3% ($\nu = 0,34$) the collapse pressure increases with an average of 8%. When the Poisson's ratio is decreased 6,3% ($\nu = 0,32$), the collapse pressure decreases with an average of 4,9%. Figure 4.32 illustrates the wellbore pressures with the effect of Poisson's ratio.

TABLE 4.6: INPUT PARAMETERS

Parameters	Ref.	Input values	
Poisson's ratio, ν	0,32	0,3	0,34
Activity of drilling fluid, a_{df}	0,9	-	-
Activity of formation water, a_{fw}	0,9	-	-
η_s=	0,52941	-	-
Biot's coefficient, α_{Biot}	0,96	-	-
Temperature Tw, deg C	0	-	-

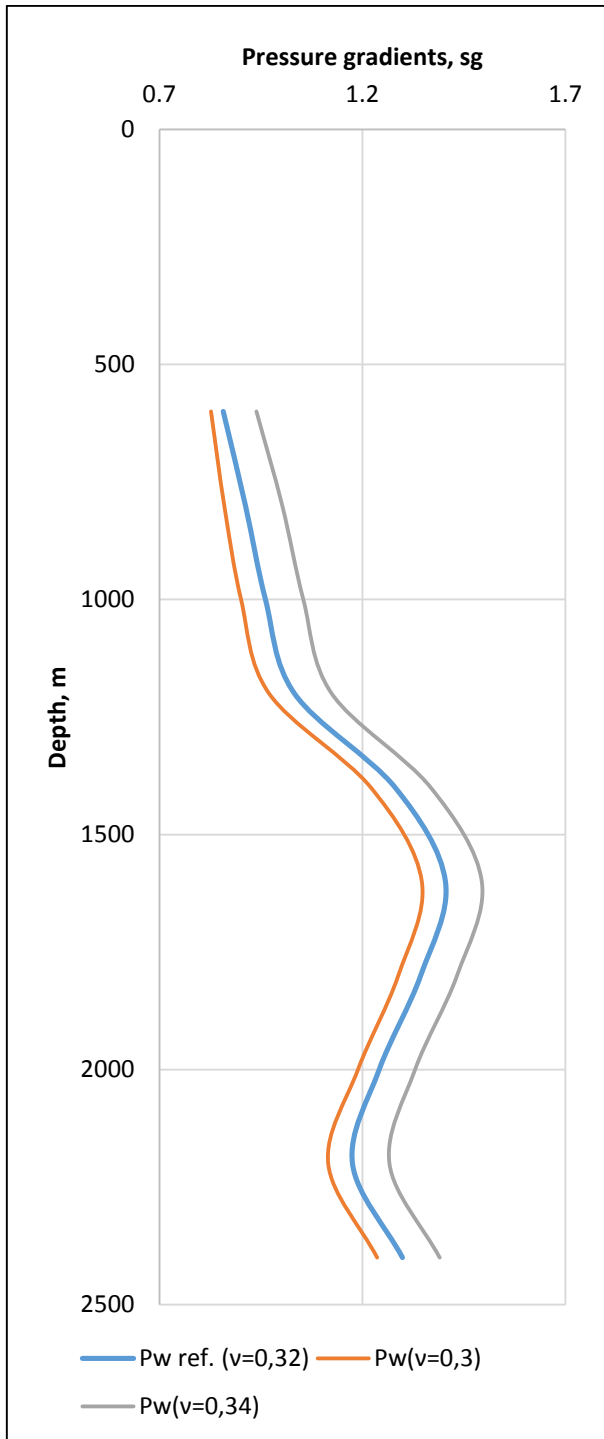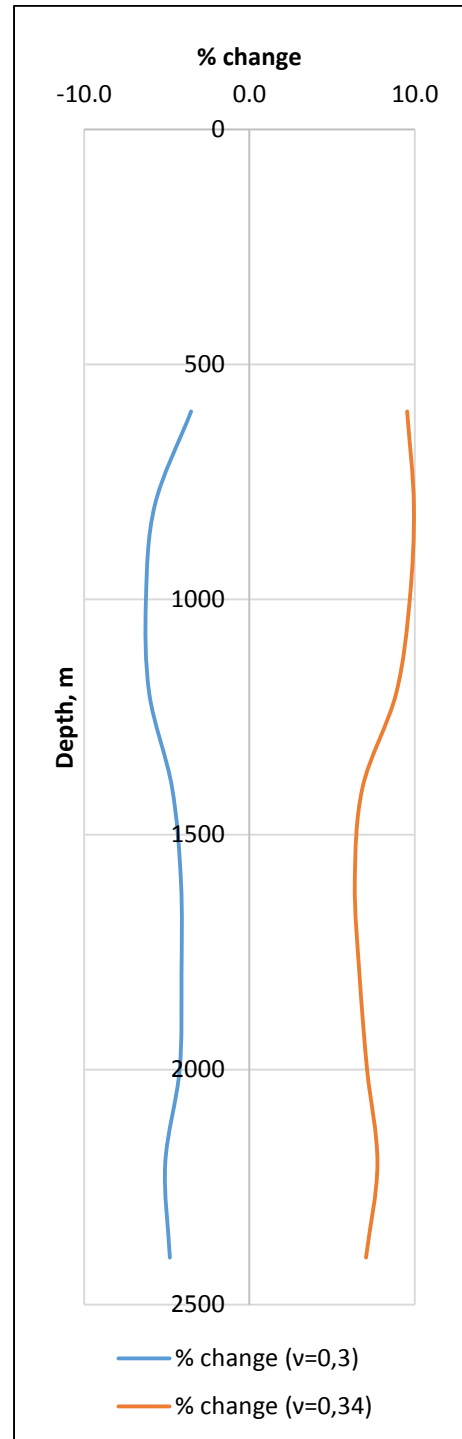FIGURE 4.30: CHANGE IN COLLAPSE PRESSURE
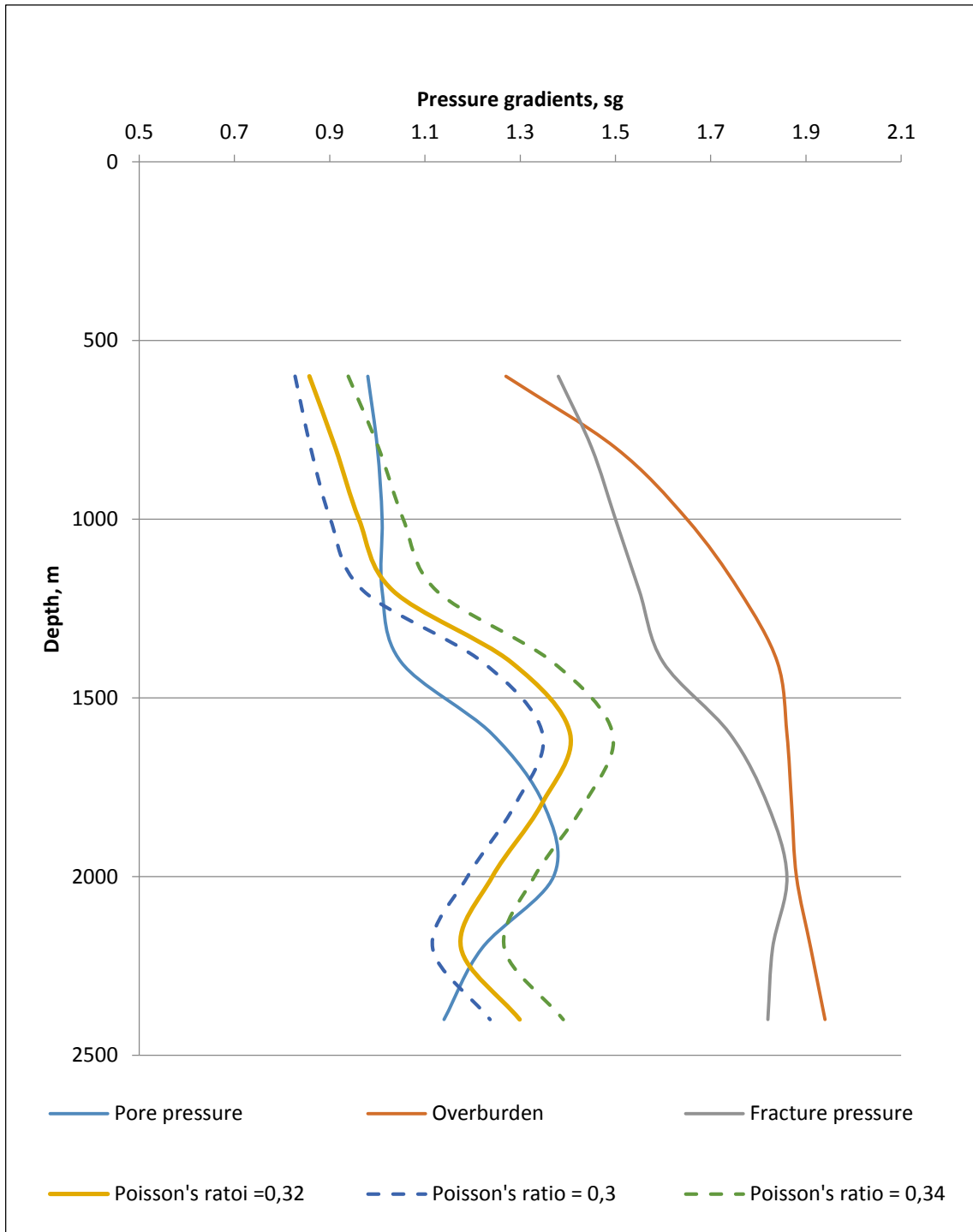

FIGURE 4.31: PERCENTAGE CHANGE IN COLLAPSE PRESSURE

FIGURE 4.32: WELLBORE PRESSURES

4.3.2.2 Effect of Biot's Coefficient

Table 4.7 displays the input parameters for this simulation. This simulation will illustrate the effects of changing the of Biot's coefficient from 0,96 to 0,86 and 1,0. Figure 4.33 displays the changes in the collapse pressure due to the effect of Biot's coefficient. As seen from figure 4.34, when the Biot's coefficient is increased by 4,2% ($\alpha = 1,0$), the collapse pressure decreases with an average of 1,5%. When the Biot's coefficient is decreased by 10,4% ($\alpha = 0,86$), the collapse pressure increases by 6,4%. Figure 4.35 displays the wellbore pressures with the effect of Biot's coefficient.

TABLE 4.7: INPUT PARAMETERS

Parameters	Ref.	Input values	
Biot's coefficient, α_{Biot}	0,96	0,86	1,0
Poisson's ratio, ν	0,32		
Activity of drilling fluid, a_{df}	0,9	-	-
Activity of formation water, a_{fw}	0,9	-	-
$\eta_S=$	0,52941	-	-
Temperature Tw, deg C	0	-	-
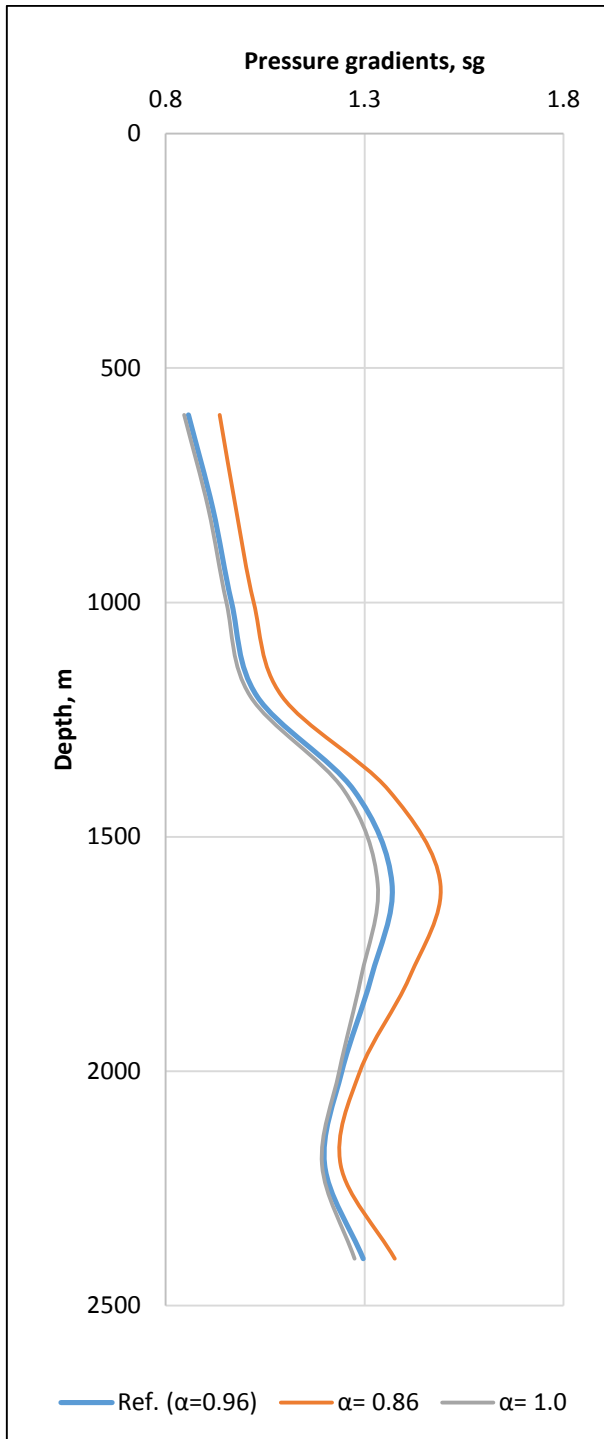
FIGURE 4.33: CHANGE IN COLLAPSE PRESSURE DUE TO BIOT'S COEFFICIENT
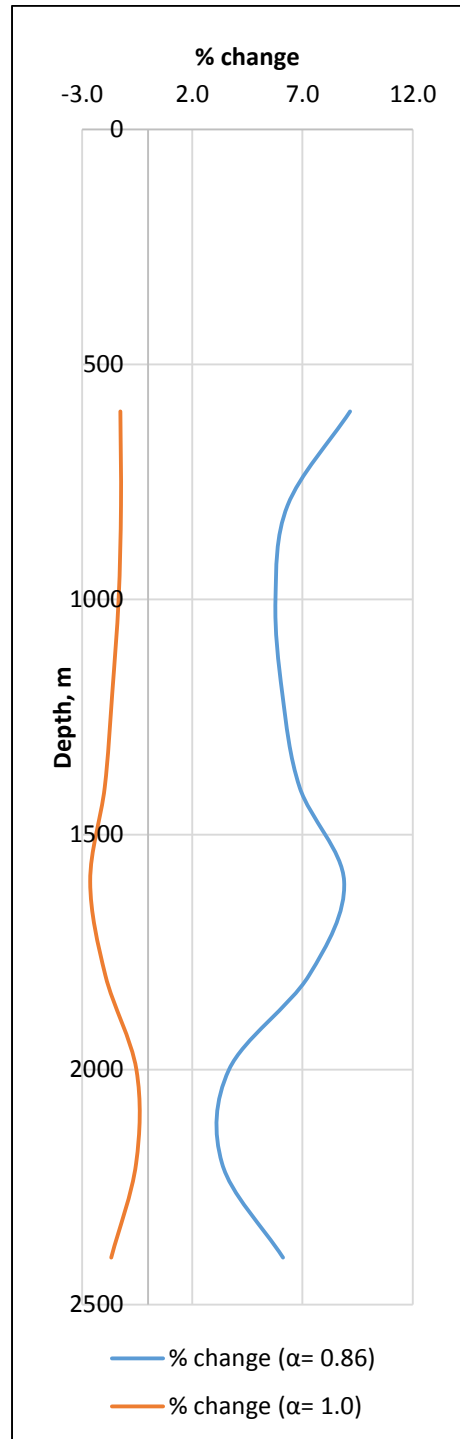
FIGURE 4.34:PERCENTAGE CHANGE IN COLLAPSE PRESSURE

79
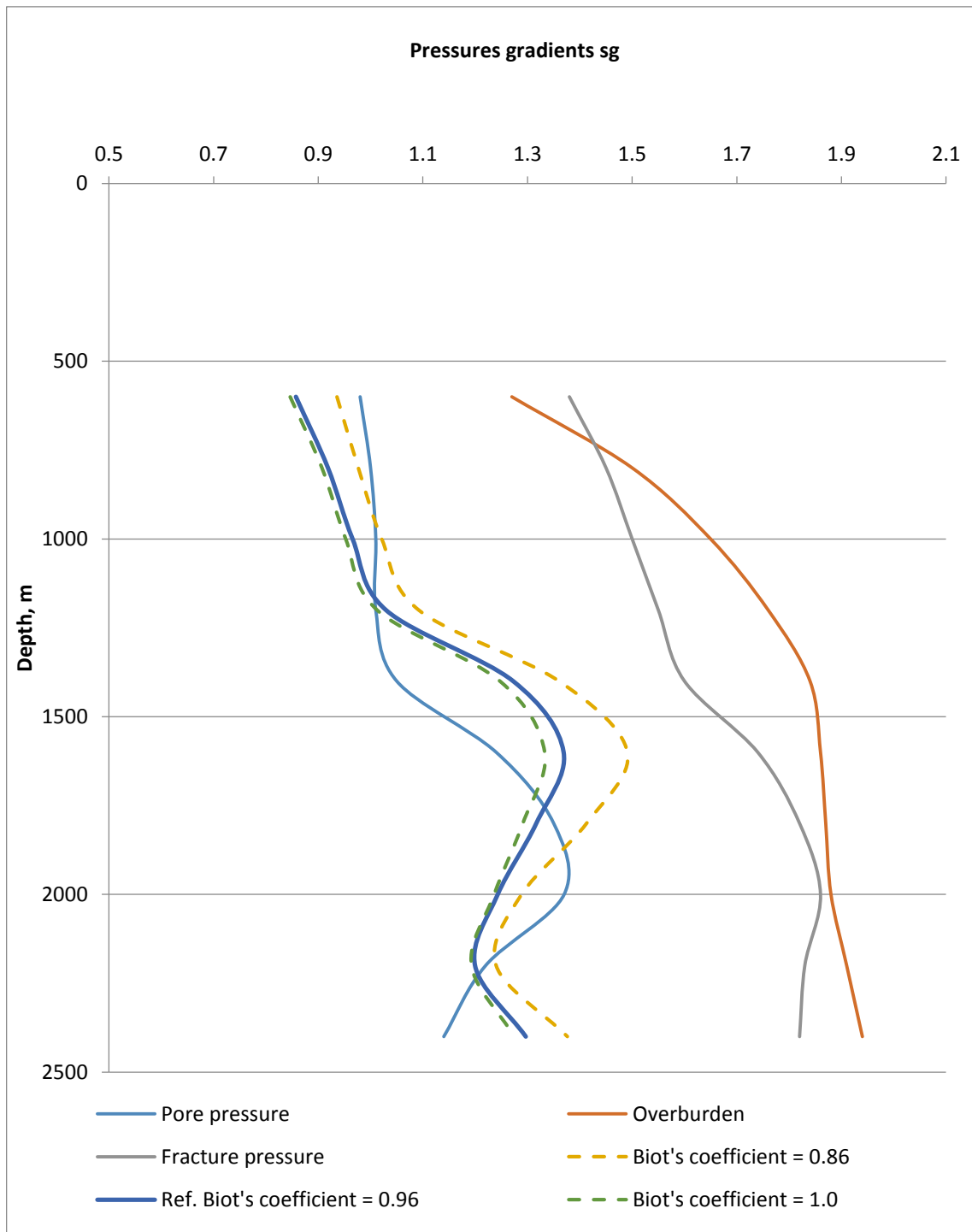
FIGURE 4.35: WELLBORE PRESSURES

4.3.3 Transient State Parameter Sensitivity Studies

The transient effect was derived as in section 3.3. In this section the results for time dependent UCS will be presented. Thermal and chemical effects were not considered, hence the

combination of the effects are not simulated in this section. The only parameters considered for the transient effect are time (1 and 10 days) and the uniaxial compressive strength, C_0.
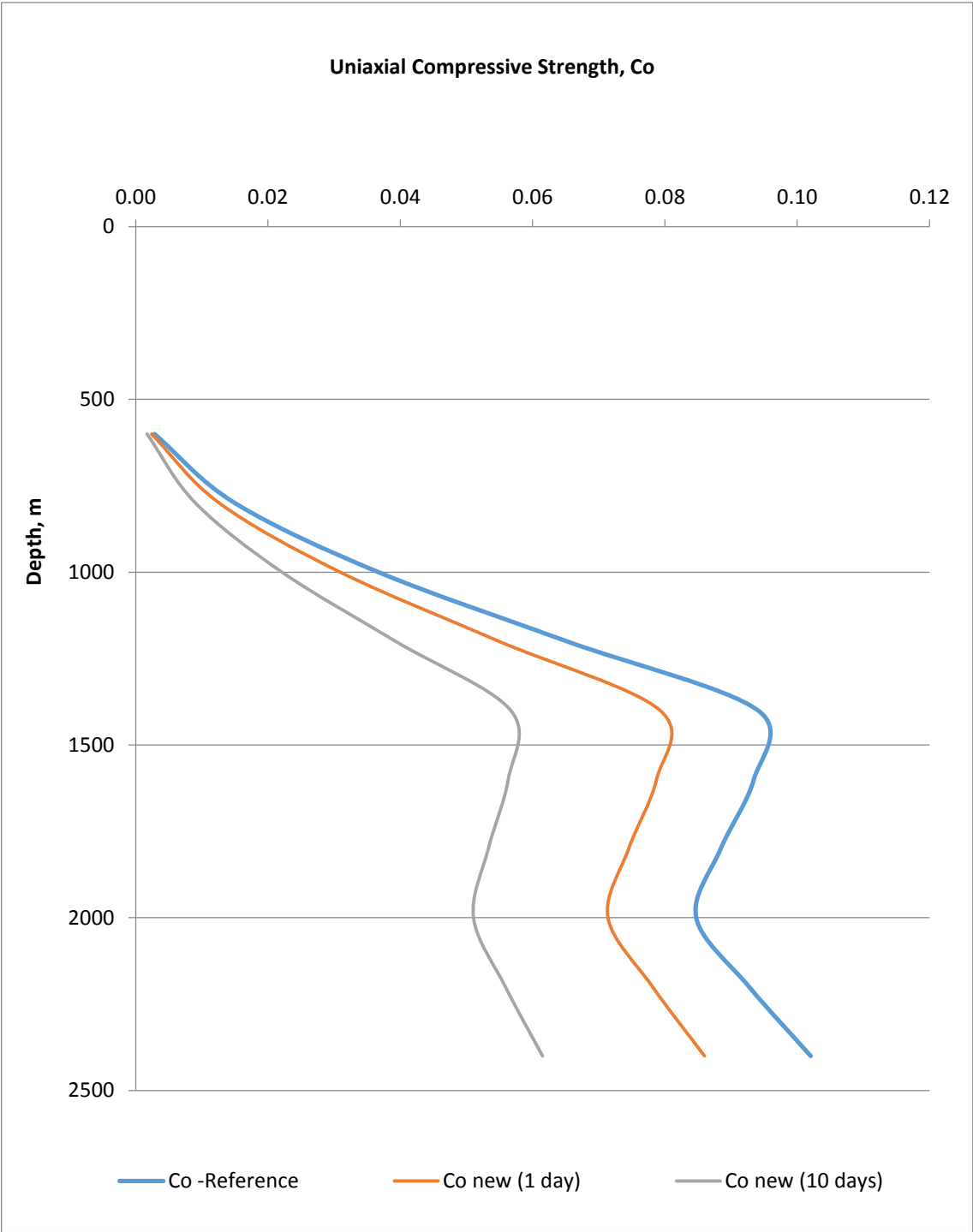
FIGURE 4.36: TRANSIENT EFFECT

As seen from figure 4.36, the uniaxial compressive strength decreases by 15,7% after one day, and after ten days it decreases by 39,7% from its original value. Figure 4.37 displays the transient effect on the collapse pressure. By observing the figure, it is obvious that the collapse pressure increases with time. Figure 4.38 illustrates the percentage change in collapse pressure. As seen, after one day, the collapse pressure changes the most in the interval 1200-2400 meters (1,5 -1,9 %). After ten days, the collapse pressure changes the most in the interval 1000-2400 meters (2,4 - 4,9%).

FIGURE 4.37: CHANGE IN COLLAPSE PRESSURE DUE TO TRANSIENT EFFECT

FIGURE 4.38: PERCENTAGE CHANGE IN COLLAPSE PRESSURE

5 Discussion

In the following sections, the steady and transient state effects of the simulated parameters are discussed and compared. A few comparisons between the two well collapse models are also given.

It should be noted that the simulations would be more accurate if sonic-log data were available for the two well programs of Heidrun and Norne. Also, if the parameters varied downwards the well instead of maintaining a constant value, the 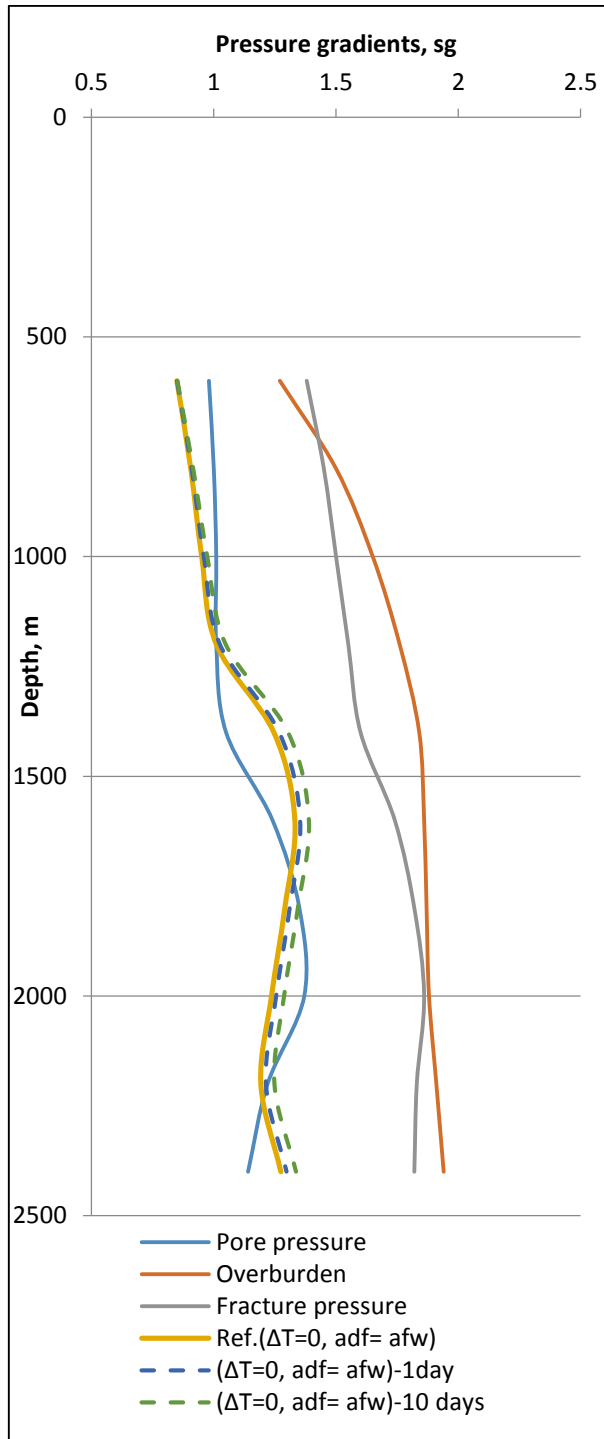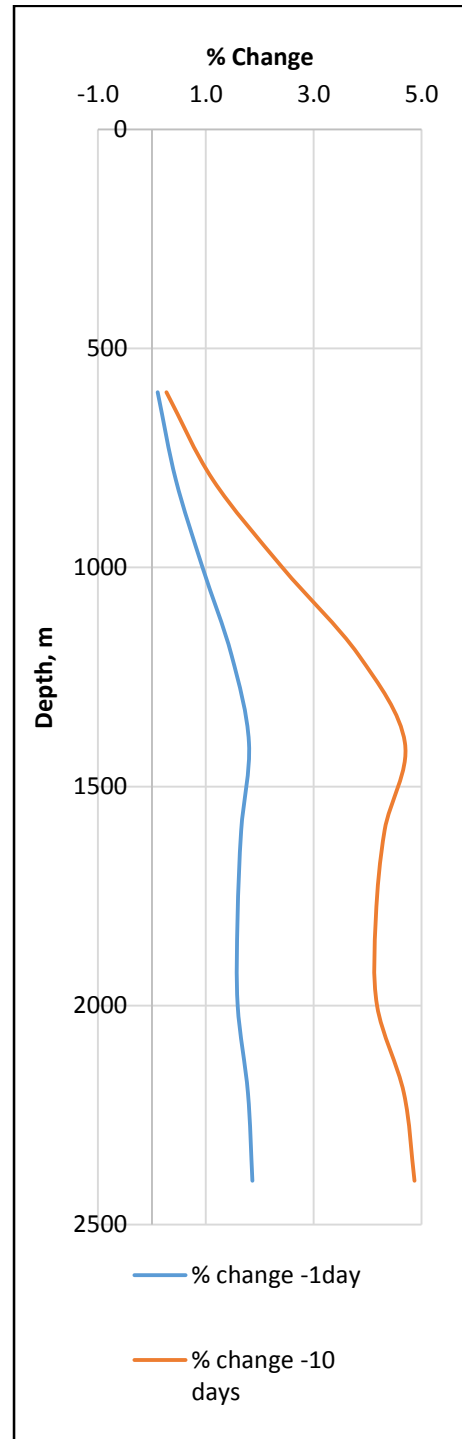simulations and the models would be more precise . However, the best effort was made in choosing parameters in the most realistic ranges.

5.1 Heidrun with the Mohr-Coulomb Model

5.1.1   Steady State

From the simulation results it is seen that the 3 % increase in Poisson's ratio changed the collapse pressure by an average value of 0,8%. Although this change is not very high, it is definitely noticeable compared to other simulated effects of changing parameters.

The results of changing the Biot's coefficient demonstrated rather visible changes compared to Poisson's ratio. When the Biot's coefficient was altered by 1%, the collapse pressure increased with an average of 0,9%, which is approximately 3 times more than the effect of Poisson's ratio.

The simulation results demonstrated that the water activity of the drilling fluid is the most sensitive parameter during steady state simulation with the Mohr-Coulomb model. When the water activity of the drilling fluid is 13,8% lower than the activity of the shale formation, the collapse pressure changes from a minimum of -22,9% to a maximum of 17,6%. When the water activity of the drilling fluid is 4,2% higher than the activity of the shale formation, the collapse pressure changes with a minimum of 3,1% to a maximum of 28,6 %.

5.1.2   Transient State

As seen when plotting the UCS with depth, considering no other effects than in-situ stresses, the UCS decreases in time. After one day, it decreases 15,7 % and after ten days it decreases 39,8%. Hence, the change is most severe after the first day. Furthermore, the effect of UCS on

the collapse pressure varies a lot down the well. The effect is the most prominent in the middle section of the well (around 1500 meters) when only in-situ stresses are acting. Considering the combined effect (transient, chemical and thermal), the collapse pressure increases when $a_{df} > a_{fw}$ and decreases when $a_{df} < a_{fw}$. The combined effect is the most visible in the upper part and in the middle part of the well. It should be noted that the change is not very visible from the first to the tenth day, but very visible from the reference point to the first day and from the reference point to the tenth day. The combined effect is due to the hydration of the shale, which evolves as time passes, and weakens the uniaxial compressive strength.

5.2 Heidrun with the Stassi D'Alia Model

5.2.1   Steady State

As the activity of the drilling fluid demonstrated the most significant effect from the simulation with the Mohr-Coulomb model, only this parameter was presented for the Stassi d'Alia simulation. When $a_{df} < a_{fw}$ the collapse pressure decreases, and when $a_{df} > a_{df}$ the collapse pressure increases as for the Mohr-Coulomb model.

Changing the a_{df} to a value of ca. 14% lower than the a_{fw}, and also to a value of ca. 4% lower than the a_{fw}, was presented similarly for the two models. Hence, it is easy to compare the two models and see the difference. When a_{df} was 14% lower than the a_{fw} the Mohr-Coulomb showed changes in the range of -22,9% to 17,6%, while the Stassi d'Alia demonstrated in the range of -22,6% to -2,2%. Comparisons between the two models indicated that the water activity was more sensitive when applying the Mohr-Coulomb model than when applying the Stassi d'Alia model.

5.2.2   Transient State with Combined Effect

The combined effect after the first day, when the a_{df} was ca. 1,4% lower than the a_{fw} and when a_{df} was ca. 4% higher than the a_{fw} displayed the most visible changes in the middle section of the well (1000-1700 meters). In this section the changes ranged from 1,41-1,5% when $a_{df} < a_{fw}$ and 1,43-1,59% when $a_{df} > a_{fw}$. Hence, the combined effect seems to have a lower percentage impact than the single effect, when considering the drilling fluid activity.

5.3 Norne with the Stassi D'Alia Model

5.3.1   Steady State

When Poisson's ratio increases by 6,3%, the collapse pressure increases by an average of 8%. When Poisson's ratio is decreased by 6,3%, the collapse pressure decreases with an average of 4,9%. This implies that the Poisson's ratio is not as sensitive for the Stassi d'Alia model as it is for the Mohr-Coulomb model (when increased by 0,8% it gave an average increase of the collapse pressure by 3%).

When Biot's coefficient was increased by 4,2% the collapse pressure decreased by an average of 1,5%. When decreased by 10,4% the collapse pressure increased by 6,4%. This implies that when the Biot's coefficient's effect is simulated the Stassi d'Alia model works in an opposite way, than how the Mohr-Coulomb model works.

5.3.2   Transient State

When only in-situ stresses are considered, the UCS decreases by 15,7% after one day and 39,7% after ten days, the same as for the Mohr-Coulomb model. After one day the collapse pressure changes the most in the middle section of the well (1000-1400 meters) in the range of 1,5-1,9%. After ten days the collapse pressure changes the most in the same section, but in the range of 2,4-4,9%. This is approximately the same change as when applying the Mohr-Coulomb model. Both models gave approximately 1,5% change after one day, and both models displayed the most significant change in the middle section of the well.

6 Conclusion

The following conclusion is based on the overall simulation results obtained from the two derived models, Stassi d'Alia and Mohr-Coulomb. By analyzing the results, it can be seen that the chemical effects has a significant impact on the collapse curve. By changing the activity of the drilling fluid, the direction of the fluid flow may be controlled. The drilling fluid activity must therefore be carefully adjusted by adding different solutes during the design phase of the well program.

- The temperature effects were not very visible, and the results were therefore not discussed, but rather put in the appendix. Hence, the case studies showed that chemical effects were far more dominating than the thermal effects for the given Norne and Heidrun well programs.

- The transient effects were most visible after day one and the UCS had a great impact on the collapse pressure. Hence, it is important to include the continuous changes in collapse pressure in time, when designing the well program.

- Observing the simulations for the steady state conditions, the most sensitive parameter is the activity of the drilling fluid, followed by the Biot's coefficient, and then the Poisson's ratio.

- Observing the simulations for transient state, it was found that cohesive strength and time are the most sensitive parameters.

- Comparing the two models, the Mohr-Coulomb model displayed more noticeable effects when the parameters were changed. However, this does not imply that Stassi d'Alia is a more precise model.

- Overall, the chemical, thermal and transient effects, all have an immense impact on the collapse strength, and must be considered during the designing of the mud weight program.

A recommendation of further work is to simulate by using sonic log data, derive collapse models based on Mogi-Coulomb and Ewy failure criteria.

7 References

Aadnøy, B. S., 2003. Introduction to special issue wellbore stability. *Journal of Petroleum Science and Engineering*, pp. 79-82.

Aadnøy, B. S., 2010. *Modern Well Design.* 2 ed. Boca Raton: CRC Press/ Balkema .

Aadnøy, B. S. & Chenevert, M. E., 1987. Stability of highly inclined boreholes. *Society of Petroleum Engineers*, pp. 364-374.

Aadnøy, B. S. & Looyeh, R., 2011. *Petroleum Rock Mechanincs.* s.l.:Gulf Professional Publishing.

Adlam, J., 1995. *The Norne Field Development Overview.* s.l., s.n.

Al-Ajmi, A. M. & Zimmermann, R. W., 2006. Stability analysis of vertical boreholes using the Mogi-Coulomb failure criterion. *International Journal of Rock Mechanics and Mining Sciences*, pp. 1200-1211.

Anon., 2009. *Energy Pedia News.* [Online]
Available at: http://www.energy-pedia.com/news/norway/statoilhydro-to-use-deepsea-bergen-on-heidrun--norne-and-%C3%A5sgard-production-drilling
[Accessed 15 June 2009].

Bjørlykke, K., 2010. *Petroleum Geoscience: From Sedimentary Environments to Rock Physics.* s.l.:Springer-Verlag Berlin Hidelberg.

Chen, G., Chenevert, M. E., Sharma, M. M. & Yu, M., 2001. Poroelastic chemical, and thermal effects on wellbore stability in shales. *American Rock Mechanics Association.*

Cheryan, M., 1998. *Ultrafiltration and Microfiltration.* 2 ed. Lancaster: Technomic Publ..

Cossé, R., 1993. *Basics of Reservoir Engineering.* Paris and Rueil-Malmaison: Editions Technip and Insitut français du Pétrole.

Dorkhabi, R., 2014. Fracture, Fracture Everywhere. *GEO ExPro*, Issue 4.

Ewy, R. T., 1998. *Wellbore Stability Predictions Using a Modified Lade Criterion.* s.l., Society of Petroleum Engineers.

Ewy, R. T. & Chen, G., 2005. Thermoporoelastic Effect on Wellbore Stability. *Society of Petroleum Engineers*, pp. 121-129.

Farrokhrouz, M. & Asef, M. R., 2010. Simulating Model To Reduce Detrimental Acidizing In Tabnak Gas Field. *Society of Petroleum Engineers.*

Farrokhrouz, M. & Asef, M. R., 2013. *Shale engineering: Mechanics and Mechanisms.* Leiden: CRC Press.

Fjær, E. et al., 2008. *Petroleum Related Rock Mechanics.* 2 ed. Amsterdam: Elsevier.

Gardner, G. H., Gardner, L. W. & Gregory, A. R., 1974. Formation velocity and density - The diagnostic basics for stratigraphic traps. *Gephysics*, pp. 770-780.

Grotzinger, J. & Jordan, T. H., 2010. *Understanding Earth.* 6 ed. New York: W.H Freeman.

Henderson, C., Richards, B. & Barclay, J., 2012. *Geological Atlas of the Western Canada Sedimentary Basin.* Calgary: Alberta Geological Survey.

Horsrud, P., 2001. Estimating Mechanical Properties of Shale from Empirical Correlations. *Sociecty of Petroleum Engineers*, pp. 68-73.

King, H. M., 2015. *Shale.* [Online]
Available at: http://geology.com/rocks/shale.shtml
[Accessed 6 May 2015].

Lal, M., 1999. Shale stability: Drilling fluid interaction and shale strength. *Society of Petroleum Engineers*.

Ludovic, R. P., Macbeth, C., Hajnasser, Y. & Schutjens, P., 2012. An evaluation of pore pressure diffusion into a shale overburden and sideburden induced by production-related changes in reservoir fluid pressure. *Journal Of Geophysics And Engineering*, pp. 345-358.

Myers, J. D., 2015. *Second recovery.* [Online].

NPD Facts Heidrun, 2015. *NPD Factpages.* [Online]
Available at:
http://factpages.npd.no/FactPages/default.aspx?nav1=field&nav2=PageVie
w|All&nav3=43771&culture=en
[Accessed 6 May 2015].

NPD Facts Norne, 2015. *NPD Factpages.* [Online]
Available at:
http://factpages.npd.no/FactPages/default.aspx?nav1=field&nav2=PageVie
w|All&nav3=43771&culture=en
[Accessed 6 May 2015].

NPD Facts, 2013. *NPD Factpages.* [Online]
Available at: http://www.npd.no/publikasjoner/rapporter/co2-
samleatlas/2/
[Accessed 6 May 2015].

NPD, n.d. *NPD FactPages.* [Online]
Available at:

http://www.npd.no/engelsk/cwi/pbl/field_jpgs/43778_Norne.jpg
[Accessed 12 June 2015].

PTIL/PSA, n.d. *PTIL.* [Online]
Available at:
http://www.ptil.no/getfile.php/Tilsyn%20p%C3%A5%20nettet/okasjonskart
/broenn%206609_10-2.jpg
[Accessed 12 June 2015].

Rider, M. H. & Kennedy, M., 2012. *The Geological Interpretation of Well Logs.*
3 ed. Aberdeen: Rider- Frech.

Shaw, D. B. & Weaver, C. E., 1965. The mineralogical composition of shales.
Journal of Sedimentary Petrology, pp. 213-222.

Soroush, H., 2013. Shale Gas Geomechanics. *EAGE.*

Soroush, H., Qutoh, H. & Weatherford Oil, Tool, ME Ltd, 2010. Evaluation of
rock properties using ultrasonic pulse technique and correlating static to
dynamic elastic constants. *GEO India.*

Statoil ASA, 2010. *Individual Development Well Activity Program Drilling Well
NO 6608/10-K-2 H & AH Norne,* s.l.: Statoil ASA.

Steiger, R. P. & Leung, P. K., 1992. Quantitative Determination of the
Mechanical Properties of shale. *Society of Petroleum Engineers,* pp. 181-185.

Stjern, G., Agle, A. & Horsrud, P., 2003. Local rock mechanical knowledge
improves drilling performance in fractured formations at the Heidrun field.
Journal of Petroleum Science and Engineering, pp. 83-96.

Stjern, G., Horsrud, P. & Agle, A., 2003. Local rock mechanical knowledge
proves drilling performance in fractured formations at the Heidrun field.
Journal of Petroleum Science and Engineering, pp. 83-96.

Tariq, A., 2014. *Wellbore stability in Shale formations,* Stavanger: University
of Stavanger.

Venkanna, B. K., 2010. *Fundamentals of heat and mass transfer.* New Delhi:
PHI Learning.

Yenugu, M., 2010. *Ultrasonic Measurements of Anisotropy of Shales,* s.l.:
School of Geology and Geophysics.

Yu, M., Chenevert, M. E. & Sharma, M. M., 2003. Chemical-mechanical
wellbore instability model for shales. pp. 131-143..

Yu, M., Chenevert, M. E., Sharma, M. M. & Chen, G., 2002. *Chemical and
thermal effects on wellbore stabilito of shale formations,* Auston: The
Univeristy of Texas.

Zhang, J. et al., 2006. Maintaining the stability of deviated and horizontal
wells.

8 Appendix

Appendix A: Heidrun Mohr-Coulomb Simulation

A. Effect of the Internal Friction Angle

The internal friction angle is an important parameter that describes the angle in which sliding takes place on the rock surface without any external load applied. Table A:1 shows the simulation input parameters. In the first column are the reference parameters, with $\varphi = 32°$.

TABLE A: 1 INPUT PARAMETERS

Parameters	Ref.	Input values	
Internal friction angle, φ , deg	32	35	38
Biot's coefficient, α_{Biot}	0,86	-	-
Poisson's ratio, ν	0,22	-	-
$\eta_{MC}=$	0,62	-	-
Failure angle, β_{MC}, deg	61	62,5	64

Figure A1 shows the simulation result. As seen from figure A2, when the internal friction angle increases by 9,4%, the collapse pressure increases by an average of -1,3%.
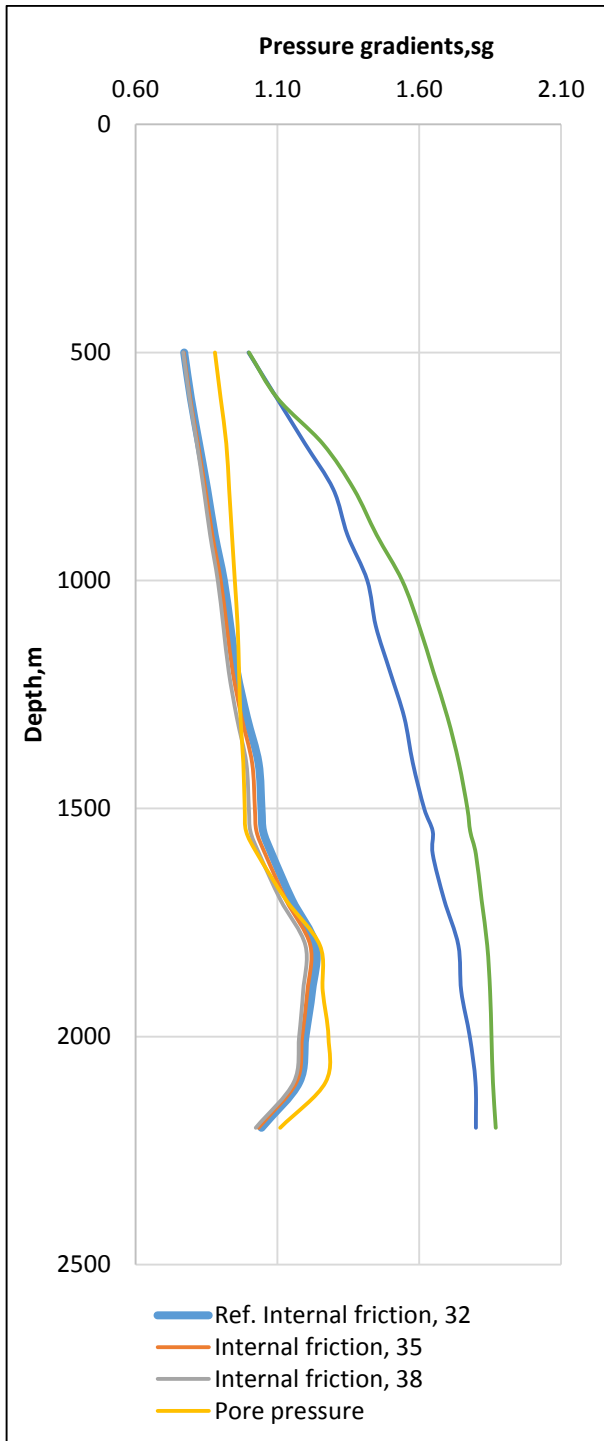
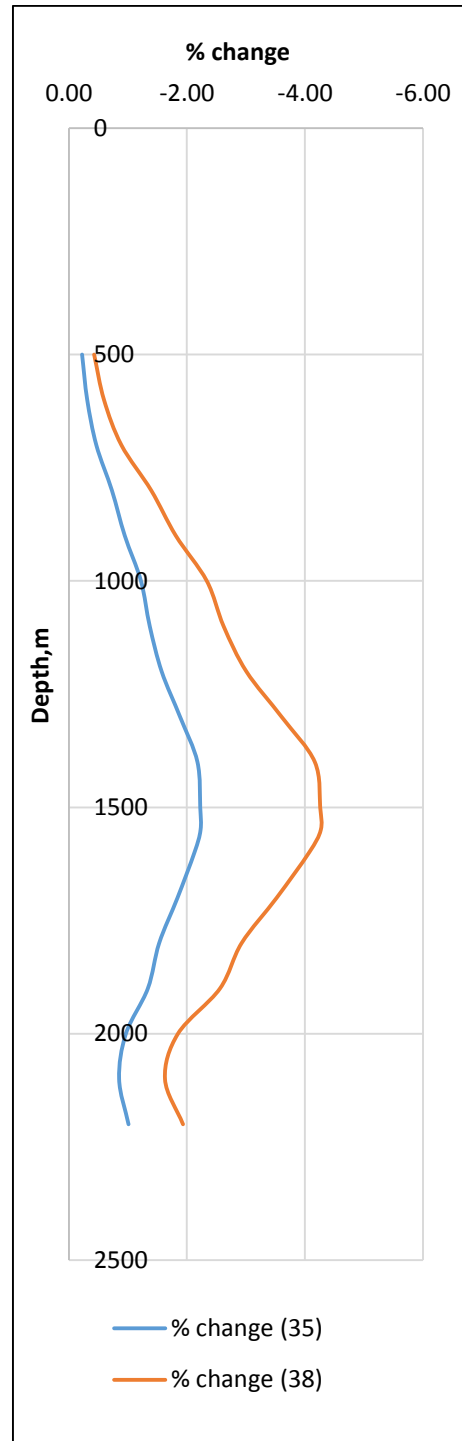FIGURE A 1: PRESSURE RESULTS FOR CHANGES IN
INTERNAL FRICTION ANGLE

FIGURE A 2: PERCENTAGE CHANGE IN
COLLAPSE PRESSURE

B. Effect of temperature

Table B:1 shows the simulation input parameters. In the first column are the reference parameters.

TABLE B: 1

Parameters	Ref.	Input values	
		10% increase	10% decrease
Temperature, deg C	Tw		
Internal friction angle, φ , deg	32	-	-
Poisson's ratio, ν	0,22	-	-
Biot's coefficient, α_{Biot}	0,86	-	-
$\eta_{MC}=$	0,62	-	-
Failure angle, β_{MC}, deg	61	-	-
E-modulus	6895	-	-
Thermal conductivity, k	$8,633 \times 10^{-6}$	-	-

Figure B1 shows the simulation result. As seen from figure B2, when the temperature increases by 10%, the collapse pressure increases by an average of 2,5%. When the temperature decreases by 10% the collapse pressure increases by an average of 1,6%. It should be noted that the changes are more visible further up the well.
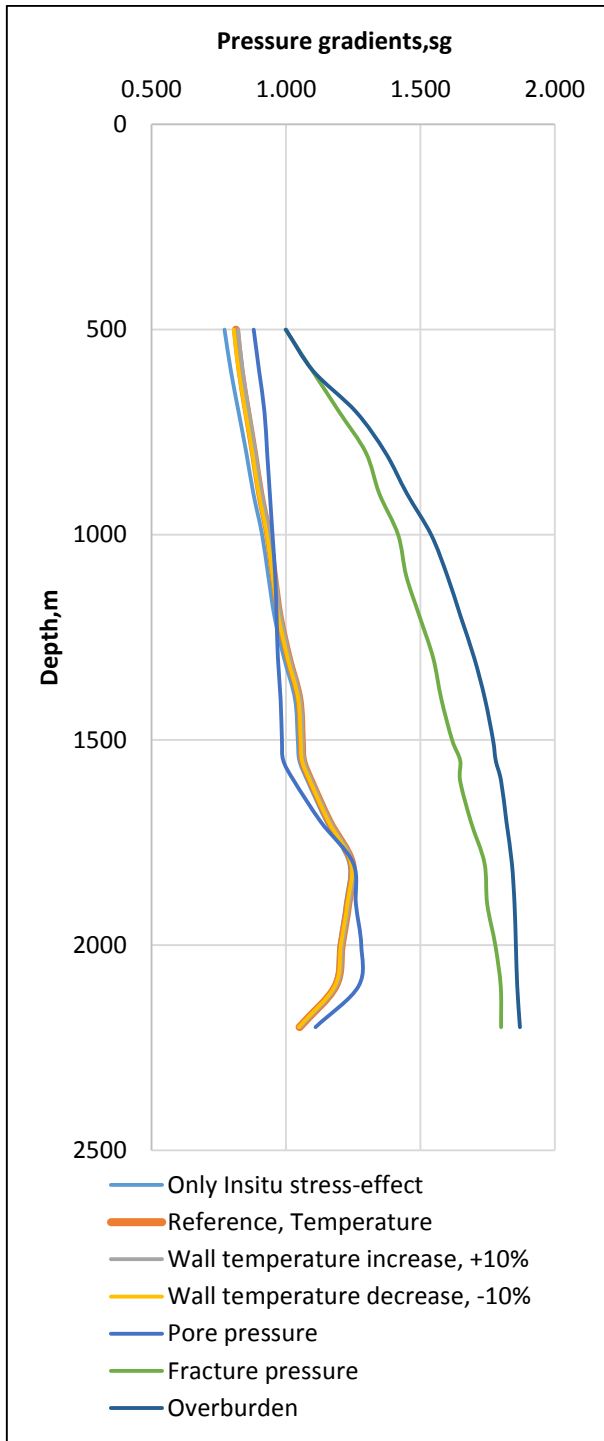
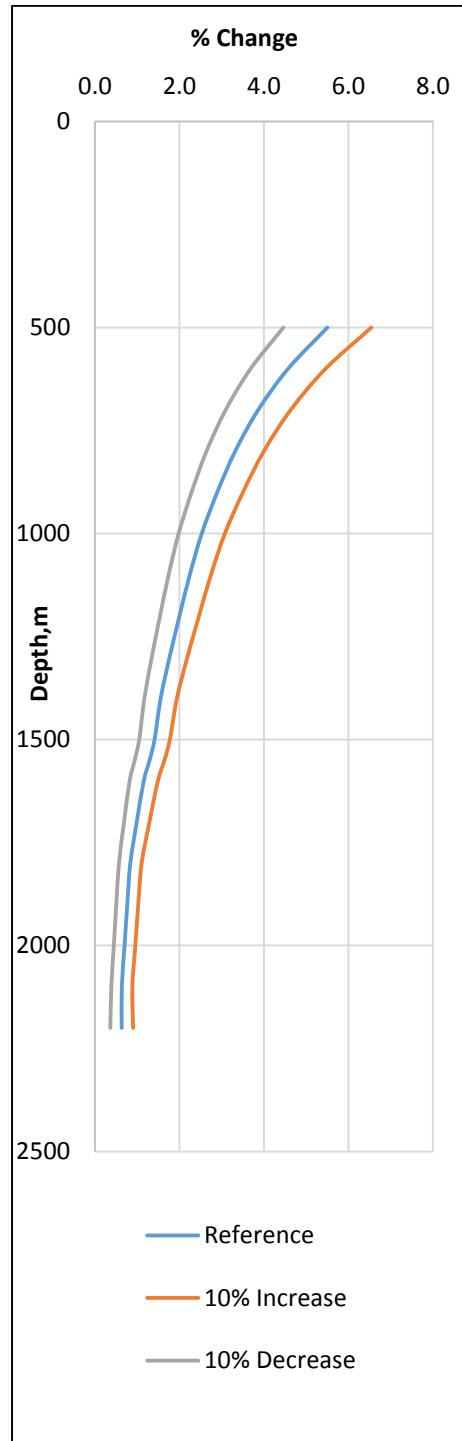FIGURE B. 1: PRESSURE RESULTS FOR CHANGES IN
TEMPERATURE

FIGURE B .2: PERCENTAGE CHANGE IN
COLLAPSE PRESSURE

C. Effect of E-Modulus

Table C:1 shows the simulation input parameters. In the first column are the reference parameters. The second column displays the values for a 10% increase in E-modulus, and the third column shows the values for a 10% decrease.

TABLE C: 1 : INPUT PARAMETERS

Parameters	Ref.	Input values	
E-modulus	6895	7584,5	6205
Temperature, deg C	Tw	-	-
Internal friction angle, φ , deg	32	-	-
Poisson's ratio, ν	0,22	-	-
Biot's coefficient, α_{Biot}	0,86	-	-
$\eta_{MC}=$	0,62	-	-
Failure angle, β_{MC}, deg	61	-	-
Thermal conductivity, k	$8,633 \times 10^{-6}$	-	-

Figure C1 shows the simulation result. As seen from figure C2, when the E-modulus increases by 10%, the collapse pressure increase by an average of 2,2%. When the E-modulus decreases by 10%, the collapse pressure decreases by an average of 1,8% . It should be noted that the changes are more visible further up the well.
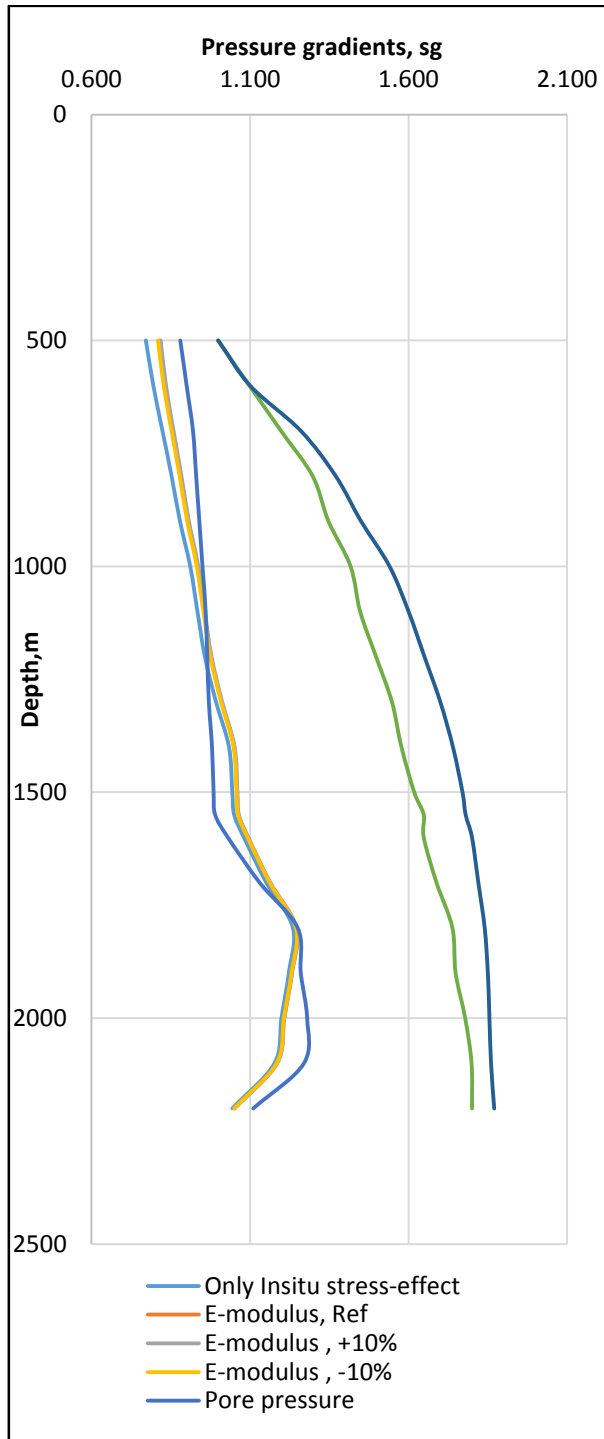
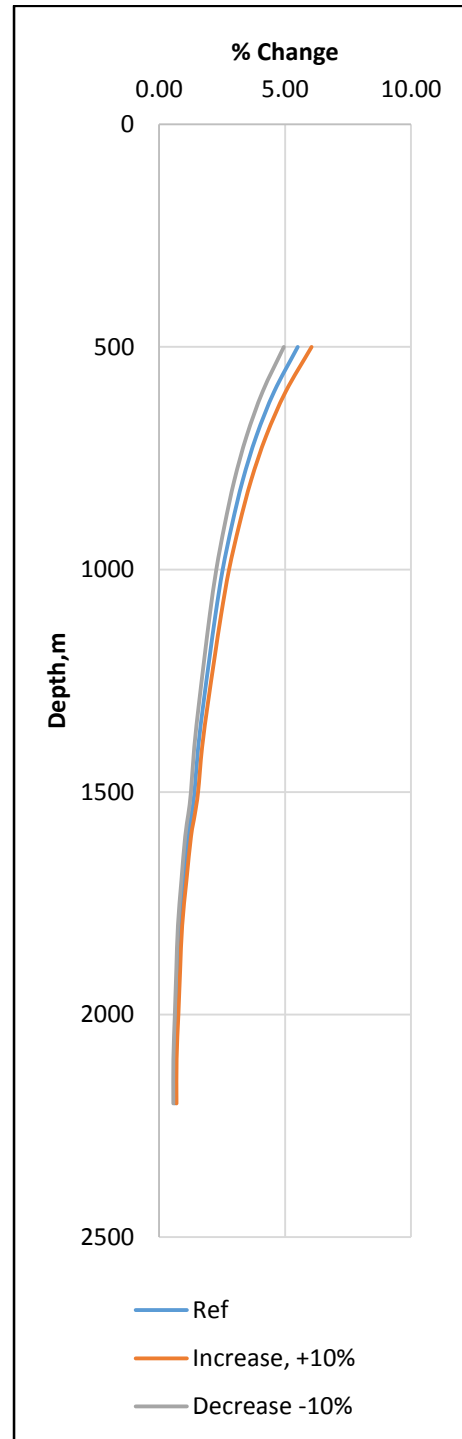FIGURE C 1: PRESSURE RESULTS FOR CHANGES IN E-MODULUS

FIGURE C 2: PERCENTAGE CHANGE IN COLLAPSE PRESSURE

97

D. **Effect of Thermal Conductivity**

Table D.1 shows the simulation input parameters. In the first column are the reference parameters. The second column shows the values for a 10% increase in thermal conductivity, and the third column shows the values of a 10% decrease.

TABLE D.1: INPUT PARAMETERS

Parameters	Ref.	Input values	
Thermal conductivity, k	$8{,}633 \times 10^{-6}$	$7{,}769 \times 10^{-6}$	$9{,}496 \times 10^{-6}$
E-modulus	6895	-	-
Temperature, deg C	Tw	-	-
Internal friction angle, φ , deg	32	-	-
Biot's coefficient, α_{Biot}	0,86	-	-
Poisson's ratio, ν	0,22	-	-
$\eta_{MC}=$	0,62	-	-
Failure angle, β_{MC}, deg	61	-	-

Figure D1 shows the simulation result. As seen from figure D2, when the thermal conductivity increases by 10%, the collapse pressure increases by an average of 2%. When the thermal conductivity decreases by 10%, the collapse pressure decreases by an average of 2,4%.
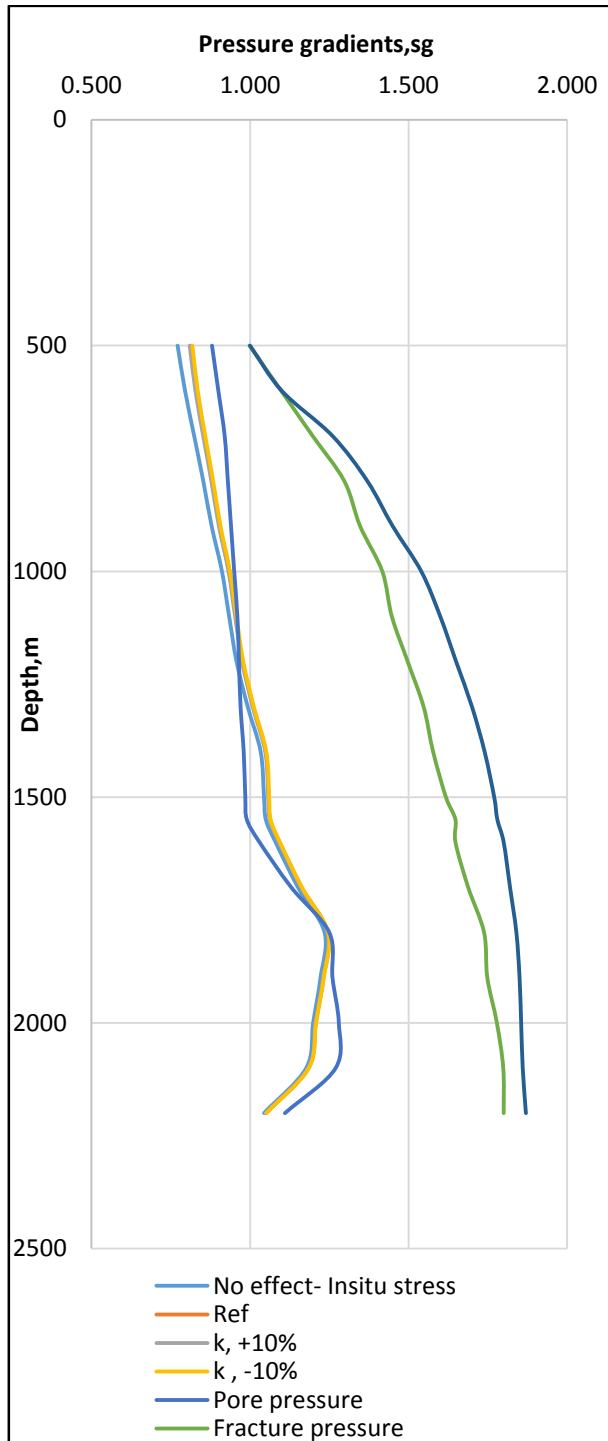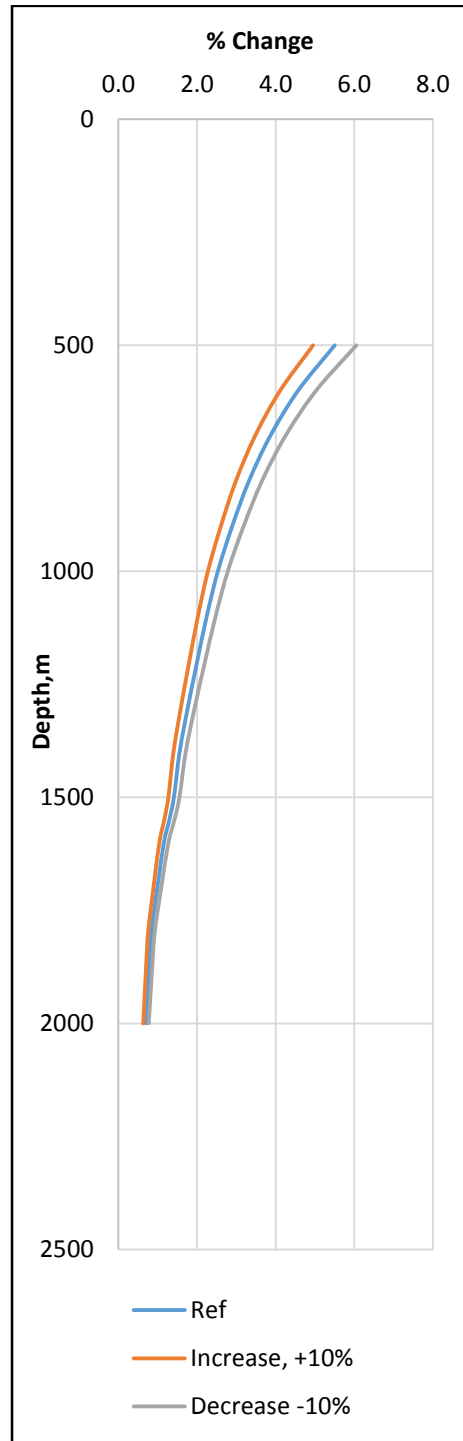
FIGURE D 1: PRESSURE RESULTS FOR CHANGES IN THERMAL CONDUCTIVITY

FIGURE D 2: PERCENTAGE CHANGE IN COLLAPSE PRESSURE